Interplay of Charge Density Modulations and Superconductivity

A Thesis Submitted to the

College of Graduate Studies and Research

in Partial Fulfillment of the Requirements

for the degree of Master of Science

in the Department of Physics and Engineering Physics

University of Saskatchewan

Saskatoon

By

Jason Sadowski

Permission to Use

In presenting this thesis in partial fulfilment of the requirements for a Postgraduate degree from the University of Saskatchewan, I agree that the Libraries of this University may make it freely available for inspection. I further agree that permission for copying of this thesis in any manner, in whole or in part, for scholarly purposes may be granted by the professor or professors who supervised my thesis work or, in their absence, by the Head of the Department or the Dean of the College in which my thesis work was done. It is understood that any copying or publication or use of this thesis or parts thereof for financial gain shall not be allowed without my written permission. It is also understood that due recognition shall be given to me and to the University of Saskatchewan in any scholarly use which may be made of any material in my thesis.

Requests for permission to copy or to make other use of material in this thesis in whole or part should be addressed to:

Head of the Department of Physics and Engineering Physics
116 Science Place
University of Saskatchewan
Saskatoon, Saskatchewan
Canada
S7N 5E2

Abstract

Recent studies of the transition metal dichalcogenide 2H-$NbSe_2$ have led to debate in the scientific community regarding the mechanism of the charge density wave (CDW) instability in this material. Moreover, whether or not CDW boosts or competes with superconductivity (SC) is still unknown, as there are experimental measurements which supports both scenarios. Motivated by these measurements we study the interplay of charge density modulations and superconductivity in the context of the Bogoliubov de-Gennes (BdG) equations formulated on a tight-binding lattice. As the BdG equations require large numerical demand, software which utilizes parallel algorithms have been developed to solve these equations directly and numerically. Calculations were performed on a large-scale Beowulf-class PC cluster at the University of Saskatchewan.

We first study the effects of inhomogeneity on nanoscale superconductors due to the presence of surfaces or a single impurity deposited in the sample. It is illustrated that CDW can coexist with SC in a finite-size s-wave superconductor. Our calculations show that a weak impurity potential can lead to significant suppression of the superconducting order parameter, more so than a strong impurity. In particular, in a nanoscale d-wave superconductor with strong electron-phonon coupling, the scattering by a weakly attractive impurity can nearly kill superconductivity over the entire sample.

Calculations for periodic systems also show that CDW can coexist with s-wave superconductivity. In order to identify the cause of the CDW instability, the BdG equations have been generalized to include the next-nearest neighbour hopping integral t'. It is shown that the CDW state is strongly affected by the magnitude of t', while superconductivity is not. The difference between the CDW and SC states is a result of the anomalous, or off-diagonal, coupling between particle and hole components of quasiparticle excitations. The Fermi surface is changed as t' is varied; in particular, the perfect nesting and coincidence of the nesting vectors and the vectors connecting van Hove singularities (vHs) for $t' = 0$ is destroyed, and vHs move away from the Fermi energy. It is found that within our one-band tight-binding model with isotropic s-wave superconductivity, CDW and SC can coexist only for vanishing $t' = 0$ and for $t' \neq 0$, the homogeneous SC state always has the lowest ground-state energy.

Furthermore, we find in our model that as t' increases, the main cause of the divergence in the dielectric response accompanying the CDW transition changes from nesting to the vHs mechanism proposed by Rice and Scott [1]. It is still an open question as to the origin of CDW and its interplay with SC in multiple-band, anisotropic superconductors such as 2H-$NbSe_2$, for which fundamental theory is lacking. The work presented in this thesis demonstrates the possible coexistence of charge density waves and superconductivity, and provides insight into the mechanism of electronic instability causing charge density waves.

Acknowledgements

I would like to express my most sincere gratitude to my supervisor, Dr. Kaori Tanaka. She has been both a friend and mentor throughout my studies, and I am thankful for our many discussions together. Her encouragement, support, and advice throughout my project were invaluable to me. I would also like to thank my committee members Dr. John Tse, Dr. Masoud Ghezelbash, and the external examiner Dr. Artur Sowa for their contributions.

I am grateful to Jason Hlady and Sean Cavanaugh at the High Performance Computing Research Facility for their help and suggestions during the development of my parallel routines. Their service and support were instrumental in completing this work. I further want to thank the Natural Science and Engineering Research Council as well as the Canada Foundation for Innovation for their financial support.

I wish to thank the many friends I have made in the Department of Physics and Engineering Physics for making this a fun and exciting place to to learn and grow. My thanks go out to Elise, Robyn, and Paul. You are cherished colleagues and friends. I am indebted to the faculty and staff for all of their kindness and hospitality, as well as for the opportunities they have provided me.

Finally, I am indebted to my family and loved ones for their unconditional encouragement and support. I could not have done it without them.

For my parents, Wayne and Deborah Sadowski.

Contents

Permission to Use i

Abstract ii

Acknowledgements iv

Contents vi

List of Tables viii

List of Figures ix

List of Abbreviations xiii

1 Introduction 1
- 1.1 High-T_c Superconductivity . . . 1
- 1.2 Transition Metal Dichalcogenides . . . 3
- 1.3 Motivation for Research . . . 4
- 1.4 Layout of Thesis . . . 9

2 Theoretical Background 10
- 2.1 BCS Theory of Superconductivity . . . 10
- 2.2 Charge Density Waves . . . 15
- 2.3 BdG Theory . . . 19

3 Formulation 21
- 3.1 Extended-Hubbard Hamiltonian . . . 21
- 3.2 Mean-Field Decomposition . . . 22
- 3.3 BdG Equations . . . 24

4 Surfaces and Impurities in Nanoscale Systems 28
- 4.1 Degenerate SC and CDW State . . . 28
- 4.2 D-Wave SC Sensitive to Surfaces . . . 30
- 4.3 S-Wave SC with Single Impurity . . . 31
- 4.4 D-Wave SC with Single Impurity . . . 33

5 Charge Density Modulations and Superconductivity 36
- 5.1 Coexistence of CDW and Superconductivity . . . 36
  - 5.1.1 Density Wave State . . . 37
  - 5.1.2 Superconducting State . . . 39
  - 5.1.3 Coexistence of CDW and SC states . . . 39
- 5.2 Mechanism for CDW in the Tight-Binding Model . . . 41

5.3 CDW state with varying Fermi Surface 44
5.4 Results and Discussion 51

6 Conclusion **66**

References **69**

A BdG Equations in the Tight-Binding Model **73**
A.1 Derivation of the BdG Equations 73
A.2 Derivation for the Ground-State Energy 77

B Numerical Methods **78**
B.1 Introduction to ScaLAPACK 78
B.2 BLACS Process Grid 79
B.3 Distributed Memory Storage Scheme 80
B.4 Diagonalization of BdG Matrix Elements 81
B.5 Calculations with Distributed Matrices 83

C Derivation of the Dispersion Relations **85**

D Chemical Potential and DOS for Negative t' **88**

List of Tables

5.1 Results of the zero-temperature CDW amplitude and SC order parameter for the three degenerate states. All states have $E_0 = -990.40t$ and $T_C = 0.33t$. In the mixed state (CDW+SC) the amplitude of the CDW modulations and the SC order parameter are reduced to $\sim 62\%$ and $\sim 78\%$ their value in their respective pure states. 41

List of Figures

1.1 2H-$NbSe_2$ Fermi-Surface 5

1.2 Mapping of k-points corresponding to CDW and k-dependent SC gap. The CDW wave vectors are consistent with the van Hove singularity scenario for the CDW and these regions in k-space correspond to regions where the superconducting gap is *maximum*. 7

1.3 Map of the CDW energy gap in k-space. Regions where the CDW gap is maximum correspond to regions where the SC energy gap is minimum. . . . 8

2.1 Peierls' construction of a charge density wave. By distorting the lattice one can move the energy gap from the zone boundary to $\pi/2a$. For a half-filled band this corresponds to the Fermi level. This lattice distortion causes a periodic modulation of the electron density, the wavelength of which is dependent on k_F. 16

2.2 Fermi surface nesting for a three-dimensional material with 1-,2- and 3-dimensional energy dispersion. The number of points which lead to divergent terms in the response is strongly reduced in three dimensions. 18

4.1 (a) Electron density for a 20x20-site s-wave superconductor at half filling. On-site coupling is $U_{ii} = -1.5t$. The CDW+SC state is degenerate with the SC state that has uniform density density distribution. (b) S-wave order parameter for the system described in (a). The order parameter shows slight suppression along the boundaries due to the loss of kinetic energy, but the presence of a surface is not a pair-breaking process in s-wave superconductors. 29

4.2 Plot of the relative CDW amplitude and SC order parameter as a function of temperature in an s-wave superconductor described in Figure 4.1(a). Amplitudes are taken with respect to the pure SC and CDW states. The CDW and SC states clearly have the same transition temperatures; however, the amplitude of the order parameter in the CDW+SC state is suppressed by $\sim 8\%$ with respect to the SC state. Additionally, the amplitude of the density modulations in the CDW+SC state is suppressed by $\sim 60\%$ with respect to the pure CDW state. 30

4.3 (a) Electron density for a pure 19x19-site d-wave superconductor at half filling. Off-site coupling is $U_{ij} = -1.5t$. The density is suppressed all along the boundaries, uniformly except for the four corners, and CDW-like density modulations are no longer favoured in the ground-state. (b) D-wave order parameter for the system described in (a). Similarly to the average density distribution, the d-wave order parameter is suppressed on the surfaces. . . . 31

4.4 (a) Electron density for a 21x21 s-wave superconductor at half filling. The on-site coupling strength is $U_{ii} = -2t$. In the presence of an impurity the degeneracy of the pure case is removed and the CDW becomes the favoured ground-state. (b) S-Wave order parameter for the system described in (a). The upper (purple) plot is the order parameter for $\epsilon_{11,11} = -10.0t$, while the lower (green) plot is for $\epsilon_{11,11} = -0.5t$. 32

4.5 Electron density for a 21x21 d-wave superconductor at half filling with impurity $\epsilon_{11,11} = -0.5t$. (a) $U_{ij} = -1.5t$. For weak electron-phonon coupling, the charge density becomes localized around the impurity site and slightly suppressed at the boundary. (b) $U_{ij} = -2.7t$. For strong coupling the effect in (a) becomes amplified, as electrons can gain more energy by moving away from the surface. In this example the electron density is completely suppressed at the boundary. 35

4.6 D-wave order parameter for the system described in Figure 4.5. (a) $U_{ij} = -1.5t$. The order parameter is suppressed at the location of the impurity as well as along the boundary. (b) $U_{ij} = -2.7t$. In the strong coupling case the order parameter is completely suppressed at the impurity site, leaving a narrow region of "surface superconductivity". 35

5.1 (a) Charge density distribution for the 18x18 cell lattice with $|U_{ii}| = 2.50t$. The colour scheme is such that regions of low density correspond to red, while high density correspond to green. (b) The total density of states for the pure CDW state, clearly exhibiting an energy gap. 37

5.2 LDOS for the 18x18 cell lattice with $|U_{ii}| = 2.50t$. Sites (1,1) and (2,2) have density less than one, while sites (1,2) and (2,1) have density greater than one. The alternating charge density seen in Figure 5.1(a) results in a spatially alternating local density of states. 38

5.3 Site-averaged density of states for a 18x18 cell and $|U_{ii}| = 2.50t$ in the SC state. Contrary to the CDW state the LDOS is identical at all sites in the sample and therefore equivalent to the total DOS. The total DOS in the SC state is identical to the DOS shown in Figure 5.1(b) for the CDW state. . . . 40

5.4 Relative CDW amplitude and SC order parameter as a function of temperature in the CDW+SC mixed state. Both SC and CDW disappear at the same temperature. 41

5.5 The Fermi surface for the 2D square lattice of the tight-binding Hamiltonian at half filling. Nesting vectors connecting the sides of the square Fermi surface are shown as black dashed lines and the positions of the saddle points are marked with black circles. The vectors that connect the saddle points are identical to the nesting vectors. 43

5.6 Energy-momentum disperion relation for positive and negative values of t'. The contours at the base identify the Fermi surfaces. In addition to a phase shift of $\vec{k} = (\pm\pi/a, \pm\pi/a)$, surfaces for $t' = 0.25$ are electron-like, while for $t' = -0.25$ are hole-like. When $t' \to -t'$ then $E(\vec{k}) \to -E(\vec{k})$. 45

5.7 Energy-momentum dispersion relation for various values of hopping parameter t'. The contours at the base identify the Fermi surfaces. As t' is increased the top and bottom of the band rises, while the saddle points move lower in energy. As a result the saddle points are moved off the Fermi surface. . . . 47

5.8 Band structure for a 24x24 cell in the normal state. As t' increases the top and bottom of the band move toward positive energy, while the total bandwidth remains $8t$. The band also begins to flatten near the vHs, indicating a large density of states at this energy. 49

5.9 Calculated Fermi surface for a 24x24 cell at various values of hopping parameter t'. The plot only spans one quarter of the first BZ, and the full Fermi surface can be found by symmetrizing to the other three quadrants. When $t' \neq 0$ perfect nesting disappears. 49

5.10 (a) Density of states for $0 \leq t' \leq 0.45$ for $|U| = 0$ on a 24x24 lattice. The results are shifted vertically for clarity. As t' increases the bandwidth remains $8t$. However, negative-energy band width decreases, while the width of positive energy states increases. In addition the saddle-point singularity shifts from $E = 0$ at $t' = 0$ towards $E = -2t$ as t' increases. (b) The same results obtained by the BdG equations, indicating the "artificial" states.. 50

5.11 Density of states for various values of t'. The results are shifted vertically for clarity. These results were obtained for a 24x24 cell at half filling using on-site coupling $|U| = 5t$. The gap seen in the DOS is a result of the presence of a CDW. The vHs, only for the hole states for $t' \neq 0$, are strongly enhanced as t' increases and the hole bandwidth is squeezed. 51

5.12 LDOS for the 24x24 cell lattice with $|U_{ii}| = 5t$ and $t' = 0.1$. 54

5.13 LDOS for the 24x24 cell lattice with $|U_{ii}| = 5t$ and $t' = 0.2$. 54

5.14 LDOS for the 24x24 cell lattice with $|U_{ii}| = 5t$ and $t' = 0.3$. 55

5.15 LDOS for the 24x24 cell lattice with $|U_{ii}| = 5t$ and $t' = 0.4$. 55

5.16 Dependence of gap size and T_c on t' for the CDW and SC states on a 24x24 lattice with $|U| = 5t$. (a) The critical temperature is gradually reduced as t' increases while the gap size decreases linearly. (b) For the CDW state one can see a definite slope change in the gap to T_c ratio around $t' \sim 0.25$, while in the SC state the ratio remains constant at the BCS value. 57

5.17 $Re\ \epsilon(\vec{q}, \omega \rightarrow 0)$ for $0 \leq t' \leq 0.45$. The divergence at the nesting vector $\vec{q} = (\pm\pi/a, \pm\pi/a)$ can clearly be seen for all t'. As the Fermi surface changes its shape in the dispersion and perfect nesting is destroyed, the divergence rapidly decreases and begins to level off at $t' \sim 0.25$, indicating that the vHs becomes dominant. 59

5.18 Density of States for various values of t'. The results are shifted vertically for clarity. These results were obtained using a 24x24 cell at half filling using an onsite coupling parameter of $|U| = 5t$ in the superconducting state. 60

5.19 Chemical potential for $0 \leq t' \leq 0.5$ for $|U| = 5t$ on a 24x24 lattice. Results are shown for the normal, superconducting, and CDW states. One can see that the chemical potential as a function of t' behaves identically for the CDW and normal states; however, there is a very different behaviour in the SC state. This is a result of the anomalous coupling between particle and hole amplitudes in the SC state. 62
5.20 Ground state energy for $0 \leq t' \leq 0.5$ for $|U| = 5t$ on a 24x24 lattice. Results are shown for the normal, superconducting, and CDW states. At $t' = 0$ the SC and CDW states have identical ground-state energy and is considerably lower than the normal-state energy. However for $t' \neq 0$ the energies split and the SC state always has the lowest energy. The behaviour of the normal and CDW states energy curves is a result of the dependence of the chemical potential on t'. 63
5.21 Condensation energy per particle for SC and CDW states. The condensation energy is the difference in energy between the SC/CDW and normal states. The larger condensation energy for the SC state indicates that it is the most stable configuration. The increase in the CDW condensation energy near $t' = 0.25$ may indicate that a vHs driven CDW is more stable than due to nesting. 64

B.1 ScaLAPACK software hierarchy 78
B.2 Example of a $P_r = 2$, $P_c = 4$ process grid 79
B.3 A 9X9 matrix distributed across 4 processors 80

D.1 Chemical potential for $-0.5 \leq t' \leq 0.5$ on a 24x24 lattice. The chemical potential increases for negative t' such that μ for positive and that for negative t' are mirror images of each other. 88
D.2 Density of states for positive and negative t' on a 24x24 cell with $|U| = 5t$. Clearly, the density of states for positive and negative t' are identical with $E(k) \rightarrow -E(k)$. 89

List of Abbreviations

SC	Superconductivity
ScaLAPACK	Scalable Linear Algebra Package
STM	Scanning Tunnelling Microscope
STS	Scanning Tunnelling Spectroscopy
LDOS	Local Density of States
DOS	Density of States
BdG	Bogoliubov de Gennes Theory
BCS	The Bardeen-Cooper-Schrieffer Theory
TMD	Transition Metal Dichalcogenide
CDW	Charge Density Wave
FS	Fermi Surface
vHs	van Hove Singularity
LOF	List of Figures
LOT	List of Tables

Chapter 1

Introduction

1.1 High-T_c Superconductivity

Superconductivity (SC), a phenomenon first uncovered by Heike Kamerlingh Onnes [2] in 1911, was an accidental discovery during the race to be the first to produce liquid helium [3]. During a series of experiments he found that the electrical resistance of pure mercury sharply dropped to zero at 4K, and later coined the phrase *superconductivity* to describe it. It did not take long for experimentalists to discover other superconducting materials and even more exotic superconductors. Today, superconductivity above 77K is quite common and can be demonstrated in high school class rooms and laboratories. As of 2009, the superconductor with the highest recorded transition temperature is $HgBa_2Ca_2Cu_3O_x$ with $T_C = 135K$ [4].

In 1933 Meissner and Ochenfeld found that in addition to zero resistivity, superconducting metals expel magnetic fields from their interior. The expulsion of magnetic flux is a fundamentally different behaviour from that of a "perfect conductor", and demonstration of the Meissner effect became the defining characteristic of a superconductor. Theorists worked tirelessly for over 40 years trying to explain superconductivity until finally in 1957, Bardeen, Cooper, and Schrieffer (BCS) were able to successfully apply the (relatively new) quantum theory to describe superconductivity. In this theory electrons in the metal form pairs (known as Cooper pairs) via interactions with the crystal lattice. The ground state is a *coherent state* of these Cooper pairs, and the long-range correlation among them is what generates the unusual properties of superconductors. For a while it seemed that superconductivity was well understood in terms of the BCS theory and research began to slow down. One of the key predictions of the BCS theory was that superconductivity should not occur at any

temperature higher than roughly 40K. In 1986, however, to the surprise of the scientific community Bednorz and Müller discovered superconductivity in the Ba-La-Cu-O system near 30K [5] and soon after materials with T_C's higher than 77K were found.

For the first time superconducting materials could be studied using liquid nitrogen as opposed to liquid helium which is more costly and difficult to work with. These so called high-temperature (or "high-T_c") superconductors not only exhibit a transition temperature T_c that exceeds far beyond the highest T_c predicted by the BCS theory, but also defy the conventional expectation that superconductivity cannot occur in magnetic materials. These compounds, known as cuprates, are systems which contain CuO_2 planes. In these planes oxygen (O^{--}) has a valence configuration of $(1s)^2(2s)^2(2p)^6$ while copper (Cu^{++}) has configuration $(3d)^9$. There are a few interesting features which can be determined from knowledge of the electronic configuration. Nine electrons occupy the five d orbitals ($d_{xy}, d_{xz}, d_{yz}, d_{z^2}, d_{x^2-y^2}$) making four orbitals doubly occupied and one singly occupied. Therefore for this system the total spin $S = 1/2$ and the electron at the Cu site is magnetic. It was not imaginable that copper, a magnetic atom, could possibly play a role in superconductivity as one would expect magnetism to conflict with the spin-singlet Cooper-pairing. The wavefunctions for the $d_{x^2-y^2}$ orbitals have a small overlap with those on adjacent sites, meaning that the two electrons can pair into either a spin singlet or triplet state.

In addition to unusually high T_c, the cuprates exhibit a complex phase diagram that consists of a magnetic insulator phase, superconductivity, the so-called pseudogap phase, and non-Fermi-liquid behaviour due to strong interactions of the d electrons. There has also been discussions on the possible existence of a quantum critical point inside the superconducting 'dome'. The BCS theory, which is based on a weakly interacting Fermi liquid, is not equipped to describe the properties of such systems. Discovery of the high-temperature cuprates started a revolution in condensed matter research and at present there is no single theory capable of explaining all of these observations, making high-T_c superconductivity one of the most pressing problems in solid state theory.

The strongly correlated nature of the d electrons in the cuprates is what makes research using the usual methods rather difficult. The work horse of condensed matter physics and theoretical chemistry is the density functional theory (DFT) [6] used for performing band

structure calculations. In DFT the electrons are approximated as independent particles, and the electrostatic repulsion among them is replaced by an interaction with an average electron density. This approximation, known as the local density approximation (LDA), effectively reduces the many-body problem down to a single-particle problem and works well when the correlation among electrons is relatively weak, or alternatively, when the electrons have relatively high kinetic energy [7]. The strong electron correlations in the cuprates means that this approximation is no longer valid, and alternatives to the usual DFT calculations need be found.

1.2 Transition Metal Dichalcogenides

Many of the cuprates and recently discovered exotic superconductors exhibit charge density waves (CDW) which can be observed directly by scanning tunneling spectroscopy (STS). The Fermi surface changes across a CDW transition can be probed by angle-resolved photoemission spectroscopy (ARPES) [8, 9] with high precision. In addition, there are some CDW materials which exhibit features common to the cuprates, including "kinks" in the energy-momentum dispersion, anisotropic electron-phonon coupling [10], as well as a pseudogap [11, 12, 13]. There are theories which suggest that some phenomena seen in cuprates could potentially be a manifestation of a CDW in these materials. Therefore, in order to understand the underlying mechanism responsible for high-T_c superconductivity (which is still unknown) it will be instructive to understand possible relationships between superconductivity and electronic instabilities that can cause CDW.

The transition metal dichalcogenides (TMDs) provide an excellent opportunity for studying the interplay of charge density modulations and superconductivity in the context of the conventional BCS theory. These materials show charge density waves [14, 15], and astonishingly become superconductors at lower temperatures. For example, 2H-$TaSe_2$ and 2H-TaS_2 are TMDs which have a charge density wave transitions at $T_{CDW} = 90$K and 75K as well as a superconducting transitions at $T_{SC} = 0.6$K and 0.15K, respectively[16, 17]. TMDs contain chalcogen elements from the oxygen family (oxides are distinguished from chalcogenides) combined with group V metals (i.e., $NbSe_2$, $TaSe_2$, $NbTa_2$, etc., ...). The TMD's form

a layered X-M-X structure where the metal (M) atom is sandwiched between hexagonally packed chalcogen atoms (X). The sandwich-like stacking can be made in a variety of ways and one usually distinguishes between the pure octahedral type (1T) from the pure trigonal prismatic (2H) stacking. In addition, since these layered materials are easy to cleave, they are suitable for surface sensitive measurements such as ARPES and STS, and make an ideal starting point for studying the interplay of CDW and superconductivity.

1.3 Motivation for Research

An especially interesting example of a TMD exhibiting the coexistence of CDW and SC is 2H-$NbSe_2$, which has $T_{CDW} = 33$K and the transition to the superconducting state at $T_{SC} = 7.2$K is well-separated from CDW. This material, although relatively simple in composition, has recently become a source of significant debate in the area of superconductivity. The charge density wave transition has traditionally been understood in terms of a concept originally studied by Peierls [18, 19] called *nesting*. In this model, the existence of parallel sections of the Fermi Surface that can be connected by a common wave vector lead to a periodic lattice distortion, resulting in periodic charge density modulations [20]. One of the predictions of this model is that such "charge density waves" have the periodicity determined by the "nesting (or CDW) wave vector" (which connect parallel portions of the Fermi surface) and a gap should form at the Fermi level. When the material forms CDW, it tends to become an insulator, due to the localisation of the electrons. Such a metal-insulator transition due to the formation of CDW has been observed in many metals. There are, however, several TMDs (including $NbSe_2$) that exhibit somewhat counter-intuitive properties, becoming a *better* conductor upon going through a CDW transition [21]. This unusual behaviour led T.M. Rice and G.K. Scott [1] to formulate a new mechanism for CDWs involving a van Hove singularity near the Fermi Surface. A van Hove singularity is a saddle point in the electron energy-momentum dispersion, and presents itself as a divergence in the density of states. According to this model, vectors which connect vHs's near the Fermi surface can also result in a lattice distortion. In the normal state, the large density of states at the vHs causes electrons to easily scatter to the saddle points. Therefore, removal of states at the

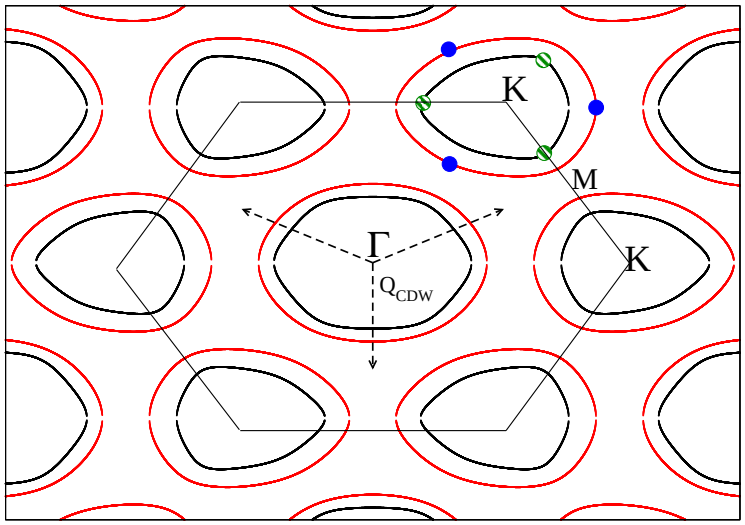

Figure 1.1: $NbSe_2$ Fermi Surfaces showing the double barreled cylinders around Γ and K, as well as the CDW nesting vectors known from neutron scattering experiments[23]. More recent band structure calculations show that there is an additional "pancake"-like structure at Γ, and that the cylinders have small dispersion along k_z. Blue circles represent "hot-spots" determined by Kiss *et al.* [24] while green hatched circles correspond to "hot-spots" measured by Borisenko *et al.*[25]

vHs in the CDW state can enhance the conductivity [22].

Ever since CDW was first observed in $NbSe_2$, there has been ongoing debate regarding the the mechanism for the CDW in this material. The first band structure calculations for $NbSe_2$ were performed by Mattheiss [26] in 1973 and these calculations were able to provide the basic features of the band structure, giving a Fermi surface similar to that shown in Figure 1.1. The Fermi surface of 2H-$NbSe_2$ consists of two sets of cylindrical pockets centered around Γ and K as well as a saddle point singularity at $(1/2)\Gamma K$. The calculations performed by Mattheiss, however, were not selfconsistent, overestimating the depth of the saddle point (∼400 meV below Fermi energy E_F) and showing only two bands crossing the Fermi level. From more recent selfconsistent band structure calculations [27, 28] we now know that there is an additional "pancake"-shaped surface at Γ which has significant k_z dispersion and that the vHs is closer to ≈150 meV below the Fermi energy. Using the band structure results of Mattheiss and the CDW vectors known from neutron scattering measurements ($Q_{CDW} \approx (2/3)\Gamma M$ [23]), J. A. Wilson *et al.* concluded that the CDW in

2H-$NbSe_2$ was a result of Fermi-Surface nesting [17] and that the mechanism of Rice and Scott could be ruled out, as the van Hove singularity was too far away from the Fermi level. It was not until 1999 that the first experimental mapping of the Fermi surface was done by Straub *et al.* using ARPES [29]. This measurement was able to reproduce the bands around Γ and K; however, due to the relatively limited energy and momentum resolution ($\Delta E = 60$ meV and $\Delta\theta = 1.5°$) they were not able to resolve the double-walled nature of the Fermi surfaces. Using the measured Fermi surfaces they also concluded that the CDW was a result of nesting between parallel portions of the hexagonal surfaces around Γ. Although the vHs was closer to E_F than had been thought originally (~ 50 meV), it was still too far for the Rice and Scott mechanism to be a major factor for the CDW transition. A subsequent ARPES measurement by Tonjes *et al.* [30] reached the same conclusion; however, they too were unable to resolve the double walls around Γ and K. Realizing that Fermi surface nesting cannot explain the *reduced* resistivity of 2H-$NbSe_2$ in the CDW state, they suggested that the CDW might be caused by a combination of nesting of the Fermi surfaces and the presence of van Hove singularities.

With the development of more advanced technology and ARPES techniques, all of the expected Fermi surface sheets from the band structure calculations were finally resolved in 2001 [31]. This, as well as other measurements [32], have determined that contrary to the results found by Straub *et al.* the hexagonal Fermi surface at Γ is far too large for nesting with Q_{CDW}. If nesting is indeed the mechanism for the CDW it must be occurring somewhere else in the Brillouin zone. Additionally, with improved energy resolution ($\Delta E = 2.5$ meV and $\Delta\theta = 0.1°$) the superconducting gap has been measured by means of ARPES for the first time [33]. An unexpected result is that the electron-phonon coupling and the superconducting gap have been found to be Fermi-surface sheet dependent, being maximum in particular regions of k-space [10].

This led to another problem for researchers. If nesting was indeed the mechanism responsible for CDW in $NbSe_2$, a gap should open open up in the regions connected by the CDW vectors. The apparent absence of a CDW gap in the ARPES measurements had previously been attributed to the poor energy resolution available at the time. Since the latest ARPES [33] has been able to detect the SC gap in different regions of k-space, the lack of a CDW

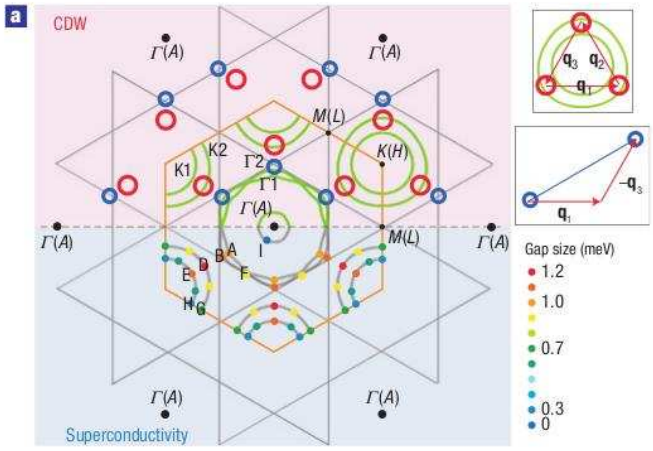

Figure 1.2: Mapping of k-points showing the CDW "hot spots" and k-dependent SC gap [24]. The upper portion corresponds to measurements in the CDW state while the lower portion is in the SC state. Red and blue circles identify "hot spots" which are connected by the primary and secondary CDW vectors, respectively, and coloured dots give the magnitude of the superconducting gap across the Fermi surfaces.

gap was a cause for concern, as the CDW gap was expected to be larger than the SC gap. In order to explain the missing CDW gap, many theories have been proposed ranging from gapless excitations [34] to nesting not being a factor at all in CDW formation [28].

The theory of Rice and Scott based on van Hove singularity has been revived once again in a recent paper by Kiss *et al.* [24] in which they performed high-resolution ARPES measurements of 2H-$NbSe_2$. This experiment has shown that CDW-induced changes of the electronic structure occur only at specific points in k-space, referred to as "hot spots", and the energy points where spectral changes are largest are those at the van Hove singularity. They find the energy of the van Hove singularity (E_{vHs}) to be ~ 35 meV below the Fermi level – close enough that the vHs mechanism for CDW is possible. In addition, the "hot spots" in k space are located on portions of the Fermi surfaces which are closest to the vHs. These points are along ΓK and are shown as blue circles in Figure 1.1. After symmetrizing the "hot spots" to other points in the BZ they have found that these points are connected by precisely the primary and secondary CDW vectors as shown in Figure 1.2. Moreover, the regions of the Fermi surfaces where the CDW-induced changes occur correspond to

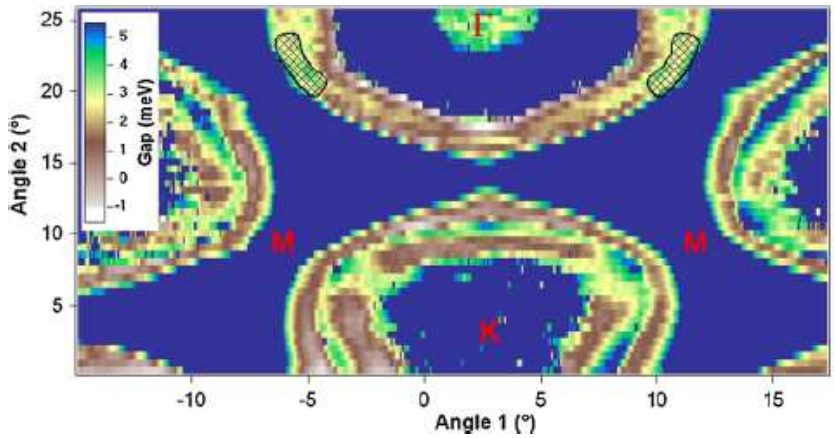

Figure 1.3: Map of the CDW energy gap provided by Borisenko *et al.* [25]. The energy gap breaks the inner K barrel into "arcs" and is maximum along the $K-M-K$ line. These new "hot-spots" are shown in Figure 1.1 as green hatched circles and are also connected by the CDW nesting vectors. Regions where the CDW gap is maximum correspond to regions where the SC energy gap is minimum.

regions where the electron-phonon coupling and the SC energy gap are *maximum*. Although it has been the long standing consensus that CDW (tending towards insulating behaviour) should compete with superconductivity, this result indicates that a CDW can in fact *enhance* superconductivity.

Although these measurements have identified "hot spots" where the CDW induce spectral changes, the CDW energy gap was still not observed in 2H-$NbSe_2$. In a recent paper by Borisenko *et al.* [25] they have used ARPES to perform an "ultra-high" precision mapping of the Fermi surfaces and claim to provide direct measurements of the CDW energy gap for the first time. They found that in contrast to all the previous studies of 2H-$NbSe_2$, none of the proposed nesting scenarios would apply and instead, points along the $K-M-K$ line on the inner K barrel are connected by the CDW vectors. The proposed CDW energy gap seems to support this new scenario, and a plot showing the magnitude of the CDW gap in k-space is presented in Figure 1.3. This figure shows that the CDW gap is maximum at specific k-points in the BZ and breaks the inner K barrel into "arcs". These new "hot spots" are shown in Figure 1.1 as green hatched circles and correspond to regions in k-space where the SC gap is *minimum*. Moreover, temperature-dependent measurements are claimed to show

that the CDW gap persists into the normal state (in analogy with the pseudogap in cuprates) and to explain why previous measurements of the energy gap had been unsuccessful. The results provided by Borisenko *et al.* support the conventional nesting mechanism for the CDW in 2H-$NbSe_2$ and indicate that CDW *competes* with superconductivity.

As has been illustrated, there has been significant debate regarding the nature of the mechanism for the CDW in 2H-$NbSe_2$. To date there is no consensus as to whether the CDW is a result of conventional nesting of the Fermi surfaces, or the vHs scenario proposed by Rice and Scott. The experiments presented above provide strong justification for theoretical studies of charge density modulations and their possible relation with superconductivity, and provide the primary motivation for the research presented in this thesis.

1.4 Layout of Thesis

The remainder of this thesis is organized as follows. In Chapter 2 we review the relevant theoretical background for superconductivity and CDW. Here, emphasis will be given to the different models regarding the mechanism for a CDW instability. The theoretical and computational formulation for our study is presented in Chapter 3. The coexistence of charge density modulations and superconductivity is first examined in Chapter 4 for finite-size systems with inhomogeneity as due to surfaces and impurities, with either s- or d-wave superconductivity. The most significant results of this research are presented in Chapter 5, in which we investigate the mechanism for the CDW instability in our model and study the interplay of charge density modulations with superconductivity. Finally, Chapter 6 discusses the scope of this study and concludes the thesis.

Chapter 2

Theoretical Background

The goal of this chapter is to provide a sufficient background for the theoretical formulation of the research. In this chapter a brief review of the BCS theory of superconductivity is given and its scope and limitations are discussed. In addition an introduction to the theory of charge density wave formation is given. The section concludes with a discussion of the BdG theory and its advantages over the conventional BCS theory.

2.1 BCS Theory of Superconductivity

In the mid 1950's there was a tremendous amount of research and effort put in by the scientific community in order to try and understand the relatively new phenomena of superconductivity. Phenomenological theories due to London, Ginzburg, and Landau were able to provide qualitative predictions; however, a fundamental understanding of the mechanism behind superconductivity was still lacking. It was not until 1957 when Bardeen, Cooper, and Schrieffer (BCS) proposed their theory of superconductivity [35] that the microscopic mechanism of superconductivity could be understood.

The BCS theory of superconductivity is based on the Landau theory of the Fermi liquid, which states that as long as the interactions among electrons do not lead to discontinuous changes in the properties of the system, then a quasiparticle approach is valid. In the normal state (as opposed to the SC state), the strong Coulomb repulsion among electrons is greatly reduced due to screening, and together with the Pauli exclusion principle, its net result is to shift the effective mass of the electron (hence the name "quasiparticle") and change the Fermi-Dirac distribution function around the Fermi energy only slightly. Thus a Fermi liquid consists of free, independent quasiparticles and there is one-to-one correspondence

between a quasiparticle in the "non-interacting" system and an electron in the many-body system. What leads to superconductivity is the residual interactions among the Landau quasiparticles in the normal metal via exchange of phonons. This is the starting point of the BCS theory. The Fermi-liquid theory is then applied to the weak electron-phonon interaction that results in the instability against Cooper-pair formation, and the terminology "quasiparticle" is then used for a single-particle excitation in the superconducting state. For this reason, henceforth the Landau quasiparticles in the normal state are simply referred to as electrons. In conventional superconductors, the energy difference between the SC and normal states is of the order of a few meV, and thus the nature of the correlations pertinent to superconductivity cannot be drastically different above and below the superconducting transition temperature. This justifies the use of the Fermi liquid approach in the BCS theory.

Experimental confirmation of the isotope effect, where the critical temperature of the superconducting transition varies with the ionic mass, motivated studies of electron-phonon interactions in metals. Bardeen and Pines [36] had previously worked on the electron-phonon interaction and found the interaction to have the form

$$H_{el-ph} = \frac{1}{2} \sum_{kk'\sigma\sigma'q} \frac{2\hbar\omega_q |M_q|^2 \hat{c}^\dagger_{k'-q,\sigma'} \hat{c}_{k',\sigma'} \hat{c}^\dagger_{k+q,\sigma} \hat{c}_{k,\sigma}}{(\epsilon_k - \epsilon_{k+q})^2 - (\hbar\omega_q)^2} \,, \tag{2.1}$$

where $c_{k\sigma}$ and $c^\dagger_{k\sigma}$ are the annihilation and creation operators for an electron of momentum k and spin σ. The ϵ_k and $\hbar\omega_q$ are the energy of an electron with momentum k and phonon of momentum q, respectively. Although k and q represent three dimensional vectors, the vector notation (i.e., $\vec{k}$) has been suppressed for simplicity. The isotopic mass dependence is contained in the electron-phonon scattering matrix element M_q. With this interaction in mind BCS were struggling to find a solution to the general Hamiltonian,

$$H = \sum_{k\sigma} \epsilon_k \hat{n}_{k\sigma} + H_{Coul} + H_{el-ph} + H_{Exch} \,, \tag{2.2}$$

where the first term is the kinetic energy of the electron gas, and H_{Coul} and H_{Exch} are the direct Coulomb and exchange interactions, respectively. Cooper noticed that there is a restricted range of energies where H_{el-ph} would be negative, namely,

$$\epsilon_k - \epsilon_{k+q} < \hbar\omega_q \,.$$

For these energies, the electron-phonon interaction contribution to the overall Hamiltonian would be negative and the total ground-state energy of the system would be reduced. Motivated by this result, Cooper began to study a class of matrices where the off-diagonal components were all negative. To his surprise, he found that such a matrix always had at least one bound state (i.e., negative eigenvalue), leading him to study the famous two-pair problem above a filled Fermi sea. The major discovery by Cooper [37] was that there were certain circumstances when the net interaction between the electrons could be *attractive* due to the electron-phonon interaction. If two electrons were interacting above a filled Fermi sea, then these electrons would inevitably form a bound state, now known as a Cooper pair. The binding energy would be maximum for electrons of opposite momenta $(k, -k)$, and the exchange correlation energy would be minimum if they had opposite spins. Thus the ground-state energy of the superconducting state can be minimized if electrons form Cooper pairs (i.e., pairs with $k \uparrow$ and $-k \downarrow$) with zero relative angular momentum, i.e., an s-wave bound state. Instead of trying to solve the full interacting Hamiltonian (2.2), Bardeen, Cooper, and Schrieffer [35] tried to solve a reduced Hamiltonian which consisted of a gas of paired electrons interacting via an attractive potential:

$$H_{red} = \sum_{k\sigma} \epsilon_k \hat{n}_{k\sigma} + \sum_{k,k'} V_{k,k'} \hat{b}_k^\dagger \hat{b}_{k'} \ , \tag{2.3}$$

where $V_{k,k'}$ is assumed to be negative for pairing to occur. The $\hat{b}_k$'s are now Cooper-pair annihilation operators given by $\hat{b}_k = \hat{c}_{-k\downarrow}\hat{c}_{k\uparrow}$. Although the Hamiltonian is reduced, it is still not possible to solve the problem exactly. The real breakthrough for the theory came when Schrieffer suggested a form of coherent-state wavefunction cast in the form of a variational approach. He suggested that the ground-state wavefunction could be written as:

$$|\Psi_0\rangle = \prod_k \left(u_k + v_k \hat{b}_k^\dagger\right) |0\rangle \ , \tag{2.4}$$

where u_k and v_k are the hole and particle amplitudes of a Cooper pair respectively, and $|0\rangle$ is the vacuum state. Orthonormality of the wavefunctions demands that $u_k^2 + v_k^2 = 1$. Schrieffer treated the particle and hole amplitudes as variational parameters under this constraint as well as the constraint that on average the total number of particles in the system is fixed:

$$\langle\Psi_0| \sum_{k\sigma} \hat{n}_{k\sigma} |\Psi_0\rangle = N \, , \tag{2.5}$$

where N is the total number of particles. Using the method of Lagrange multiplier, one minimizes the ground-state energy,

$$\delta W = \delta \left\langle \Psi_0 \right| H_{red} - \mu \hat{N}_{op} \left| \Psi_0 \right\rangle = 0 \,. \tag{2.6}$$

Here $\hat{N}_{op}$ is the operator which counts the number of particles in the many-body system, and μ is the chemical potential. By minimizing this energy in terms of u_k and v_k one finds

$$u_k^2 = \frac{1}{2}\left(1 + \frac{\epsilon_k - \mu}{E_k}\right) , \tag{2.7}$$

$$v_k^2 = \frac{1}{2}\left(1 - \frac{\epsilon_k - \mu}{E_k}\right) , \tag{2.8}$$

$$u_k v_k = \frac{\Delta_k}{2E_k} , \tag{2.9}$$

where

$$E_k = \sqrt{\epsilon_k^2 + \Delta_k^2} \,, \tag{2.10}$$

and Δ_k is called the order parameter. In general it is a function of momentum k, and it must be determined selfconsistently by the so-called gap equation:

$$\Delta_k = -\sum_{k'} V_{kk'} \frac{\Delta_{k'}}{2E_{k'}} \,. \tag{2.11}$$

In their derivation, BCS neglected anisotropic effects for s-wave superconductivity and replaced $V_{k,k'}$ by a constant average-value matrix element. This averaging neglects the details of the band structure, but it was accepted based on the experimental evidence available at the time. Today we know that there are in fact superconductors where anisotropy plays an important role and must be included. The BCS formulation has also been extended to d-wave pairing in high-T_c materials by making the electron-phonon coupling momentum-dependent. For an isotropic s-wave superconductor, the gap equation is reduced to

$$\Delta = -\sum_{k'} V \frac{\Delta}{2E_{k'}}. \tag{2.12}$$

When an electron in state k, σ is added or removed from the superconducting ground-state, the pair state $(k, \sigma; -k, -\sigma)$ is no longer available for pairing due to the Pauli exclusion principle and blocked from coherent scattering among Cooper pairs. When this occurs the pair state is said to be broken, increasing the total energy of the system. By using the

definition of the wavefunction (2.4) and the commutation relations of the pair operators, the ground-state energy of the system is given by

$$E = \langle \Psi_0 | \, H_{red} - \mu \hat{N}_{op} \, | \Psi_0 \rangle = \sum_k 2 \left(\epsilon_k - \mu \right) v_k^2 + \sum_{kk'} V u_k v_k u_{k'} v_{k'} \, . \tag{2.13}$$

By breaking a pair state of momentum k the energy of the system is increased by an amount

$$-2\epsilon_k v_k^2 - 2 \sum_{k'} V u_k v_k u_{k'} v_{k'} \, .$$

To this we must add the kinetic energy of the added electron to get the total change in energy

$$\delta E = \epsilon_k \left[1 - 2 v_k^2 \right] + 2 \Delta u_k v_k \, ,$$

where we have used the gap equation (2.12) to simplify the interaction energy. Using the results in Equations (2.7)-(2.9) the increase in energy becomes (with $\mu = 0$)

$$\delta E = \frac{\epsilon_k^2}{E_k} + \frac{\Delta^2}{E_k} = E_k \, . \tag{2.14}$$

We thus find that E_k is the energy required to break a Cooper pair and create an excitation in state k and Δ is called the energy gap. Adding or removing an electron both break pair states and in fact, both processes are equivalent and cannot be distinguished except that they change the total number of particles N to $N+1$ and $N-1$, respectively. Thus, single-particle excitations in the superconductor are a superposition of an electron and a hole. This is referred to as a *quasiparticle* excitation and has energy E_k.

Excited states of the reduced Hamiltonian can be obtained through a canonical transformation, referred to as the Bogoliubov-Valatin transformation, which diagonalizes the Hamiltonian. These transformations are given by [38]

$$\begin{aligned} \hat{\gamma}_{k\uparrow}^\dagger &= u_k \hat{c}_{k\uparrow}^\dagger - v_k \hat{c}_{-k\downarrow} \, , \\ \hat{\gamma}_{-k\downarrow} &= u_k \hat{c}_{-k\downarrow} + v_k \hat{c}_{k\uparrow}^\dagger \, , \end{aligned}$$

as well as their Hermitian conjugates. When these operators act on $|\Psi_0\rangle$ one finds the

relations,

$$\begin{aligned}
\hat{\gamma}^{\dagger}_{k\uparrow}\,|\Psi_0\rangle &= |\Psi_{k\uparrow}\rangle\ , \\
\hat{\gamma}^{\dagger}_{-k\downarrow}\,|\Psi_0\rangle &= |\Psi_{-k\downarrow}\rangle\ , \\
\hat{\gamma}_{k\uparrow}\,|\Psi_0\rangle &= 0\,, \\
\hat{\gamma}_{-k\downarrow}\,|\Psi_0\rangle &= 0\,.
\end{aligned}$$

Evidently $\hat{\gamma}^{\dagger}_{k\uparrow}$ creates a quasiparticle with momentum k and spin up and $\hat{\gamma}_{-k\downarrow}$ destroys a quasiparticle with momentum $-k$ and spin down in the superconducting state; in either case the total momentum and spin of the system are increased by k and spin one half. The ground-state $|\Psi_0\rangle$ is the vacuum state free of quasiparticles. These elementary excitations are sometimes referred to as *Bogoliubov quasiparticles* or *Bogolons*.

2.2 Charge Density Waves

In the mid 1930s Rudolph Peierls was writing an introductory textbook on the quantum theory of the solid state [18], and was in the process of designing a many-body exercise when he made an accidental discovery. He was considering the following question; what would happen if the crystal lattice could be distorted so that the size of the unit cell was effectively doubled? It was well established that a periodic potential in the lattice causes a gap due to a level splitting to form at the edge of the Brillouin zone. (In a one dimensional lattice of lattice spacing a the gap is at k = π/a). Doubling the size of the unit cell, he thought, should effectively halve the size of the Brillouin zone and the gap would now open at $\pi/2a$ as illustrated in Figure 2.1. If the metal had enough electrons so that the energy band was half filled (half-filling), the Fermi level would also be at $\pi/2a$. He wanted to know if the energy saved by the gap opening at the Fermi level was more than the energy cost to distort the lattice in the first place. To his complete surprise [19] this distortion of the lattice was *always* energetically favourable, and such a metal would undergo what is now known as the Peierls transition. Since the distortion of the lattice causes the electron density to distort in a periodic fashion, it is also known as a charge density wave transition (CDW).

Intuitively one can see that the formation of a charge density wave is dependent on

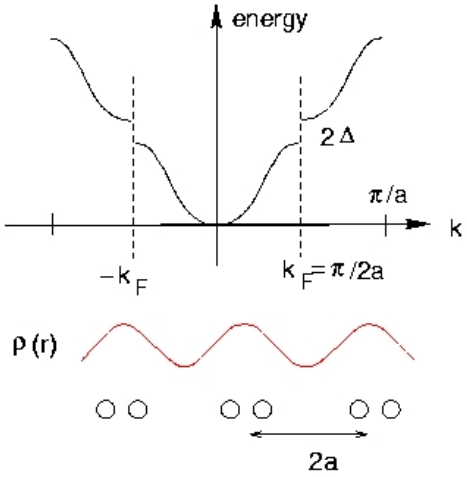

Figure 2.1: Peierls' construction of a charge density wave. By distorting the lattice one can move the energy gap from the zone boundary to $\pi/2a$. For a half-filled band this corresponds to the Fermi level. This lattice distortion causes a periodic modulation of the electron density, the wavelength of which is dependent on k_F.

the distortion of the lattice, and therefore the CDW is intimately tied with the electron-phonon interactions. Physically, the CDW is induced as a result of electrons overscreening the potential induced by the lattice of ions. The dielectric response of a gas of electrons characterizes how the gas will respond to an external potential, and in general is frequency- and wavevector-dependent. Therefore the behaviour of the dielectric response can provide insight into density wave formation. A useful approximation which can characterize many metals is given by Equation (2.15) and is known as the Lindhard equation for the dielectric response of an electron gas [39]:

$$\epsilon(\vec{q},\omega) = 1 - \lim_{\alpha\to 0} \frac{e^2}{V_g \epsilon_0 q^2} \sum_{\vec{k}} \frac{f_o(\vec{k}+\vec{q}) - f_o(\vec{k})}{E(\vec{k}+\vec{q}) - E(\vec{k}) - \hbar\omega - i\hbar\alpha} \ . \tag{2.15}$$

In this equation $f_o(\vec{k})$ is the Fermi-Dirac distribution function at energy $E(\vec{k})$, V_g is the volume of the unit cell, and q and ω are the space and time Fourier components of a general time-dependent external potential. The Lindhard equation characterizes how the electron gas will respond to an external potential, and for CDW formation this potential is a result of phonon effects in the lattice. For CDW we are interested in the response for a frozen-in

periodic lattice distortion, therefore the quantity of interest is $\epsilon(\vec{q}, \omega = 0)$.

A divergence in the response indicates that the electron gas is unstable and electrons will move to overscreen the potential. As Johannes *et al.* have emphasized [28, 40], although the response has real and imaginary parts, it is the *real* part that defines a CDW instability. As the imaginary part vanishes as $\alpha \rightarrow 0$, it is the real part shown in Equation (2.16) which contains relevant information from within an energy window $E(\vec{k} + \vec{q}) - E(\vec{k})$. It is interesting to note that a divergence in the dielectric response can also be the origin of the so-called Kohn Anomaly [41]. In real metals the electron-phonon interaction is replaced by a screened interaction, which depends on the dielectric response $\epsilon(\vec{q}, \omega)$. The singularity which develops in the dielectric response means that this screening changes rather sharply for specific wavevectors $\vec{q}$. Therefore, the divergence of the dielectric response manifests itself as a dip in the phonon frequency spectrum at $q = 2k_F$, resulting in the Kohn Anomaly.

$$Re\ \epsilon(\vec{q}, \omega = 0) = 1 - \lim_{\alpha \rightarrow 0} \frac{e^2}{V_g \epsilon_0 q^2} \sum_{\vec{k}} \frac{\Big(f_o(\vec{k} + \vec{q}) - f_o(\vec{k})\Big)\Big(E(\vec{k} + \vec{q}) - E(\vec{k})\Big)}{\Big(E(\vec{k} + \vec{q}) - E(\vec{k})\Big)^2 + (\hbar\alpha)^2} \tag{2.16}$$

For a time-independent perturbation the most dominant contributions to the sum in (2.16) occur when $E(\vec{k} + \vec{q}) - E(\vec{k}) = 0$, and in a one-dimensional metal the response diverges whenever $q = 2k_F$. That is, when two states spanned by the same wavevector q have the same energy, the sum diverges, and the system becomes unstable towards a periodic lattice distortion. Constant energy surfaces connected by a common wavevector is an effect referred to as *nesting*, and in general depends on the particular topology of the Fermi surface. There are many metals for which conduction occurs along "chains" and their energy dispersion can be approximated as being one-dimensional. Thus, 3D metals with a "one-dimensional" energy dispersion have a Fermi surface consisting of 2 parallel planes at $k = \pm k_F$. An electron at $k = -k_F$ and a hole at $k = +k_F$ have the same energy and are separated by $q = 2k_F$. The wavevectors q which connect these points are referred to as nesting vectors. Since there are an infinite number of these points in such a "one-dimensional" metal the response is strongly divergent, and this is referred to as "perfect nesting" of the Fermi surface. This is the reason why materials which exhibit CDW typically contain chains of atoms. For dispersions in higher dimensions, however, the number of parallel points is

reduced as illustrated in Figure 2.2. The reduction of the number of nested points from two to three dimensions is significant, and there are very few "three-dimensional" metals which exhibit CDW. Since the cuprates and transition metal dichalcogenides are essentially "two-dimensional" metals, there is potential for nesting to be significant in these materials.

It is important to keep in mind that a divergence in (2.16) implies that the electron gas is unstable towards density wave formation. In a real system, where the lattice of ions is dynamic, nuclei may respond in such a way that a frozen in lattice distortion (zero phonon mode) may not occur. In addition there may be so-called soft phonon modes for which the eigenvalue of the electron-phonon scattering matrix vanishes. Such a zero-phonon mode can cause CDW without a divergence in the dielectric response at all. Thus, although a divergence in (2.16) provides strong criteria for a CDW instability, it does not necessarily guarantee whether a CDW will form in a physical material.

Although conventional nesting is responsible for density wave formation in many metals, it is not the only scenario in which a CDW can occur. In an article by Rice and Scott [1] it was shown that any vector Q_{sp} in momentum space which connects two saddle points close to the Fermi energy can also lead to a divergence in the dielectric susceptibility. Points connected by Q_{sp} have the same energy, and as a result of the saddle points there will be a very large density of states at this energy. This theory is particularly appealing as it provides a plausible explanation as to why many of the transition metal dichalcogenides become *better* conductors in the CDW state. In the normal state the large density of states at the vHs causes electrons to easily scatter to the saddle point. Therefore the removal of states at the

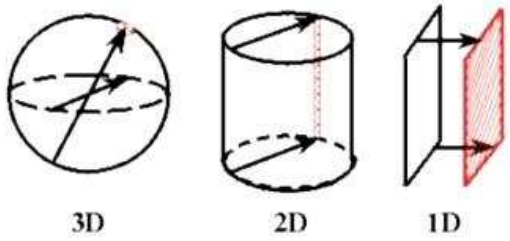

Figure 2.2: Fermi surface nesting for a three-dimensional material with 1-,2- and 3-dimensional energy dispersion. The number of points which lead to divergent terms in the response is strongly reduced in three dimensions [42].

vHs in the CDW state would enhance the conductivity.

If a material has both Fermi-surface nesting as well as a saddle point in the vicinity of the Fermi energy, the divergence in (2.16) due to the van Hove singularity will multiply the divergence due to nesting. When this happens, it is not clear which mechanism is responsible for the CDW. It is reasonable to assume that the mechanism resulting in the most dominant divergence in the response is the dominant cause for the CDW instability; although, it can be a combination of both. For the transition metal dichalcogenides the Fermi surface contains both features, and there has been considerable debate regarding whether nesting or the vHs mechanism is responsible for CDW in these metals.

2.3 BdG Theory

Although the BCS theory (which is formulated in momentum space) has been very successful in describing isotropic and homogeneous superconductors, it suffers in that it cannot describe superconductivity in the presence of inhomogeneity, where the order parameter varies spatially. The Ginzburg-Landau theory [43] allows one to calculate spatial variation of the macroscopic wavefunction of Cooper pairs. This phenomenological theory, however, cannot describe SC on the scale smaller than the coherence length (roughly the size of a Cooper pair), and is also only valid for temperatures near T_c. To understand the fundamental properties of superconductors on the microscopic scale, a generalization of the BCS theory is necessary. In the presence of a surface or an impurity, momentum is no longer a good quantum number and the Hamiltonian must be formulated in real space. This allows the study of spatial variation of the order parameters. There are two theoretical approaches which have been developed to study inhomogeneous systems. One is due to Gorkov [44] and uses the equations of motion for the Green functions, and the second approach is due to de Gennes [45] which is based on the quasiparticle wavefunctions. In the Bogoliubov de-Gennes (BdG) formalism one starts with a real-space mean-field Hamiltonian and diagonalizes it by means of a unitary transformation. The mean fields are then determined by variationally minimizing the free energy. The BdG equations are a generalization of the BCS theory, therefore for a homogeneous system they are equivalent. The tight-binding formalism is well

suited for numerical calculations on a lattice as it allows one to control the band structure, electron filling, and many other quantities unlike the free electron gas model. Combined with the BdG formulation it provides a powerful tool for studying superconductivity in metals. For this reason it is the tight-binding and BdG formalisms which we adopt for our studies.

Chapter 3

Formulation

3.1 Extended-Hubbard Hamiltonian

The DFT with LDA breaks down for systems where the correlation effects are dominant, such as the $3d$ transition metals. The most notable example of such a system is NiO, which according to the independent electron approximation should be a metal since it contains a d band that is not completely filled [46]. It turns out, however, that the actual NiO is an insulator. The explanation for this was first given by Mott in 1949. The electrostatic repulsion among electrons with overlapping orbitals will cause them to become localized at the lattice sites, reducing their kinetic energy. When this happens, there is a competition between the Coulomb repulsion and kinetic energy that is not accounted for within the conventional LDA. For example, if we have two electrons with the same spin, they cannot occupy the same lattice site (due to the Pauli exclusion principle) and so the Coulomb repulsion energy in this case is relatively low. However, if they were to have opposite spins, the electrons *can* occupy the same site and this would cause a large Coulomb repulsion between the electrons. If the Coulomb energy is comparable to the kinetic energy gain of the electron (which can be the case in the $3d$ transition metals), then transport may not occur and the system becomes insulating. Mott and Hubbard proposed a model to account for such electron correlations by adding an extra term to the LDA approximation, sometimes referred to as an LDA+U model.

The Mott-Hubbard Hamiltonian can be extended to study superconducting systems by using an *attractive* potential between electrons of opposite spins which occupy the same site. This so-called Hubbard model is a minimal model for s-wave superconductivity that arises

from isotropic electron-phonon interactions. To study the high-temperature superconductors which have d-wave symmetry the Hubbard Hamiltonian can be extended to include longer range interactions between electrons occupying neighbouring sites. Such an extended Hubbard Hamiltonian can be written as

$$H_0 = \sum_{\langle ij\rangle\sigma} t_{ij} c^{\dagger}_{i\sigma} c_{j\sigma} + \sum_{i\sigma} (\epsilon_i - \mu)\, \hat{n}_{i\sigma}\,, \tag{3.1}$$

$$H = H_0 + \sum_i U_{ii} \hat{n}_{i\uparrow} \hat{n}_{i\downarrow} + \frac{1}{2} \sum_{\langle ij\rangle} \sum_{\sigma\sigma'} U_{ij} \hat{n}_{i\sigma} \hat{n}_{j\sigma'}\,. \tag{3.2}$$

The single-particle Hamiltonian H_0 describes a non-interacting electron gas on a lattice. The electrons are modelled as having the kinetic energy that allows them to "hop" from site to site in the lattice. This is represented by the electron creation and annihilation operators which removes an electron at site j and creates an electron at site i with hopping amplitude t_{ij} and spin σ. In this thesis we first assume that electrons only hop between nearest-neighbour sites, and then in Chapter 5 the hopping will be extended to next-nearest neighbours as well. The neighbour sites are represented by the sum over $\langle i, j\rangle$ (which should be read as the sum over all sites i and all sites j which are nearest neighbours to i). The remaining terms in the single-particle Hamiltonian are the local on-site potentials. The chemical potential, μ, specifies the filling of the system (since in a tight-binding model you can control the filling of the band), while ϵ_i is a single-particle impurity potential which allows for the study of an impurity deposited at any site i in the lattice. The total Hamiltonian is the sum of the single-particle Hamiltonian as well as the interactions among electrons as shown in Equation (3.2). The U_{ii} term represents an attractive s-wave interaction between two electrons of opposite spins occupying at the same site, while the U_{ij} term represents a longer-range interaction such as d-wave coupling between electrons occupying neighbouring sites. The extended Hubbard Hamiltonian is formulated in real space and provides the starting point for our calculations.

3.2 Mean-Field Decomposition

The Hamiltonian in Equation (3.2) is exact and due to the two-body interaction terms, is difficult, if not impossible, to solve exactly. As a result one must introduce an effective

Hamiltonian in order to approximate the two-body interactions. To this end we apply a mean-field method, where the two-body interactions are replaced with a one-body interaction multiplied by a mean-field which needs to be solved selfconsistently. In the mean-field approximation a two-body operator such as $\hat{n}_{i\uparrow}\hat{n}_{i\downarrow}$ is replaced by its average value plus fluctuations about the average. Fluctuations higher than the second order are neglected in this approximation. The on-site interaction operator becomes

$$\hat{n}_{i\uparrow}\hat{n}_{i\downarrow} = \left\langle \hat{c}^{\dagger}_{i\uparrow}\hat{c}_{i\uparrow}\hat{c}^{\dagger}_{i\downarrow}\hat{c}_{i\downarrow} \right\rangle + \left(\hat{c}^{\dagger}_{i\uparrow}\hat{c}_{i\uparrow}\hat{c}^{\dagger}_{i\downarrow}\hat{c}_{i\downarrow} - \left\langle \hat{c}^{\dagger}_{i\uparrow}\hat{c}_{i\uparrow}\hat{c}^{\dagger}_{i\downarrow}\hat{c}_{i\downarrow} \right\rangle \right). \tag{3.3}$$

The expectation value of a product of four operators can be evaluated using Wick's Theorem. For an arbitrary operator $\Psi(i)$ Wick's theorem states that the expectation value is given by

$$\begin{aligned} \left\langle \Psi^{\dagger}(1)\Psi^{\dagger}(2)\Psi(3)\Psi(4) \right\rangle &= \left\langle \Psi^{\dagger}(1)\Psi(4) \right\rangle \left\langle \Psi^{\dagger}(2)\Psi(3) \right\rangle \\ &- \left\langle \Psi^{\dagger}(1)\Psi(3) \right\rangle \left\langle \Psi^{\dagger}(2)\Psi(4) \right\rangle \\ &+ \left\langle \Psi^{\dagger}(1)\Psi^{\dagger}(2) \right\rangle \left\langle \Psi(3)\Psi(4) \right\rangle . \end{aligned} \tag{3.4}$$

Therefore the mean-field decomposition of the four electron operators is

$$\begin{aligned} \left\langle \hat{c}^{\dagger}_{i\uparrow}\hat{c}^{\dagger}_{i\downarrow}\hat{c}_{i\downarrow}\hat{c}_{i\uparrow} \right\rangle = & \left\langle \hat{c}^{\dagger}_{i\uparrow}\hat{c}_{i\uparrow} \right\rangle \left\langle \hat{c}^{\dagger}_{i\downarrow}\hat{c}_{i\downarrow} \right\rangle \\ &- \left\langle \hat{c}^{\dagger}_{i\uparrow}\hat{c}_{i\downarrow} \right\rangle \left\langle \hat{c}^{\dagger}_{i\downarrow}\hat{c}_{i\uparrow} \right\rangle \\ &+ \left\langle \hat{c}^{\dagger}_{i\uparrow}\hat{c}^{\dagger}_{i\downarrow} \right\rangle \left\langle \hat{c}_{i\downarrow}\hat{c}_{i\uparrow} \right\rangle . \end{aligned}$$

In this study we are considering only non-magnetic interactions, therefore the second term in the expansion above is taken to be zero. Performing a similar decomposition for the off-site interaction terms (considering only singlet pairing) yields the mean-field Hamiltonian,

$$\begin{aligned} H_{eff} = & H_0 + \sum_{i\sigma} V^{(H)}_{ii}\hat{n}_{i\sigma} + \frac{1}{2}\sum_{\langle ij\rangle\sigma} V^{(H)}_{ij}\hat{n}_{i\sigma} - \frac{1}{2}\sum_{\langle ij\rangle\sigma} V^{(F)}_{ij}c^{\dagger}_{i\sigma}c_{j\sigma} \\ & + \sum_{i} \Delta_{ii}c^{\dagger}_{i\uparrow}c^{\dagger}_{i\downarrow} + \frac{1}{2}\sum_{\langle ij\rangle} \Delta_{ij}c^{\dagger}_{i\uparrow}c^{\dagger}_{j\downarrow} + H.c. \end{aligned} \tag{3.5}$$

The mean fields are defined as

$$
\begin{aligned}
V_{ii}^{(H)} &= U_{ii} \left\langle \hat{c}_{i\sigma}^{\dagger} \hat{c}_{i\sigma} \right\rangle && (3.6)\\
V_{ij}^{(H)} &= U_{ij} \left\langle \hat{c}_{j\sigma}^{\dagger} \hat{c}_{j\sigma} \right\rangle && (3.7)\\
V_{ij}^{(F)} &= \frac{1}{2} U_{ij} \left[\left\langle \hat{c}_{j\sigma}^{\dagger} \hat{c}_{i\sigma} \right\rangle + \left\langle \hat{c}_{i\sigma}^{\dagger} \hat{c}_{j\sigma} \right\rangle \right] && (3.8)\\
\Delta_{ii} &= U_{ii} \left\langle \hat{c}_{i\downarrow} \hat{c}_{i\uparrow} \right\rangle && (3.9)\\
\Delta_{ij} &= \frac{1}{2} U_{ij} \left[\left\langle \hat{c}_{j\downarrow} \hat{c}_{i\uparrow} \right\rangle + \left\langle \hat{c}_{i\downarrow} \hat{c}_{j\uparrow} \right\rangle \right] , && (3.10)
\end{aligned}
$$

where σ is the spin of the electron, either up or down. The first two fields are the on- and off-site Hartree potentials, and the third term is the Fock potential due to the exchange interaction between electrons on neighbouring sites. Finally, we have the on- and off-site pairing potentials that correspond to the s-wave and d-wave order parameters, respectively. It should be emphasized that the Hartree-Fock mean-fields *need* be included selfconsistently for studies of density modulations on the atomic scale. These electron correlations, though important, are often simply neglected due to a significant increase in computational demand by including these terms. The rationale behind this is that it is commonly thought that the net effect of the Hartree-Fock mean-fields is to shift the chemical potential and nearest-neighbour hopping amplitudes. For systems with nanoscale or atomic-scale inhomogeneity and charge density modulations, however, this is not the case and these terms cannot be ignored. In fact, it is crucial to solve for the Hartree-Fock potentials selfconsistently as well as the order parameters in understanding superconductivity in an inhomogeneous system. These terms are also important for solving the number equation, as they also determine the filling of the bands.

3.3 BdG Equations

The mean-field Hamiltonian in Equation (3.5) now only contains single-particle operators and can be diagonalized via a canonical transformation. This can be done using the Bogoliubov-Valatin transformation as described in Section 2.1. The electron annihilation operators are

transformed as

$$\hat{c}_{i\uparrow} = \sum_n \left(\gamma_{n\uparrow} u_n(i) - \gamma^\dagger_{n\downarrow} v^*_n(i) \right) , \tag{3.11}$$

$$\hat{c}_{i\downarrow} = \sum_n \left(\gamma_{n\downarrow} u_n(i) + \gamma^\dagger_{n\uparrow} v^*_n(i) \right) , \tag{3.12}$$

where u_n and v_n are complex numbers, and the operators $\gamma_{n\sigma}, \gamma^\dagger_{n\sigma}$ describe a quasiparticle in state n with spin σ. These quasiparticle operators diagonalize the effective Hamiltonian,

$$H_{eff} = E_0 + \sum_{n\sigma} \epsilon_n \gamma^\dagger_{n\sigma} \gamma_{n\sigma} , \tag{3.13}$$

where E_0 is the ground-state energy, and ϵ_n is the energy of a quasiparticle excitation in state n. As shown in Appendix A this implies,

$$\left[H_{eff}, \gamma_{n\sigma} \right] = -\epsilon_n \gamma_{n\sigma} , \tag{3.14}$$

$$\left[H_{eff}, \gamma^\dagger_{n\sigma} \right] = \epsilon_n \gamma^\dagger_{n\sigma} . \tag{3.15}$$

Since the form of the operators must be invariant under a canonical transformation, the quasiparticle operators must also obey the fermion anti-commutation relations,

$$\left\{ \gamma_{m\sigma} \gamma^\dagger_{n\sigma'} \right\} = \delta_{mn} \delta_{\sigma\sigma'} , \tag{3.16}$$

$$\left\{ \gamma_{m\sigma} \gamma_{n\sigma'} \right\} = 0 , \tag{3.17}$$

$$\left\{ \gamma^\dagger_{m\sigma} \gamma^\dagger_{n\sigma'} \right\} = 0 . \tag{3.18}$$

For a superconductor at finite temperature the quasiparticle operators also obey the Fermi-Dirac statistics,

$$\left\langle \gamma^\dagger_{m\sigma} \gamma_{n\sigma'} \right\rangle = \delta_{mn} \delta_{\sigma\sigma'} f_n , \tag{3.19}$$

$$\left\langle \gamma_{m\sigma} \gamma_{n\sigma'} \right\rangle = 0 , \tag{3.20}$$

where $f_n \equiv f(\epsilon_n)$ is the Fermi-Dirac distribution function evaluated at energy ϵ_n. Equation (3.16) with $m = n$ and $\sigma = \sigma'$ implies that $|u_n|^2 + |v_n|^2 = 1$, which is consistent with the result from the BCS theory for a homogeneous system. By evaluating the commutators in Equations (3.14) and (3.15), and using the transformations (3.11) and (3.12), one arrives at

the Bogoliubov-de Gennes (BdG) equations:

$$\begin{pmatrix} \hat{T} + \hat{V}^{(H)} + \hat{V}^{(F)} & \hat{\Delta} \\ \hat{\Delta}^* & -\left(\hat{T}^* + \hat{V}^{(H)} + \hat{V}^{(F)}\right) \end{pmatrix} \begin{pmatrix} u_n \\ v_n \end{pmatrix} = \epsilon_n \begin{pmatrix} u_n \\ v_n \end{pmatrix}, \tag{3.21}$$

where $\hat{T}$ is the kinetic energy matrix, and $\hat{V}^{(H)}$ and $\hat{V}^{(F)}$ are the Hartree and Hartree-Fock potentials, and u_n and v_n are the particle and hole amplitudes of the quasiparticle excitations, respectively. For a lattice with N sites the BdG equations form a $2N \times 2N$ eigenvalue problem, where excitation energies are the eigenvalues and the particle-hole amplitudes are the eigenvectors. Written in this form it is evident that the pairing potentials $\hat{\Delta}$ couple the particle and hole amplitudes, and if $\hat{\Delta} = 0$ (i.e., the normal state) then the two amplitudes are independent and each state is either a particle or a hole state. This corresponds to the Hartree-Fock equations for an electron and for a hole.

The mean fields in (3.21) are determined by minimizing the free energy of the system. In analogy with the BCS theory, we use u_n and v_n as variational parameters and perform the minimization under the constraint that quasiparticle wave functions are normalized,

$$\delta F = \delta \langle H_{eff} \rangle - T\delta S = 0\,, \tag{3.22}$$

which provides a set of selfconsistent equations for the mean fields. Here δF and δS are a change in the free energy and entropy, respectively. In terms of the particle and hole amplitudes they are given by

$$V_{ij}^{(H)} = U_{ij} \sum_n \left[\, |u_n(j)|^2 f_n + |v_n(j)|^2 (1 - f_n) \,\right], \tag{3.23}$$

$$\Delta_{ij} = -\frac{1}{2}\, U_{ij} \sum_n \left[\, u_n(i) v_n^*(j) + u_n(j) v_n^*(i) \,\right] (1 - 2f_n)\,, \tag{3.24}$$

which are valid for either $j = i$ or $j \neq i$. The notation f_n represents the Fermi-Dirac distribution function for energy ϵ_n. The Fock potential is defined as

$$V_{ij}^{(F)} = \frac{1}{2}\, U_{ij} \sum_n \left[\, \left(u_n^*(i) u_n(j) + u_n(i) u_n^*(j)\right) f_n + \left(v_n(i) v_n^*(j) + v_n^*(i) v_n(j)\right) (1 - f_n) \,\right]. \tag{3.25}$$

The mean-field potentials are defined in terms of the particle and hole amplitudes and energies, and as a result the BdG equations (3.21) represent a set of Schrödinger-like equations

which must be solved selfconsistently until the mean-field potentials converge. Since the electron creation and annihilation operators are defined in terms of the quasiparticle amplitudes, any physical observable can be calculated in terms of the eigenvalues and eigenvectors. For example it is possible to determine the average electron density at each site in the lattice, since $\langle n_i \rangle = \sum_\sigma \langle \hat{c}^\dagger_{i\sigma} \hat{c}_{i\sigma} \rangle$. In terms of the solutions of the BdG equations this is

$$\langle n_i \rangle = 2 \sum_n \left[\, |u_n(i)|^2 + |v_n(i)|^2 (1 - f_n) \, \right] . \tag{3.26}$$

Two particularly useful physical observables that can be calculated are the ground-state energy of the system and the local density of states (LDOS). Since the LDOS is what is measured by scanning tunnelling spectroscopy (STS) it will be a convenient tool for analyzing the results of our model. Using the same technique to determine the electron density, the ground-state energy for the Hubbard Hamiltonian with on-site and off-site interactions is given by

$$\begin{aligned} \langle H_{eff} \rangle =& 2 \sum_{\langle ij \rangle} \left(t_{ij} - \frac{1}{2} V^{(F)}_{ij} \right) \frac{V^{(F)}_{ij}}{U_{ij}} + \sum_i \left(\epsilon_i - \mu + V^{(H)}_{ii} \right) \langle \hat{n}_i \rangle \\ & + 2 \sum_i \frac{|\Delta_{ii}|^2}{U_{ii}} + \frac{1}{2} \sum_{\langle ij \rangle} V^{(H)}_{ij} \langle \hat{n}_i \rangle + \sum_{<ij>} \frac{|\Delta_{ij}|^2}{U_{ij}} \, . \end{aligned} \tag{3.27}$$

The local density of states is

$$A_i(\omega) = \sum_n |u_n(i)|^2 \, \delta(\omega - \epsilon_n) + |v_n(i)|^2 \, \delta(\omega + \epsilon_n) \tag{3.28}$$

where $u_n(i)$ and $v_n(i)$ are the particle and hole amplitudes at site i for energy ϵ_n. In these equation $\delta(\omega)$ is the Dirac delta function. The BdG equations are solved exactly, and as a result have a very high numerical demand. To solve these equations I have developed parallel algorithms designed to perform such calculations quickly and efficiently. The calculation have been performed on a largescale Beowulf-class PC cluster, *iglu*, here at the U of S. Iglu has 128 Intel Xeon processors clocked at 3.06 GHz, each with 2 GB RAM. Matrix diagonalization has been performed with the Scalable Linear Algebra Package (ScaLAPACK) designed for use on distributed-memory parallel computers. Details of the derivation of the BdG equations and the outline of the numerical algorithms are presented in Appendices A and B, respectively.

Chapter 4

Surfaces and Impurities in Nanoscale Systems

In this chapter we first investigate the effects of inhomogeneity as due to the presence of a surface or an impurity, or finite size of the sample on both s-wave and d-wave superconductivity. In particular, quantum interference effects in nanoscale superconductors are studied, in which the influence of surface boundaries and even a single impurity can dominate over the entire sample. The presence of a boundary or an impurity tends to trigger charge density modulations and inhomogeneous superconductivity. We begin with a study of pure finite-size systems and demonstrate that s-wave SC is quite robust against the presence of a surface and can in fact coexist with CDW, while d-wave SC is not. We will then examine the effects of a single impurity deposited onto the centre of a nanoscale sample. The results presented in this chapter have not only a potential impact on nanotechnology, but also give us interesting insight into the interplay of CDW and SC.

4.1 Degenerate SC and CDW State

The presence of a surface can lead to interesting behaviours of s-wave and d-wave superconductors. First we study a pure s-wave superconductor of finite size (20x20 atomic lattice) with on-site electron-phonon coupling $U_{ii} = -1.5t$ at half filling (meaning that the total number of electrons is the same as the number of lattice sites, hence one electron per site on average). What is remarkable about this system is that there are three degenerate ground-states: the superconducting state with uniform density (SC), a CDW state with no superconductivity (CDW), as well as the state in which CDW and SC coexist (CDW+SC).

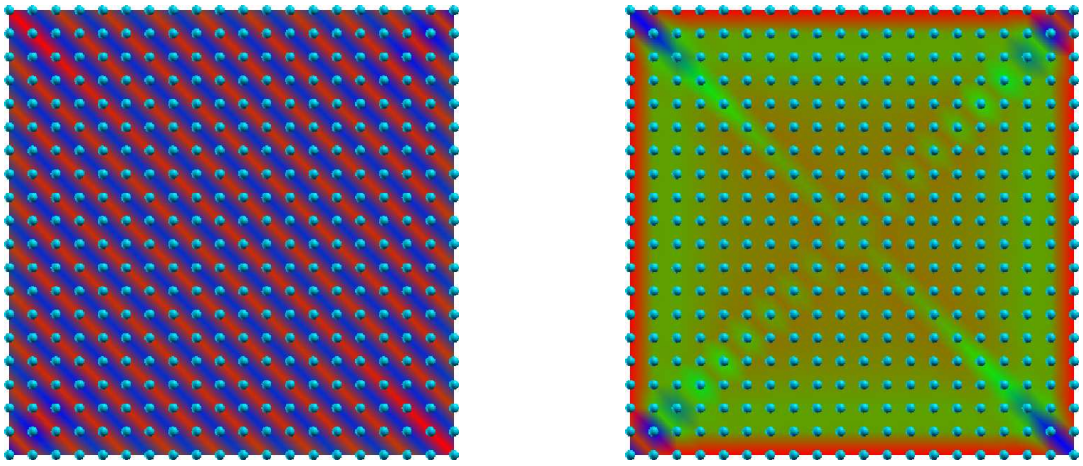

Figure 4.1: (a) Electron density for a 20x20-site s-wave superconductor at half filling. On-site coupling is $U_{ii} = -1.5t$. The CDW+SC state is degenerate with the SC state that has uniform density density distribution. (b) S-wave order parameter for the system described in (a). The order parameter shows slight suppression along the boundaries due to the loss of kinetic energy, but the presence of a surface is not a pair-breaking process in s-wave superconductors.

These states all have exactly the *same* ground-state energy and critical temperature, but with different electron density distribution. The electron density and order parameter for the CDW+SC state are shown in Figures 4.1 (a) and (b), respectively. In these figures red indicates suppression (or minimum value) and blue means enhanced (maximum value). In the mixed state (SC+CDW) the SC order parameter is suppressed compared to the homogeneous density state (SC) as shown in Figure 4.2. This intriguing result indicates that contrary to usual expectations a CDW can in fact coexist with SC. In this figure, it can be seen clearly that the density modulations of CDW and the SC order parameter vanish at the same T_c. Figure 4.1 (b) also illustrates that the CDW amplitude in the mixed (CDW+SC) state is suppressed compared to the pure (i.e., no SC) state.

This result also emphasizes the significance of the Hartree-Fock interactions in Equation (3.6). If this term is not included when solving the mean-field equations a CDW solution cannot be found and a uniform density distribution with increased ground-state energy would always result. Including these terms allows the electrons to "feel the presence" of the other electrons via exchange of phonons without anomalous coupling, and can gain energy by formation of a charge density wave. It is clear that an inhomogeneous density distribution can be induced by surfaces in a small superconductor. Naturally, an electron at the boundary will

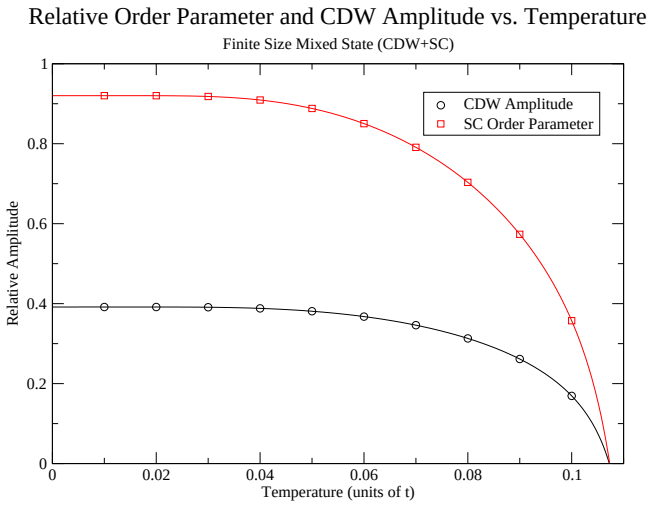

Figure 4.2: Plot of the relative CDW amplitude and SC order parameter as a function of temperature in an s-wave superconductor described in Figure 4.1(a). Amplitudes are taken with respect to the pure SC and CDW states. The CDW and SC states clearly have the same transition temperatures; however, the amplitude of the order parameter in the CDW+SC state is suppressed by $\sim 8\%$ with respect to the SC state. Additionally, the amplitude of the density modulations in the CDW+SC state is suppressed by $\sim 60\%$ with respect to the pure CDW state.

lose some kinetic energy as it can no longer "hop" past the surface. The pairing interaction, however, is local (on-site in our model) in s-wave superconductors and does not extend to nearest-neighbours, making s-wave superconductivity quite robust against the presence of a surface. Along the boundary there is now a competition set up between the kinetic energy loss due to being near the surface versus the pairing energy gained by forming a Cooper pair, and at a corner the loss in kinetic energy is doubled. The tendency of electrons to avoid corners in order to minimize loss in their kinetic energy results in a smaller average density at the four corners, thus triggering a CDW across the whole sample.

4.2 D-Wave SC Sensitive to Surfaces

In a d-wave superconductor the situation is quite different from the s-wave case. Again for this system we model a pure d-wave superconductor with off-site electron-phonon coupling $U_{ij} = -1.5t$ ($U_{ii} = 0$) in a finite size (19x19) lattice at half filling. The electron density and order parameter are shown in Figures 4.3 (a) and (b), respectively. In the case of d-

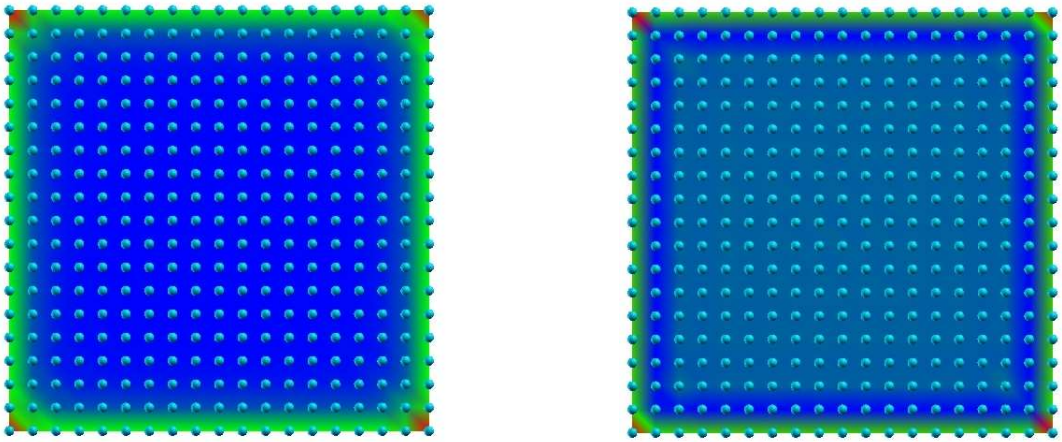

Figure 4.3: (a) Electron density for a pure 19x19-site d-wave superconductor at half filling. Off-site coupling is $U_{ij} = -1.5t$. The density is suppressed all along the boundaries, uniformly except for the four corners, and CDW-like density modulations are no longer favoured in the ground-state. (b) D-wave order parameter for the system described in (a). Similarly to the average density distribution, the d-wave order parameter is suppressed on the surfaces.

wave superconductivity, due to nearest-neighbour electron-phonon coupling, across a surface the electrons not only lose kinetic energy, but also interaction energies (both Hartree-Fock and pairing energies). Thus a surface is always pair-breaking and tends to suppress d-wave superconductivity. This is reflected in the electron density distribution shown in Figure 4.3 (a), where the density is overall suppressed all along the boundaries (suppression is the largest at the corners), and obviously a CDW cannot be formed. Also due to the loss of nearest-neighbour interactions, the order parameter is smaller (i.e., less superconducting ordering) along the boundaries (Figure 4.3 (b)). These results indicate that d-wave superconductivity is very sensitive to the presence of a surface and will be an important constraint for surface-sensitive measurements or developing nanoscale devices.

4.3 S-Wave SC with Single Impurity

We would now like to consider the effects of a single impurity deposited at the centre of a nanoscale superconductor. In this regard we model an s-wave superconductor with on-site electron-phonon coupling $U_{ii} = -2t$ in a finite size (21x21) lattice at half filling. The impurity is deposited at the centre of the lattice ($x = 11$, $y = 11$). Here we present results

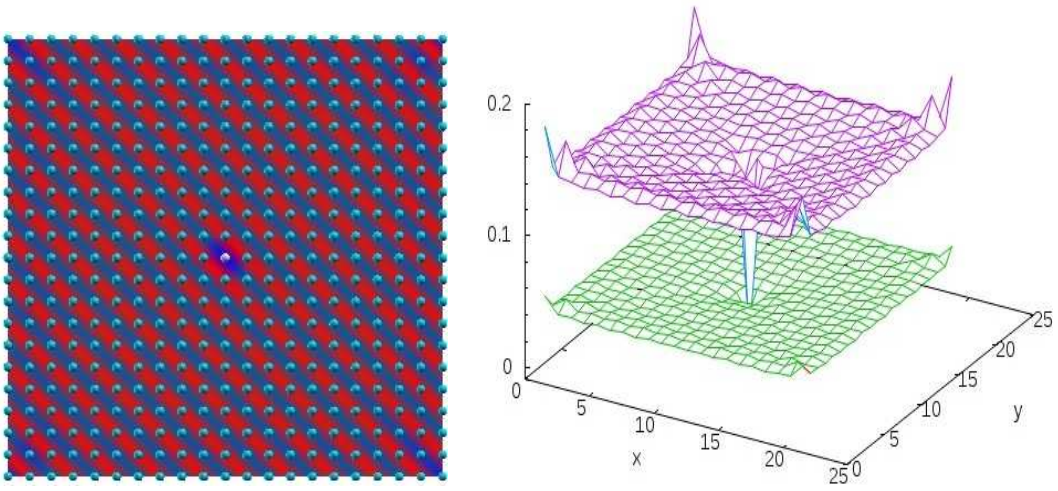

Figure 4.4: (a) Electron density for a 21x21 s-wave superconductor at half filling. The on-site coupling strength is $U_{ii} = -2t$. In the presence of an impurity the degeneracy of the pure case is removed and the CDW becomes the favoured ground-state. (b) S-Wave order parameter for the system described in (a). The upper (purple) plot is the order parameter for $\epsilon_{11,11} = -10.0t$, while the lower (green) plot is for $\epsilon_{11,11} = -0.5t$.

for an attractive impurity potential. Two cases for weak impurity scattering ($\epsilon_{11,11} = -0.5t$) and strong impurity scattering ($\epsilon_{11,11} = -10t$) are presented. The electron density and order parameter are shown in Figures 4.4 (a) and (b), respectively. As demonstrated in the last section, in a pure s-wave system with open boundaries there are three degenerate ground-states: the superconducting state with uniform density (SC), a CDW state with no superconductivity (CDW), as well as the state in which CDW and SC coexist (CDW+SC). When an impurity is deposited into the system, the degeneracy is lifted and the CDW state becomes the preferred ground-state. This is because the impurity pins the phase of the density wave to its site, making the modulations more favoured as shown in Figure 4.4 (a).

When the strength of the impurity is changed, some counter-intuitive results are obtained. One would think that with strong impurity scattering superconductivity should be suppressed more than with weak impurity scattering. As Figure 4.4 (b) indicates, however, that in fact the opposite happens. The average value of the order parameter for the weak ($\epsilon_{11,11} = -0.5t$) impurity is suppressed by a considerable amount compared to the strong ($\epsilon_{11,11} = -10.0t$) impurity. After some thought, the reason why this should occur becomes clear. For a strong impurity (attractive) potential, electrons become localized around the impurity site and they do not have enough kinetic energy to hop to neighbouring sites.

Moreover, the scattering length of a strong impurity can be rather short, possibly on the scale of few atomic sites. The net effect of such a strong impurity is to effectively remove that site from the lattice, and the remaining electrons are barely affected by the impurity. For a weak impurity, however, an energy gain by sitting at the impurity site can be minor and electrons are fairly mobile around the impurity. Still, the electrons are scattered by the impurity (though weakly) and many can be affected by the relatively long scattering length of the weak impurity. If the scattering length is comparable or even larger than the coherence length, i.e., roughly the size of a Cooper pair, then this pair breaking effect of an attractive impurity potential can be substantial. Therefore, in a nanoscale superconductor in which the Cooper-pair wavefunction can extend over the bulk of the sample, SC can be suppressed significantly by a *single*, weak impurity, whose scattering length is comparable to the sample size. Since s-wave SC is robust against the presence of surfaces, we can conclude that this is mainly an effect of the impurity by itself.

4.4 D-Wave SC with Single Impurity

Impurities deposited onto a finite-size d-wave superconductor have profoundly different effects than for the s-wave case. In addition to pair breaking at the boundaries, there is now pair breaking occurring at the impurity site. We demonstrate the effects of an impurity in a d-wave superconductor of a finite size (21x21) lattice at half filling with an impurity deposited at the centre of the lattice with $\epsilon_{11,11} = -0.5t$. To illustrate the effects of varying the electron-phonon coupling strength for a fixed impurity potential strength, we present the electron density distribution for $U_{ij} = -1.5t$ and $U_{ij} = -2.7t$ in Figures 4.5 (a) and (b), respectively. The pair breaking due to the surface tends to push electrons away from the boundary, and as can be seen in these figures the attractive impurity potential tends to localize the electrons around its site. For stronger electron-phonon coupling this effect is amplified, as the electrons can gain more energy by being further away from the boundary. For $U_{ij} = -2.7t$, there is a large region of localized electrons around the impurity, while the density along the boundary is mostly suppressed.

The order parameter for $U_{ij} = -1.5t$ and $U_{ij} = -2.7t$ are shown in Figures 4.5 (a) and

(b), respectively. As one would expect, the d-wave order parameter is suppressed around the region of the impurity as well as along the boundaries, as these both cause pair breaking processes. Increasing the electron-phonon coupling strength, however, leads to somewhat surprising results. One would think that by increasing the pairing interaction the superconductor would be more robust against the presence of impurities due to its short coherence length. As Figure 4.6 (b) shows, however, increasing the coupling strength leads to much *stronger* suppression of the order parameter, in a much larger region. A *weakly attractive* potential kills SC with *strong* electron-phonon interaction! In the example for $U_{ij} = -2.7t$ shown above, the pair-breaking effects due to the surface and single impurity combined have led to SC being completely destroyed in a major area of the sample, and what we are left with is a narrow "ring" close to the boundary where SC remains more or less intact. This is a very intriguing analogy to the so-called surface superconductivity seen in type-III materials in a magnetic field, where SC is suppressed except in a thin layer near the surface.

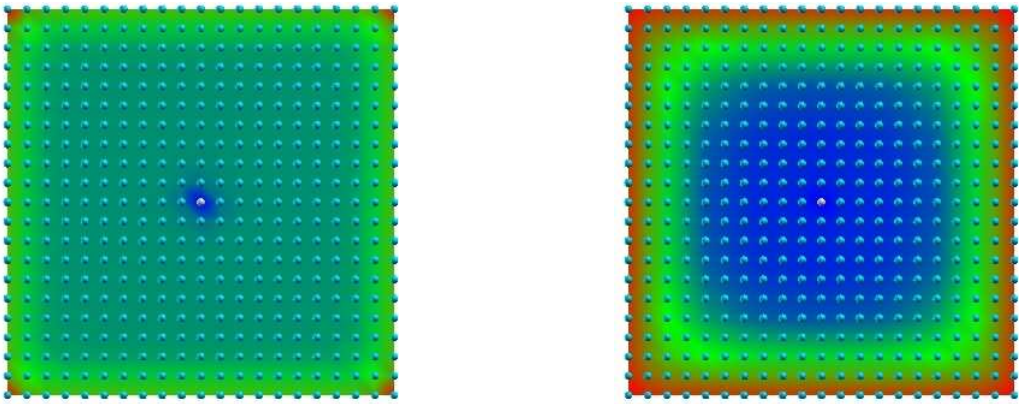

Figure 4.5: Electron density for a 21x21 d-wave superconductor at half filling with impurity $\epsilon_{11,11} = -0.5t$. (a) $U_{ij} = -1.5t$. For weak electron-phonon coupling, the charge density becomes localized around the impurity site and slightly suppressed at the boundary. (b) $U_{ij} = -2.7t$. For strong coupling the effect in (a) becomes amplified, as electrons can gain more energy by moving away from the surface. In this example the electron density is completely suppressed at the boundary.

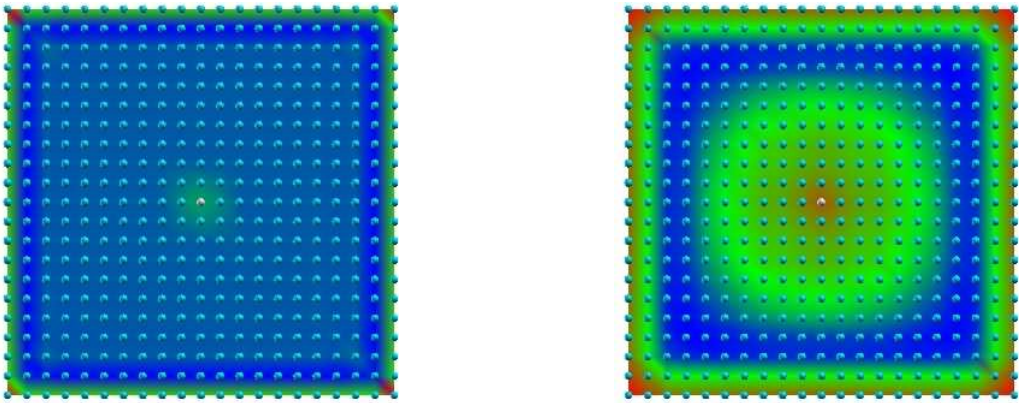

Figure 4.6: D-wave order parameter for the system described in Figure 4.5. (a) $U_{ij} = -1.5t$. The order parameter is suppressed at the location of the impurity as well as along the boundary. (b) $U_{ij} = -2.7t$. In the strong coupling case the order parameter is completely suppressed at the impurity site, leaving a narrow region of "surface superconductivity".

Chapter 5

Charge Density Modulations and Superconductivity

In this chapter the results regarding the nature of the interplay between CDW and SC in the context of the BdG equations is examined. The purpose of this research is to understand the relationship between the superconducting and CDW states in our model. We begin by studying a periodic system without impurities and examining the coexistence of the CDW and SC states. In order to identify the mechanism for the density wave instability we examine the topology of the Fermi surface and how it affects the interplay between the SC and CDW states. It is hoped that the results in this chapter can provide a theoretical basis for interpreting the results seen in experiments such as those described in Chapter 1.

5.1 Coexistence of CDW and Superconductivity

In addition to the charge density modulations found in finite size systems as described in Chapter 4, density modulations have also been found for systems with periodic boundary conditions (PBC) without impurities. It has also been found that with on-site s-wave interactions both the CDW state and superconducting state coexist at half filling. As a typical example we present (below) the main results for an 18x18 cell at half filling using PBC and on-site s-wave coupling strength $U_{ii} = -2.50t$. There are *three* degenerate ground-states for this system: the superconducting state with uniform density (SC), a CDW state with no superconductivity (CDW), as well as the state in which CDW and SC coexist (CDW+SC). Each of these three states have identical ground-state energy and transition temperature. The following sections detail how each of the three states are achieved.

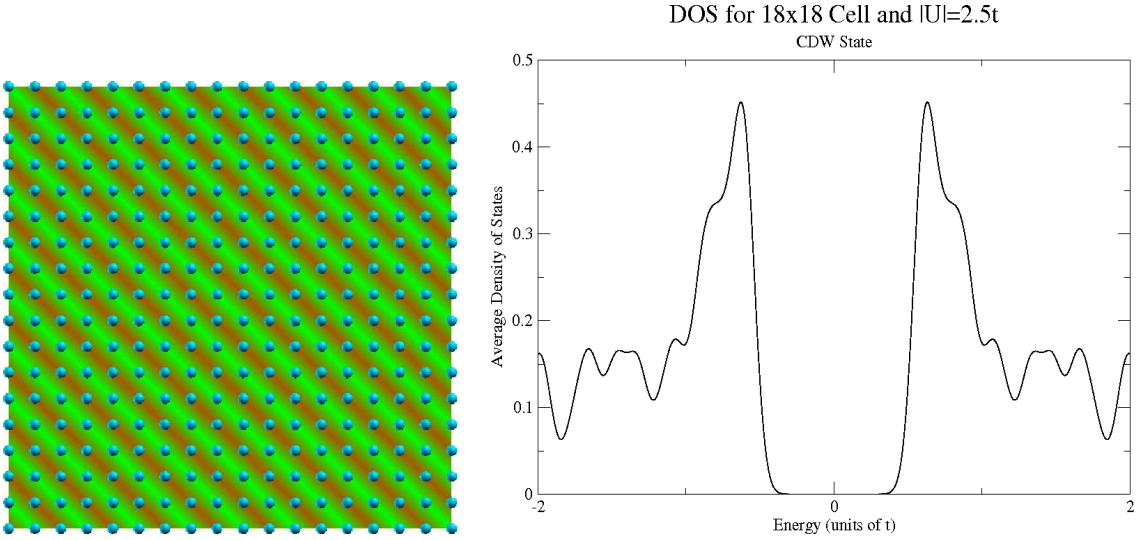

Figure 5.1: (a) Charge density distribution for the 18x18 cell lattice with $|U_{ii}| = 2.50t$. The colour scheme is such that regions of low density correspond to red, while high density correspond to green. (b) The total density of states for the pure CDW state, clearly exhibiting an energy gap.

5.1.1 Density Wave State

The pure density wave state is achieved by setting the anomalous SC coupling terms in the BdG equations to be zero. More precisely, the off-diagonal components of the BdG equations are zero:

$$\begin{pmatrix} \hat{H} & 0 \\ 0 & -\hat{H} \end{pmatrix} \begin{pmatrix} u_n \\ v_n \end{pmatrix} = \epsilon_n \begin{pmatrix} u_n \\ v_n \end{pmatrix} . \tag{5.1}$$

Thus, the particle and hole amplitudes u_n and v_n are decoupled. Since superconductivity is "off", the sole effect of the on-site s-wave attraction U_{ii} is to cause electron correlations via the Hartree potential (Eq. (3.6)). As already mentioned in Section 4.1, this term is crucial to obtaining density modulations. If this term were simply neglected (as is typically the case) no CDW would result and one would have a uniform density distribution with a larger ground-state energy. The electron density for our 18x18 cell with PBC is shown in Figure 5.1(a) and clearly shows regular CDW density modulations. The ground-state energy of this state is $E_0^{CDW} = -990.40t$ and has a critical temperature of $T_c^{CDW} = 0.33t$. The ground-state energy of the normal state (i.e., no CDW) with the uniform density at half filling is $E_0 = -522.61t$. The site-averaged density of states (DOS) is shown in Figure 5.1(b).

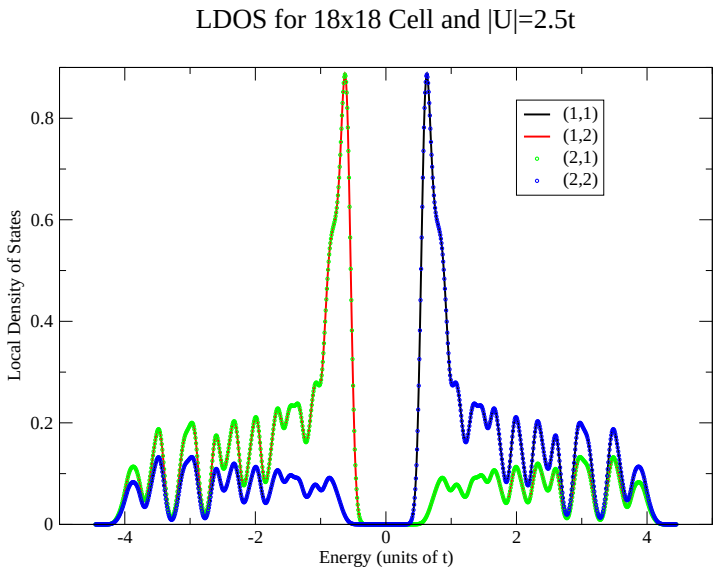

Figure 5.2: LDOS for the 18x18 cell lattice with $|U_{ii}| = 2.50t$. Sites (1,1) and (2,2) have density less than one, while sites (1,2) and (2,1) have density greater than one. The alternating charge density seen in Figure 5.1(a) results in a spatially alternating local density of states.

This DOS shows a gap opening at the Fermi level that signifies the stability of the CDW state and the required energy to add or remove an electron to destroy the perfect periodic charge modulations. The energy gap is well-defined and the DOS appears to be particle-hole symmetric; however it is not so for the local density of states, which alternates from site to site following the charge alteration. The LDOS at sites $(x, y) = (1, 1), (1, 2), (2, 1), (2, 2)$ are shown in Figure 5.2. Sites $(1, 1)$ and $(2, 2)$ correspond to regions with an average density less than one, and sites $(1, 2)$ and $(2, 1)$ have an average density greater than one. Figure 5.2 shows that the sites with the electron density greater than one have a large number of states available for hole excitation, while sites with an average electron density less than one have a large number of states available for particle excitation. When the site-averaged density of states is calculated the peaks appear to be symmetric as in Figure 5.1(b). The CDW energy gap will be discussed in much greater detail in Section 5.4

5.1.2 Superconducting State

By including the off-diagonal components of the BdG equations the particle and hole amplitudes u_n and v_n are coupled via the order parameter given by Eq (3.9), and the result is a superconducting state. When the BdG equations are solved selfconsistently, the solutions converge to a superconducting state with an s-wave order parameter of $\Delta_s = 0.601t$. This state turns out to be a homogeneous solution, with a constant order parameter ($\Delta_i = \Delta_s \quad \forall\, i$) and uniform charge density. The SC state has a ground-state energy of $E_0^{SC} = -990.40t$ and a critical temperature of $T_c^{SC} = 0.33t$, identical to what was found for the pure CDW state. The site averaged density of states for the SC state is shown in Figure 5.3. As can be seen in this figure this is identical to the DOS obtained for the CDW state shown in Figure 5.1(b). Thus, the superconducting and CDW ground-states are degenerate. These two stable ground states have exactly the *same* energy and critical temperature; however, they have different electron density distributions. One state has a uniform density over the entire sample (SC), while the other, as shown in Figure 5.1(a), has periodic density modulations, i.e., a CDW. Contrary to the CDW state, in the SC state the local density of sates at each site is identical to the site-averaged density of states shown in Figure 5.3. This is expected due to the uniform density and order parameter in the sample.

5.1.3 Coexistence of CDW and SC states

As shown in the previous section, both the CDW state and the SC state are degenerate. In this section it will be shown that in fact these two states can coexist together simultaneously. Since the BdG equations are selfconsistent equations, one must start from an initial approximation for the mean fields. For the pure SC state the initial approximation for the charge density was taken to be uniform. In order to mix the CDW state with the SC state, we have solved the BdG equations selfconsistently starting from the Hartree potential solution in the pure CDW state and a constant order parameter as an initial input. In this way we have been able to let the solutions converge to a mixed CDW and SC state. The ground-state energy of this mixed state is $E_0^{CDW+SC} = -990.40t$ and the critical temperature is $T_C^{CDW+SC} = 0.33t$. That is, the mixed state also has the same ground-state energy

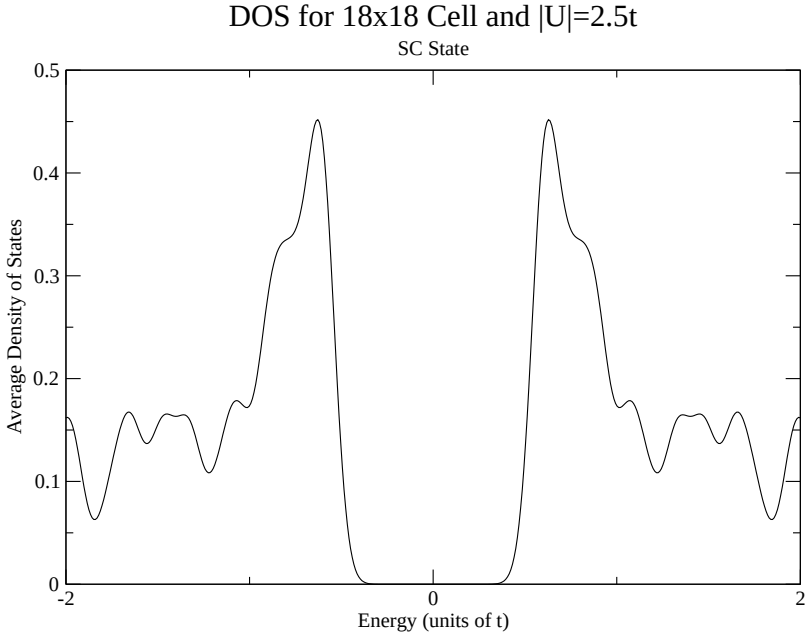

Figure 5.3: Site-averaged density of states for a 18x18 cell and $|U_{ii}| = 2.50t$ in the SC state. Contrary to the CDW state the LDOS is identical at all sites in the sample and therefore equivalent to the total DOS. The total DOS in the SC state is identical to the DOS shown in Figure 5.1(b) for the CDW state.

and critical temperature as the pure SC and CDW states. A summary of the s-wave order parameter and CDW amplitudes for these three states is presented in Table 5.1. As the table shows, in order for CDW and SC to coexist, both the order parameter and amplitude of the CDW are suppressed relative to when the states are separate. A plot of the CDW amplitude and s-wave order parameter as a function of temperature for the mixed state is shown in Figure 5.4. In this plot the CDW amplitude and order parameter are taken with respect to their respective pure-state value at zero temperature (i.e., at $T = 0$ the order parameter and the CDW amplitude in the mixed state (SC+CDW) are reduced to 78% and 62% their value in their respective pure states). The plot shows that both superconductivity and CDW disappear at the same critical temperature. At this point, why density waves occur at all is not obvious. The normal state of this system is homogeneous (i.e., no surface boundaries nor impurities). Therefore, the pure CDW and SC+CDW states must be a result of electronic instability.

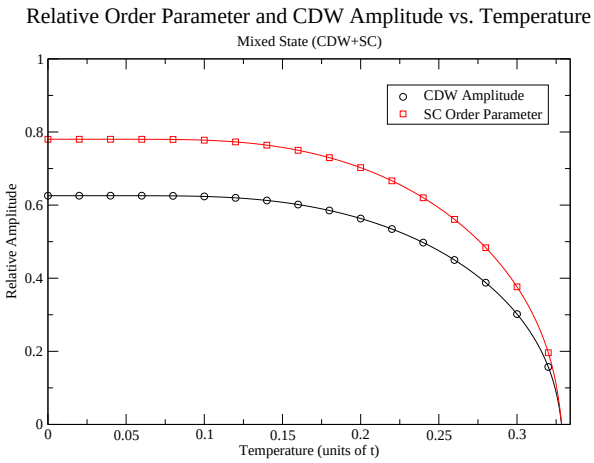

Figure 5.4: Relative CDW amplitude and SC order parameter as a function of temperature in the CDW+SC mixed state. Both SC and CDW disappear at the same temperature.

State	Δ_0 (units of t)	CDW Amplitude
SC	0.60154	0.00000
CDW	0.00000	0.48123
Mixed	0.46925	0.30110

Table 5.1: Results of the zero-temperature CDW amplitude and SC order parameter for the three degenerate states. All states have $E_0 = -990.40t$ and $T_C = 0.33t$. In the mixed state (CDW+SC) the amplitude of the CDW modulations and the SC order parameter are reduced to $\sim 62\%$ and $\sim 78\%$ their value in their respective pure states.

5.2 Mechanism for CDW in the Tight-Binding Model

We have determined that the CDW found in the previous section must be a result of an electronic instability of the normal state. In order to identify the mechanism of this instability we need to study the topology of the Fermi surface in our model. For the tight-binding model with hopping among nearest neighbours, the Fermi surface is a square at half filling as shown in Figure 5.5 and perfect nesting is occurs on the entire Fermi surface. In addition, we must also identify the position of the saddle point singularities, which are the relevant parameters for the vHs mechanism. As already mentioned in Section 2.2 it has been shown by Rice and

Scott [1] that any vector in momentum space which connects two saddle point singularities can also lead to a divergence in the dielectric response,

$$\epsilon(\vec{q},\omega) = 1 - \lim_{\alpha\to 0} \frac{e^2}{V_g \epsilon_0 q^2} \sum_{\vec{k}} \frac{f_o(\vec{k}+\vec{q}) - f_o(\vec{k})}{E(\vec{k}+\vec{q}) - E(\vec{k}) - \hbar\omega - i\hbar\alpha} \ , \tag{5.2}$$

where $f_0(\vec{k})$ is the Fermi-Dirac distribution function for energy $E(\vec{k})$. The divergence of the response indicates that the electron gas is unstable towards CDW formation, and in addition to nesting, any vector $\vec{Q_{sp}}$ which connects two saddle points will also result in a logarithmic divergence. To find the position of these saddle points we must study the normal-state dispersion relation. For the Hamiltonian in Equation (3.2) in the normal state (i.e., $|U| = 0$) the energy-momentum dispersion relation can be found analytically as

$$E(\vec{k}) = -2t\left(\cos(k_x a) + \cos(k_y a)\right) \ , \tag{5.3}$$

where a is the lattice spacing and the periodic boundary conditions make k_x and k_y are integer multiples of $2\pi/Na$:

$$k_x = \frac{2\pi n_x}{Na} \quad \text{and} \quad k_y = \frac{2\pi n_y}{Na} \ ,$$

where n_x and n_y are integers. We take the Brillouin zone to be $-N/2 \le n_x, n_y \le N/2$ for a system of N lattice sites. By taking the derivative of the dispersion relation with respect to momenta one can find the locations of the critical points,

$$\nabla_{\vec{k}} E(\vec{k}) = 0 \ .$$

The location of the critical points are then determined by the equations,

$$\partial_{k_x} E(\vec{k}) = 2ta\sin(k_x a) = 0 \ ,$$
$$\partial_{k_y} E(\vec{k}) = 2ta\sin(k_y a) = 0 \ ,$$

which give for the critical points $k'_x = m\pi/a$ and $k'_y = n\pi/a$, where m and n are integers. In the first Brillouin zone this corresponds to the 9 points:

$$(k'_x, k'_y) = \begin{cases} (0,0) \ , \\ \frac{\pi}{a}(\pm 1, 0) \ , \\ \frac{\pi}{a}(0, \pm 1,) \ , \\ \frac{\pi}{a}(\pm 1, \pm 1) \ . \end{cases} \tag{5.4}$$

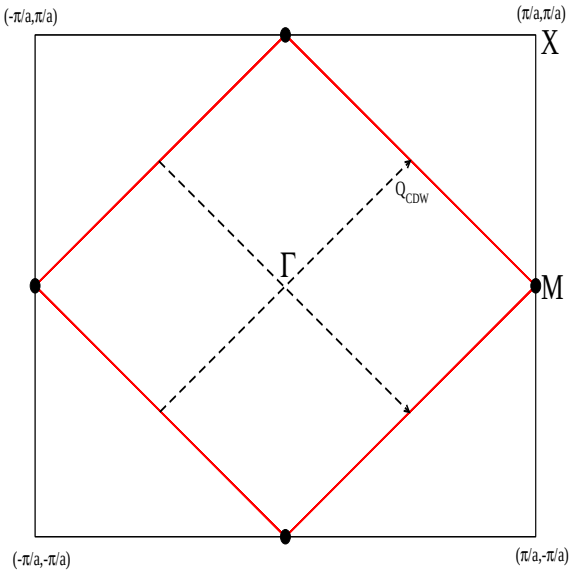

Figure 5.5: The Fermi surface for the 2D square lattice of the tight-binding Hamiltonian at half filling. Nesting vectors connecting the sides of the square Fermi surface are shown as black dashed lines and the positions of the saddle points are marked with black circles. The vectors that connect the saddle points are identical to the nesting vectors.

In order to determine if these points are saddle points we shall examine the second partial derivatives. The points are saddle points if $M(k'_x, k'_y) < 0$, where

$$M(k_x, k_y) = \begin{vmatrix} \partial_{k_x,k_x} E(\vec{k}) & \partial_{k_x,k_y} E(\vec{k}) \\ \partial_{k_y,k_x} E(\vec{k}) & \partial_{k_y,k_y} E(\vec{k}) \end{vmatrix} \tag{5.5}$$

is the 2×2 Hessian matrix. Substituting the critical points into Equation (5.5) one finds that the only points which give $M(k_x, k_y) < 0$ are

$$(k'_x, k'_y) = \begin{cases} \frac{\pi}{a}(\pm 1, 0) \\ \frac{\pi}{a}(0, \pm 1) \end{cases} \tag{5.6}$$

The location of the saddle points in Equation (5.6) correspond precisely to the midpoints of the line $X - M - X$ and are illustrated as black circles in Figure 5.5. As a result the vector which connect the saddle points and the nesting vector connecting parallel parts of the Fermi surface are the same ($\vec{Q}_{CDW} = \vec{Q}_{SP} = (\pm\pi/a, \pm\pi/a)$, with magnitude $\sqrt{2}\pi/a$). Since these vectors correspond to the wavevectors of the charge density modulation this result is

consistent with the densities shown in Figure 5.1(a), as the modulation occurs along the ΓX direction with wavelength

$$\lambda_{CDW} = \frac{2\pi}{Q_{CDW}} = \sqrt{2}a \ .$$

5.3 CDW state with varying Fermi Surface

The results of the previous section have shown that the density modulations in Figure 5.1(a) are consistent with an instability of the Fermi surface. Since $\vec{Q}_{SP}$ and $\vec{Q}_{CDW}$ are identical, however, there is no way to determine whether the density modulations are a result of nesting and/or the van Hove singularity mechanism identified by Rice and Scott [1]. In order to study the effects of the vHs on the CDW we extend our tight-binding model to include hopping among next-nearest neighbours as well. By doing so we arrive at a much richer Fermi surface and it enables us to study the effects of the Fermi surface topology on the CDW states. By modifying the hopping parameter, the Hamiltonian now has the form:

$$H_0 = \sum_{\langle ij \rangle \sigma} t_{ij} c^{\dagger}_{i\sigma} c_{j\sigma} + \sum_{i\sigma} (\epsilon_i - \mu)\, \hat{n}_{i\sigma} \ , \tag{5.7}$$

$$H = H_0 + \sum_i U_{ii} \hat{n}_{i\uparrow} \hat{n}_{i\downarrow} + \frac{1}{2} \sum_{\langle ij \rangle} \sum_{\sigma\sigma'} U_{ij} \hat{n}_{i\sigma} \hat{n}_{j\sigma'} \ . \tag{5.8}$$

where

$$t_{ij} = \begin{cases} -t & \text{if } i \text{ and } j \text{ are nearest neighbours,} \\ t' & \text{if } i \text{ and } j \text{ are next nearest neighbours,} \\ 0 & \text{otherwise,} \end{cases} \tag{5.9}$$

and we restrict the next-nearest neighbour hopping to $|t'| < 0.5t$. Results for $|t'| > 0.5$ would be unrealistic as the next-nearest neighbour element becomes comparable to the nearest-neighbour hopping. In addition we only perform calculations for $t' > 0$, as $t' < 0$ is equivalent to $t' > 0$ with $E(k)$ interchanged with $-E(k)$. This is illustrated in Figure 5.6 which shows the energy dispersion relation plotted in a repeated zone scheme for positive and negative values of t'. The Fermi surface is illustrated by the contours at the base. This figure indicates that the Fermi surface for negative t' is equivalent to that of positive t'; however surfaces are shifted in the first BZ by $\vec{k} = (\pm\pi/a, \pm\pi/a)$ and have become hole-like. As

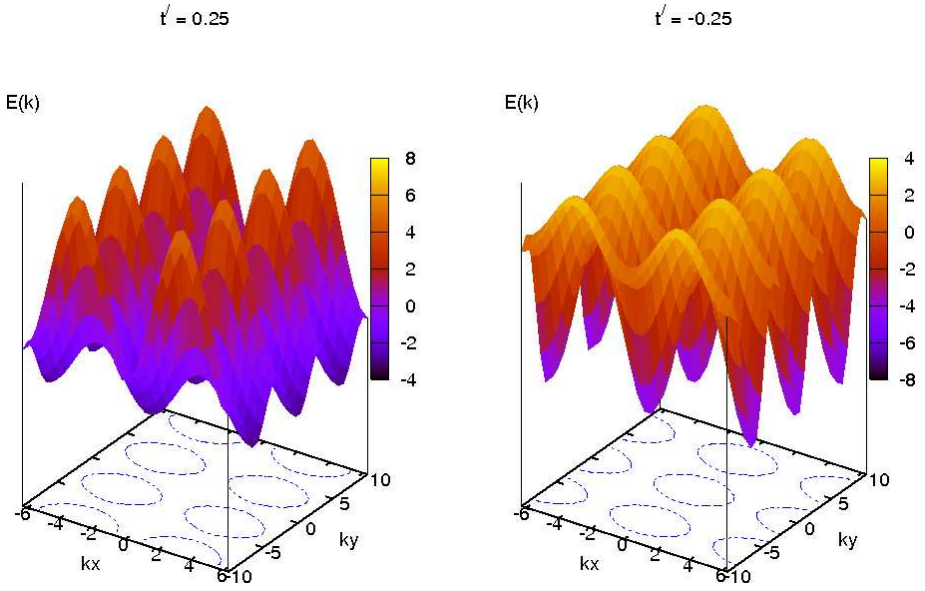

Figure 5.6: Energy-momentum disperion relation for positive and negative values of t'. The contours at the base identify the Fermi surfaces. In addition to a phase shift of $\vec{k} = (\pm\pi/a, \pm\pi/a)$, surfaces for $t' = 0.25$ are electron-like, while for $t' = -0.25$ are hole-like. When $t' \to -t'$ then $E(\vec{k}) \to -E(\vec{k})$.

shown in Appendix D, at half filling the chemical potential for negative t' increases as t' increases, keeping the density of states equivalent for both signs of t', the only difference in the DOS being $E(k)$ changed to $-E(k)$. The sole result of changing $t' \to -t'$ is to change $E(k) \to -E(k)$ and therefore it suffices to study the case for $t' > 0$ only. When next-nearest neighbour hopping is included into the Hamiltonian the normal-state dispersion relation becomes

$$E(\vec{k}) = -2t\left(\cos(k_x a) + \cos(k_y a)\right) + 4t'\left(\cos(k_x a)\cos(k_y a)\right) \ . \tag{5.10}$$

With nearest-neighbour hopping only, the properties of the ground-state are dominated by nesting of the Fermi surface as well as the vHs present at the Fermi energy. By including hopping between next-nearest neighbours we can remove the perfect nesting in Figure 5.5. The vHs is always present, however, due to the particular topology of the Fermi surface. Using the critical point test shown in the previous section it can be shown that the positions of the saddle points do not change as a function of t'; however as the chemical potential

changes, the vHs is moved off the Fermi surface. This can also been seen in Figure 5.7 which shows surface plots of the dispersion relation $E(\vec{k})$ at several values of t'.

Using the position of the saddle points in the dispersion relation one finds that the location of the saddle points in the DOS are given by

$$E_{vHs} = -4t' - \mu \ . \tag{5.11}$$

The five remaining points in Equation (5.4) correspond to maxima and minima in the dispersion relation and allow us to identify the top and bottom of the band. The bottom of the band occurs at $(k'_x, k'_y) = (0, 0)$ while the top of the band is located at points $(k'_x, k'_y) = (\pi/a)(\pm 1, \pm 1)$. Using these points one finds that

$$E_{min} = -4t + 4t' - \mu \ , \tag{5.12}$$

$$E_{max} = +4t + 4t' - \mu \ . \tag{5.13}$$

The bandwidth in our model is $8t$ and independent of t'; however, the entire band begins to shift upward as t' increases. As a result, the width of the negative states decreases, while the width of positive energy states increases. This can clearly be seen in Figure 5.8 which shows the band structure for various values of t' in the normal state (i.e. $|U| = 0$). This figure shows that the van Hove singularity remains below the Fermi level as t' increases, while the entire band shifts upwards towards positive energy. In addition, the band begins to flatten in the region near the vHs, which results in a very large density of states at this energy. The density of states shown in Figure 5.10(a) verifies this, as the vHs clearly moves towards negative energy and its divergence grows with increasing t'.

This density of states in Figure 5.10(a) is the result if one solves the usual Hartree equations with $|U| = 0$. However, if one solves the BdG equations in the normal state one obtains the DOS as shown in Figure 5.10(b) which has additional states below the bottom of the band. Looking at this figure alone one might incorrectly conclude that the bandwidth becomes larger with increasing t'; however, this is not the case as these additional state are "artificial" and are a result of the particle-hole symmetry of the BdG equations. When solving the BdG equations for the normal state using Equation (5.1) we are effectively solving the Hartree equations twice; the solutions of which having both positive (electron)

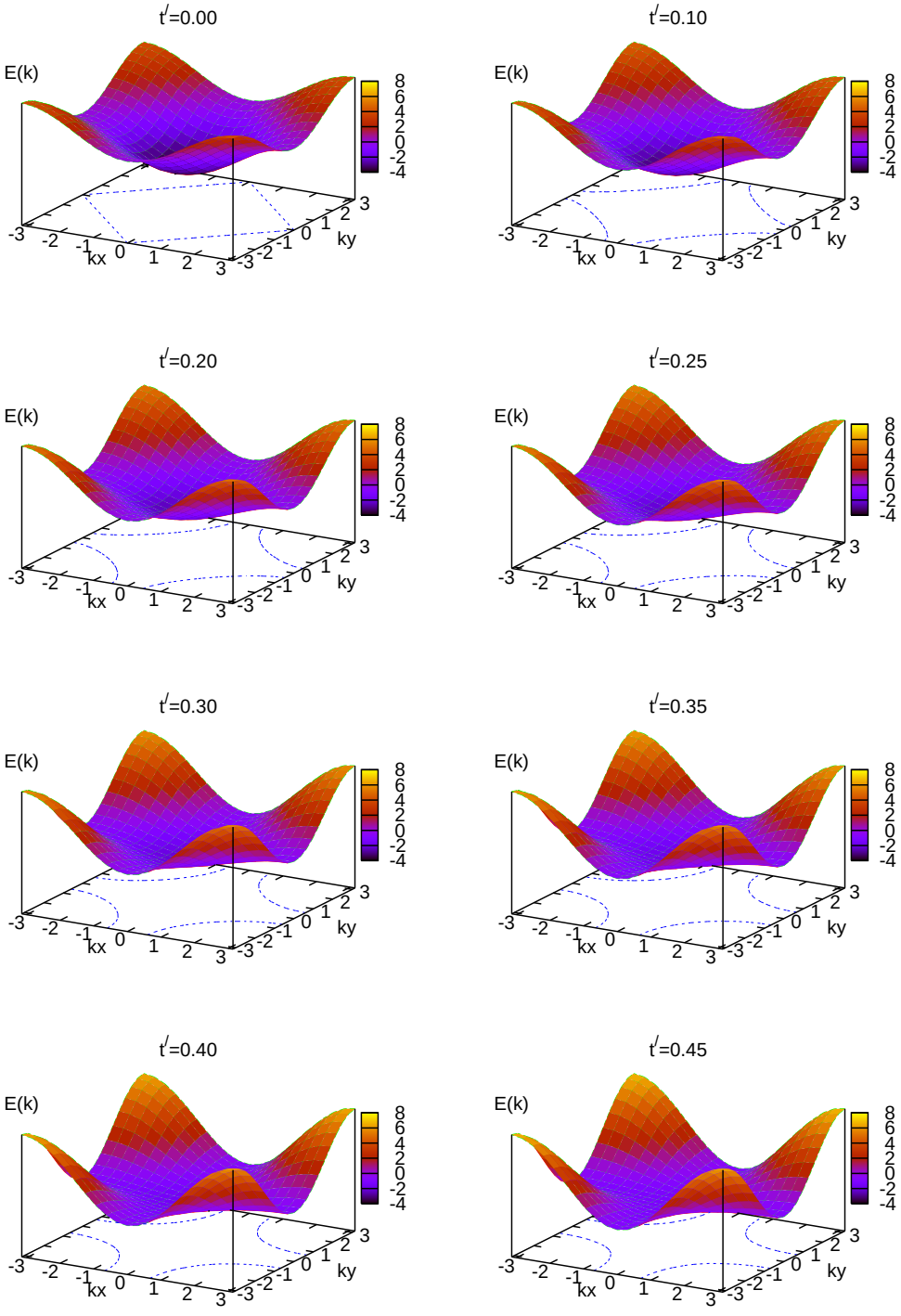

Figure 5.7: Energy-momentum dispersion relation for various values of hopping parameter t'. The contours at the base identify the Fermi surfaces. As t' is increased the top and bottom of the band rises, while the saddle points move lower in energy. As a result the saddle points are moved off the Fermi surface.

and negative (hole) energies. As an example, suppose for large t' the normal-state bandwidth ranges from $-2t \leq \epsilon \leq 6t$. The positive energy solutions will have the same bandwidth. The negative energy solutions, however, will have a bandwidth in the range $-6t \leq \epsilon \leq 2t$ making the combined bandwidth appear to be $-6t \leq \epsilon \leq 6t$. Since the true physical states are those from the positive energy solutions, the states for $-6t \leq \epsilon \leq -2t$ are "artificial" and the density of states is zero. Thus when solving the BdG equations one must be mindful that the true states are those which belong to the normal state dispersion given by Equation (5.10), and states outside the bandwidth are an artificial creation of the BdG equations.

Figure 5.9 shows how the Fermi surface evolves with varying t'. The shape of the Fermi surface is a strong function of the next-nearest neighbour hopping parameter t'. When t' becomes nonzero, the square seen in Figure 5.5 is destroyed and the Fermi surface begins to exhibit curvature. Parallel portions (although small) do seem to exist for $t' < 0.2$, however, quickly disappear as the curvature increases for larger t'. This implies that nesting of the Fermi surface should become weaker with increasing t' and eventually disappear completely. Therefore by choosing an appropriate value of t' it should be possible to determine which mechanism, nesting or the van Hove singularity, is responsible for generating density waves in our model.

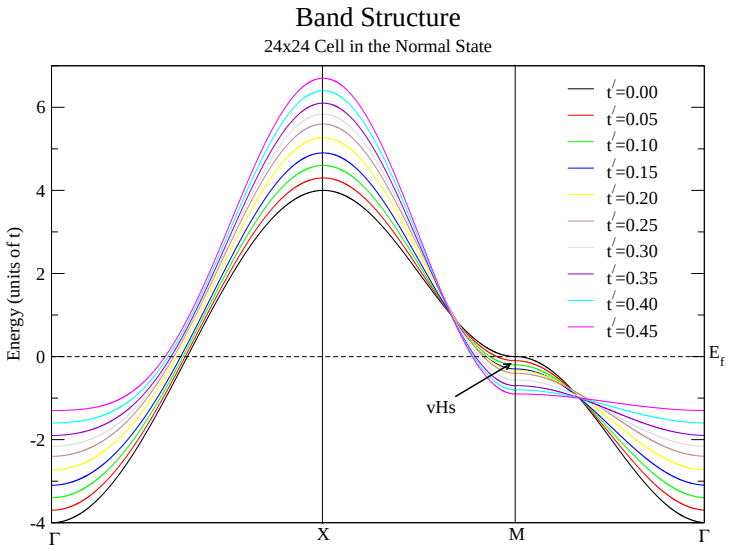

Figure 5.8: Band structure for a 24x24 cell in the normal state. As t' increases the top and bottom of the band move toward positive energy, while the total bandwidth remains $8t$. The band also begins to flatten near the vHs, indicating a large density of states at this energy.

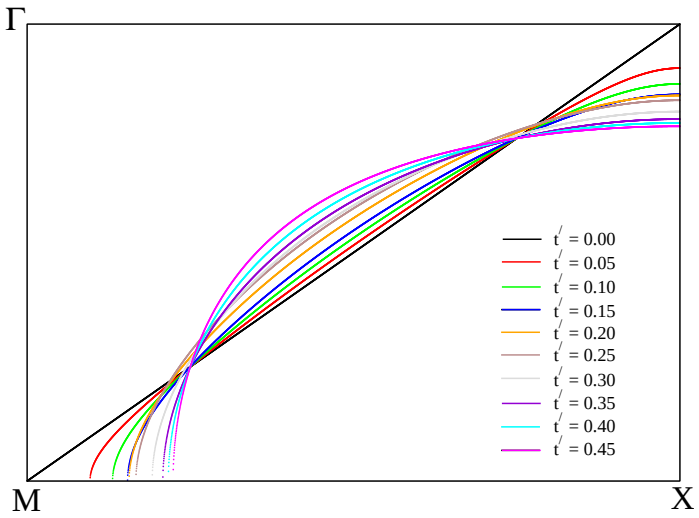

Figure 5.9: Calculated Fermi surface for a 24x24 cell at various values of hopping parameter t'. The plot only spans one quarter of the first BZ, and the full Fermi surface can be found by symmetrizing to the other three quadrants. When $t' \neq 0$ perfect nesting disappears.

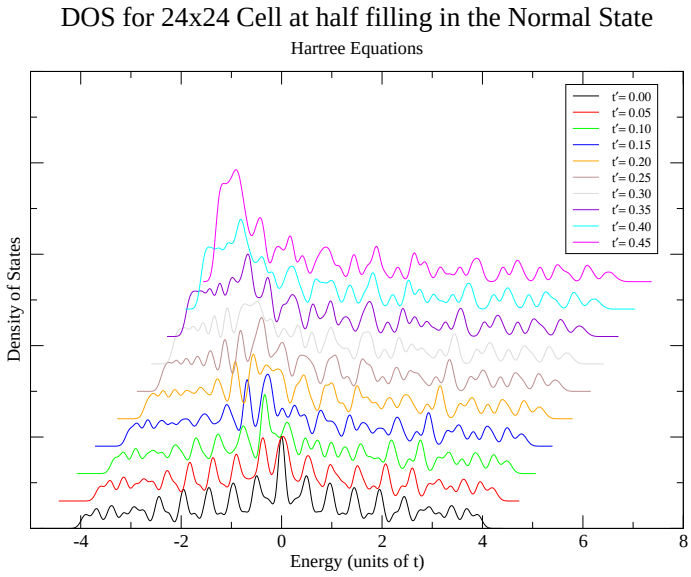

(a) Normal State DOS Solved with Hartree Equations

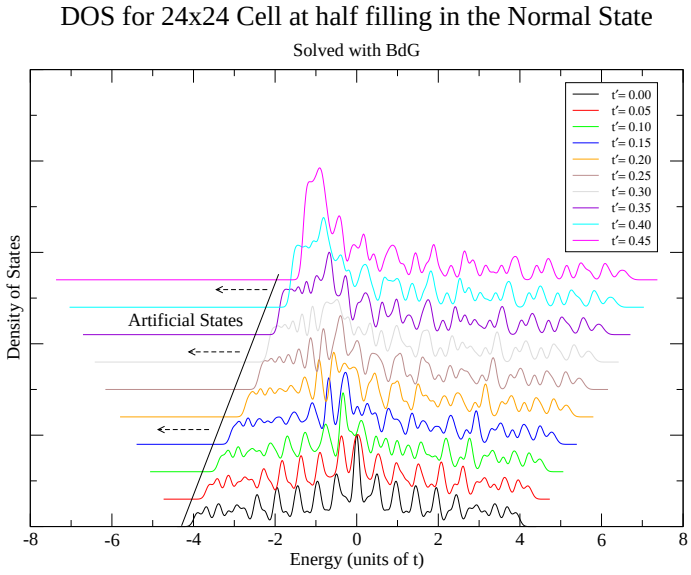

(b) Normal State DOS Solved with BdG Equations

Figure 5.10: (a) Density of states for $0 \leq t' \leq 0.45$ for $|U| = 0$ on a 24x24 lattice. The results are shifted vertically for clarity. As t' increases the bandwidth remains $8t$. However, negative-energy band width decreases, while the width of positive energy states increases. In addition the saddle-point singularity shifts from $E = 0$ at $t' = 0$ towards $E = -2t$ as t' increases. (b) The same results obtained by the BdG equations, indicating the "artificial" states..

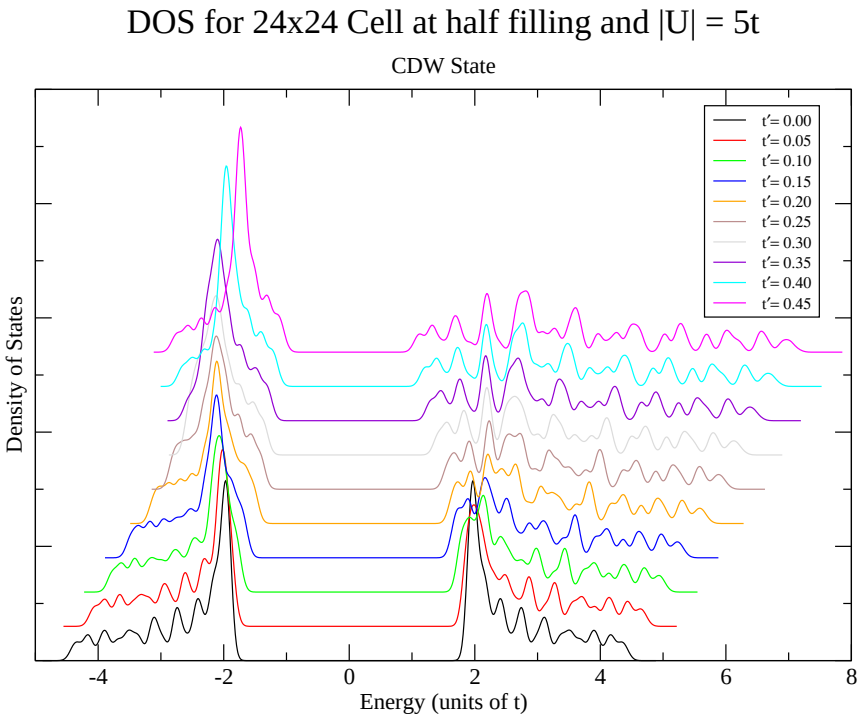

Figure 5.11: Density of states for various values of t'. The results are shifted vertically for clarity. These results were obtained for a 24x24 cell at half filling using on-site coupling $|U| = 5t$. The gap seen in the DOS is a result of the presence of a CDW. The vHs, only for the hole states for $t' \neq 0$, are strongly enhanced as t' increases and the hole bandwidth is squeezed.

5.4 Results and Discussion

In order to study the mechanism responsible for the CDW in our model and its relationship to the SC state we have studied a 24x24 periodic lattice with on-site s-wave coupling $U_{ii} = -5t$ as a function of the next-nearest neighbour hopping parameter t' for both CDW and SC states. For these calculations the Hartree and Hartree-Fock potentials were solved directly and selfconsistently. In addition, in order to ensure that the system is exactly at half filling, a second iteration loop was inserted to vary the chemical potential μ until the required average electron density has been obtained.

The CDW density of states for varying t' is shown in Figure 5.11. One can see that in contrast to the normal-state DOS in Figure 5.10(a), the CDW DOS clearly exhibits a gap

at the Fermi energy for all values of t'. When charge density modulations are present in the system, the Hartree potential $V_{ii}^{(H)}$ has the same modulations, since

$$V_{ii}^{(H)} = U_{ii} \sum_{\sigma} \left\langle \hat{c}_{i\sigma}^{\dagger} \hat{c}_{i\sigma} \right\rangle = U_{ii} \sum_{\sigma} \langle n_{i\sigma} \rangle \ . \tag{5.14}$$

Therefore, in the CDW state the Hartree potential $V_{ii}^{(H)}$ is periodic with the same periodicity as the density. The spatial variation of the Hartree potential makes it impossible to interpret $V_{ii}^{(H)}$ as a simple shift of the chemical potential, and by ignoring the Hartree potential one cannot obtain any CDW state. This is the reason why it is so imperative to include the Hartree and Hartree-Fock interactions when studying systems with inhomogeneity, as without them all of the essential physics would have been missed.

Looking at Figure 5.11 alone one might conclude that the positive-energy coherence peak disappears for $t' > 0.1$. This figure is misleading as it is the average density of states for all sites in the sample, and as was shown in Section 5.1.1 the LDOS alternates from site to site in the CDW state. The LDOS for $t' = 0.1, 0.2, 0.3, 0.4$ at several sites within the sample is shown in Figures 5.12 to 5.15. Similarly to Section 5.1.1, sites (1,1) and (2,2) have density less than one, while sites (1,2) and (2,1) have density greater than one. One can see that as t' increases and the positive-energy width widens, the positive-energy coherence peak becomes much smaller in amplitude. Near $t' = 0.3$ it becomes difficult to define coherence peaks; the energy level structure becoming clearer on either side of the gap. This behaviour is reminiscent of pseudogap behaviour in some high-T_c superconductors, where a gap in the density of states is present without coherence peaks [47]. It is plausible that when $t' > 0.25$ the vHs is the dominant mechanism for the CDW instability, and the pseudogap behaviour of the energy gap in this regime can be a manifestation of this.

It is also evident that the density of states at the van Hove singularity is also dependent on t' and becomes sharply peaked for larger t'. This is a consequence of the normal-state band structure. Recall that for $t' = 0$ the energy dispersion is symmetric and there are an equal number of particle and hole states. Since the particle and hole states for $t' = 0$ are symmetric, on average the LDOS produces the symmetric DOS seen in Figure 5.11. When t' is increased the band structure around the chemical potential is *not* symmetric, and the positive energy bandwidth is greater than the negative energy bandwidth as shown in Figure

5.10(a). The wider energy width means that the positive energy states are more spread. In addition, one can see that as the negative energy width gets smaller the van Hove singularity starts to move away from the Fermi level and at $t' \sim 0.3$ the LDOS at the vHs begins to grow significantly, even for sites with $n(i) < 1$. Since the vHs is always below the Fermi level, most of the hole excitations at sites with $n(i) > 1$ are forced to occur at the vHs. The presence of the energy gap reduces the negative energy width even further, and as a result the vHs becomes significantly enhanced as t' increases.

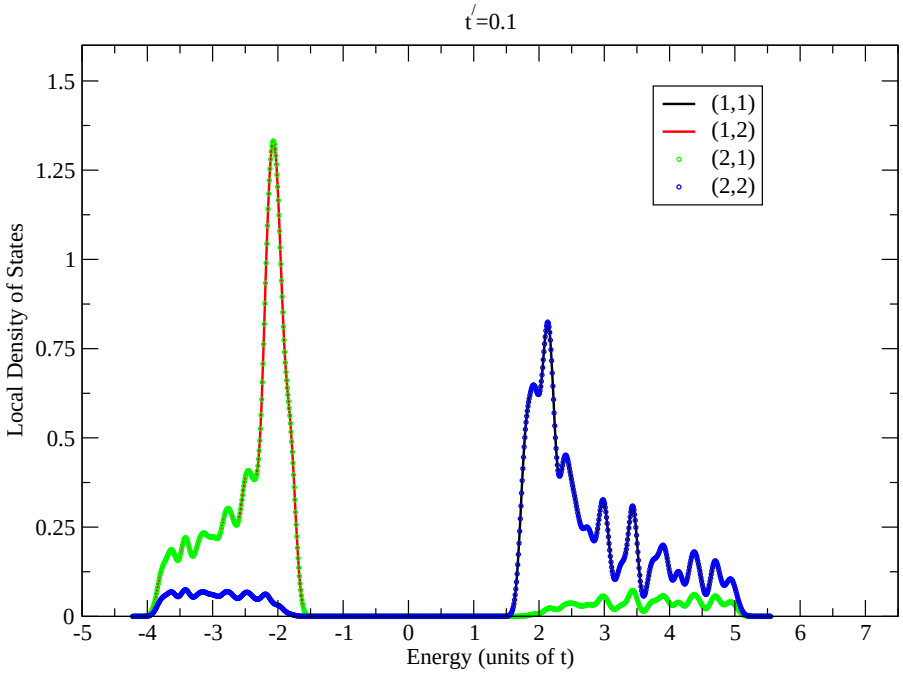

Figure 5.12: LDOS for the 24x24 cell lattice with $|U_{ii}| = 5t$ and $t' = 0.1$.

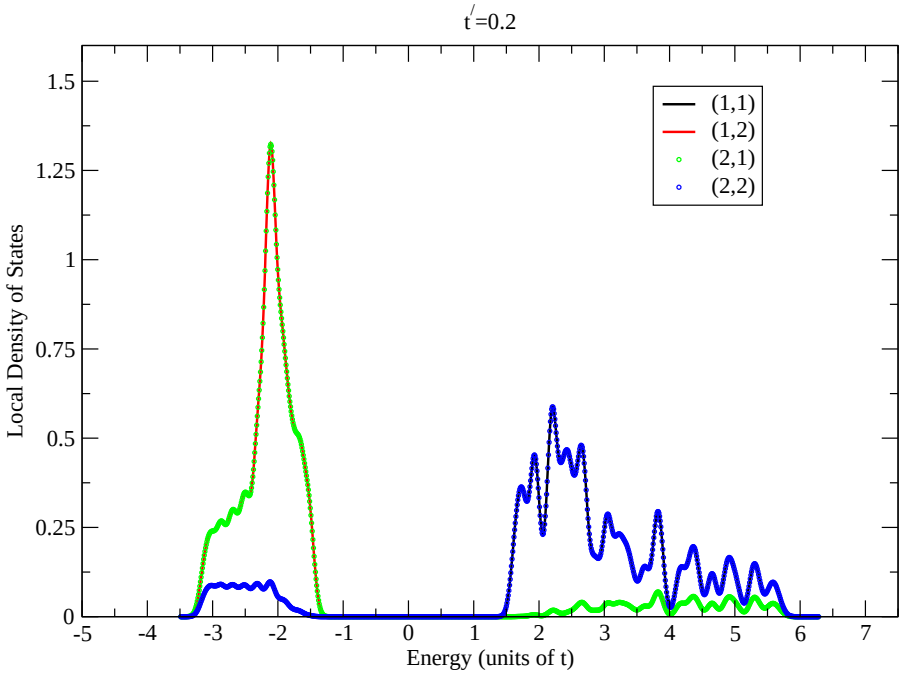

Figure 5.13: LDOS for the 24x24 cell lattice with $|U_{ii}| = 5t$ and $t' = 0.2$.

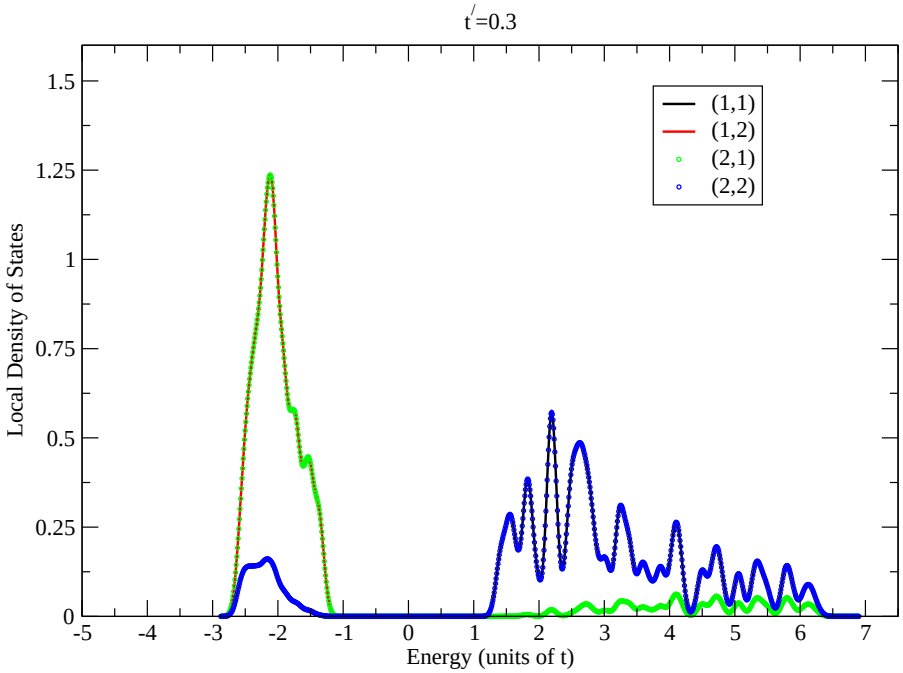

Figure 5.14: LDOS for the 24x24 cell lattice with $|U_{ii}| = 5t$ and $t' = 0.3$.

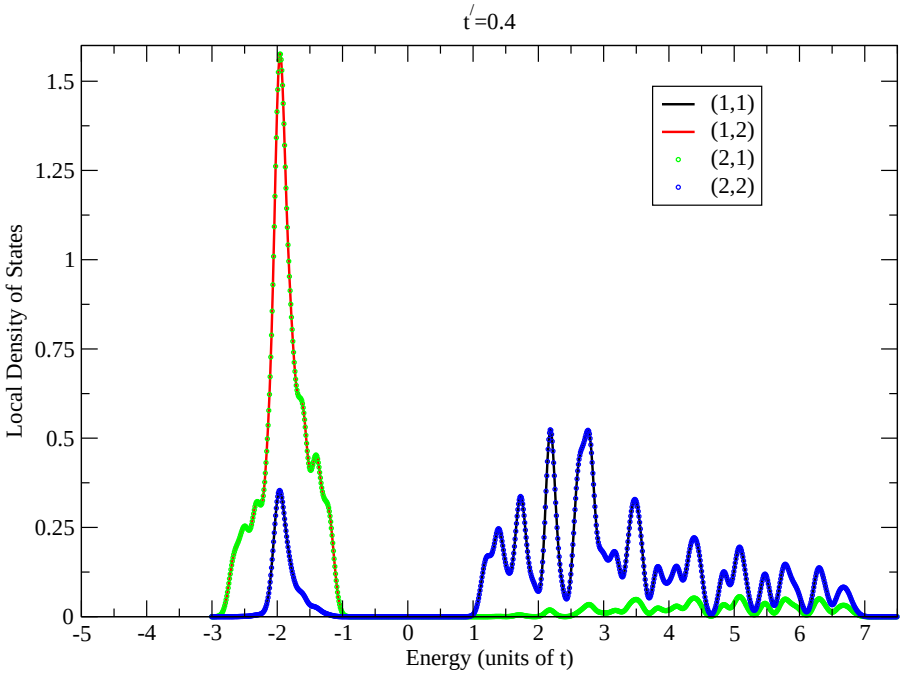

Figure 5.15: LDOS for the 24x24 cell lattice with $|U_{ii}| = 5t$ and $t' = 0.4$.

So far it has been shown that the normal state is unstable towards formation of a charge density wave, and that a gap opens up at the Fermi level. The question that needs to be answered is, what is the mechanism responsible for this instability? When $t' = 0$ perfect nesting of the square Fermi surface can lead to an instability towards CDW, but is there a scenario for which the vHs mechanism of Rice and Scott is applicable? Figure 5.9 shows that perfect nesting is destroyed as t' increases, and it has been shown that for large t' (~ 0.45) the majority of allowed hole excitations occur at the vHs. Thus, it is plausible that the vHs mechanism is responsible for the CDW at large values of next-nearest neighbour hopping.

In order to study where this transition from the nesting to vHs mechanism may occur, the t'-dependence of the CDW energy gap Δ and T_c was calculated and the results are shown in Figure 5.16. The DOS shown in Figure 5.11 indicate that the CDW gap becomes smaller as t' increases and this is verified in Figure 5.16(a). In addition to the gap, the CDW transition temperature T_c is a strong function of the next-nearest neighbour hopping and T_c is suppressed very quickly for large t'. The addition of next-nearest neighbour hopping tends to suppress CDW modulations, resulting in a lower critical temperature and a smaller gap. The ratio $2\Delta/T_c$ is shown in Figure 5.16(b) for both the CDW and SC states. As a result of T_c and the energy gap both being dependent on t', the ratio $2\Delta/T_c$ is not constant, in contrast to the SC state (see the green line in Fig. 5.16(b)). In fact the behaviour is approximately linear with a definitive slope change around $t' \sim 0.25$. Since this ratio is a measure of the electron-phonon coupling strength, this slope change may be an indication of a transition from the nesting to the vHs mechanism for the CDW instability. This interpretation is consistent with the Fermi surfaces shown in Figure 5.9, since for $t' \lesssim 0.25$ there do exist (small) parallel portions of the Fermi surface in which nesting could occur. For $t' > 0.25$, however, there is no discernible Fermi surface nesting, and nesting cannot be a dominant cause responsible for CDW.

There is additional evidence supporting the vHs mechanism present in susceptibility calculations of Equation (2.15). In the vHs scenario proposed by Rice and Scott [1] the logarithmic divergence of the susceptibility due to nesting multiplies the divergence due to the vHs. Therefore the vHs scenario will be responsible for the CDW formation as long as the nesting-driven divergence is weaker than that of the van-Hove singularity. Results for

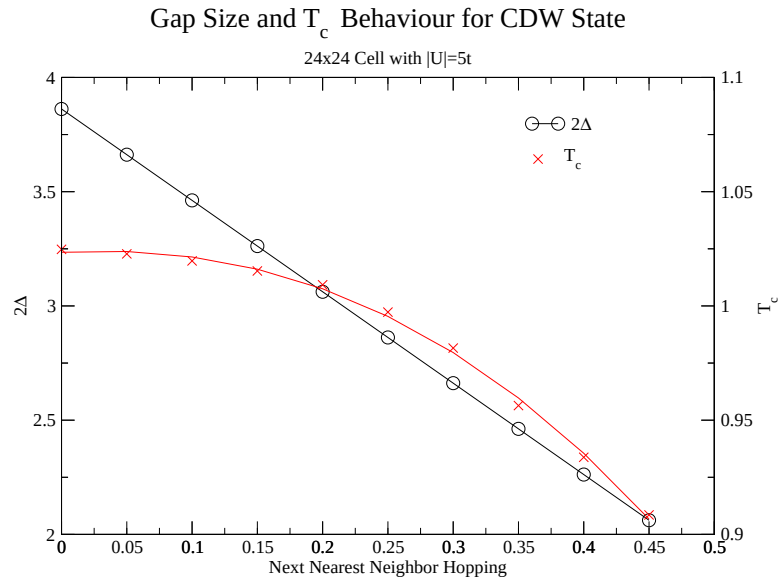

(a) Gap Size and T_c vs. t' for CDW state

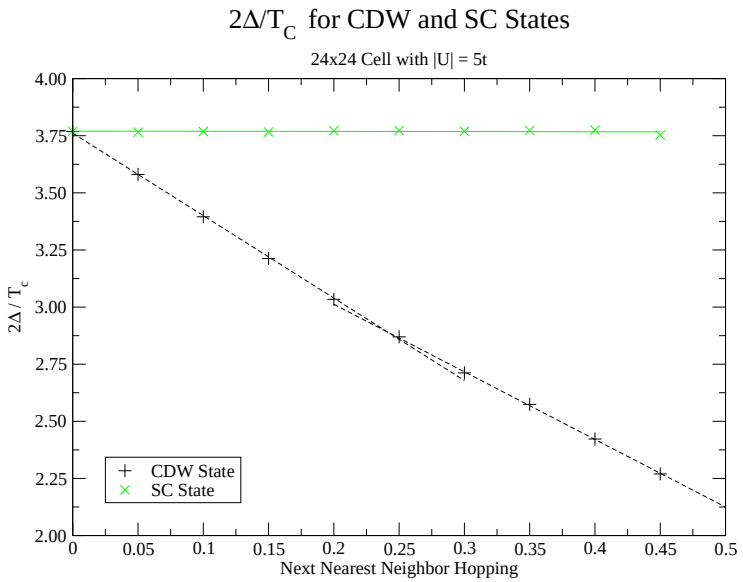

(b) $2\Delta/T_c$ vs. t' for CDW and SC states

Figure 5.16: Dependence of gap size and T_c on t' for the CDW and SC states on a 24x24 lattice with $|U| = 5t$. (a) The critical temperature is gradually reduced as t' increases while the gap size decreases linearly. (b) For the CDW state one can see a definite slope change in the gap to T_c ratio around $t' \sim 0.25$, while in the SC state the ratio remains constant at the BCS value.

the real part of the dielectric response function are shown in Figure 5.17 for $0 \leq t' \leq 0.45$. A divergence at the wavevector $\vec{Q}_{CDW} = (\pm\pi/a, \pm\pi/a)$ can clearly be seen for all values of t', and is largest for perfect nesting at $t' = 0$. When t' is increased, the magnitude of the divergence rapidly decreases by an order of magnitude between $t' = 0$ and 0.1, and between $t' = 0.25$ and 0.45 there is no noticeable change. For $t' > 0.25$ the enhanced density of states at the vHs results in a growing contribution to the divergence, and the overall divergence of the response remains constant. This shows that when $t' > 0.25$ the divergence at $\vec{Q}_{CDW}$ is a result of the van Hove singularity contribution being more dominant than that of Fermi surface nesting.

Although it is not possible to determine the precise contribution from either nesting or the vHs to the CDW instability, what we do know for certain is that as t' grows, conventional nesting plays a significantly smaller role. The evidence presented above, including enhancement of the density of states at the vHs, divergence of the dielectric response function, and the slope change in $2\Delta/T_c$ suggest that for $t' > 0.25$ the van Hove singularity is the primary mechanism responsible for the CDW instability in our model. This provides an excellent opportunity for studying the interplay of CDW with SC, as we have identified two regimes in which the CDW is a result of different mechanisms, and allows us to determine under which circumstances superconductivity can coexist with CDW.

For the CDW state the ratio $2\Delta/T_c$ was shown to be t'-dependent; however, for the SC state this ratio has a fundamentally different behaviour. As already seen in Figure 5.16(b) neither the SC gap nor the critical temperature varies with t', and for large coupling strength ($|U| = 5t$) the ratio stays constant near the BCS value. For small coupling $|U| \approx 1.5t$, the ratio is dependent on t', though only very weakly. For $|U| = 1.5t$ the gap size varies by roughly 35% between $t' = 0$ and $t' = 0.45$ and the variation rapidly decreases to less than 7% for $|U| = 2t$. Such variation is not surprising since for such small electron-phonon coupling strengths the SC interaction and the kinetic energy are comparable. When the on-site coupling strength is much larger than the kinetic energy, we find that the variation of the Fermi surface has little effect on superconductivity.

The behaviour of the superconducting state is quite distinct from the CDW state. This can be seen in Figure 5.18 which shows the superconducting density of states for various

$Re\ \epsilon(\vec{q}, \omega \to 0)$

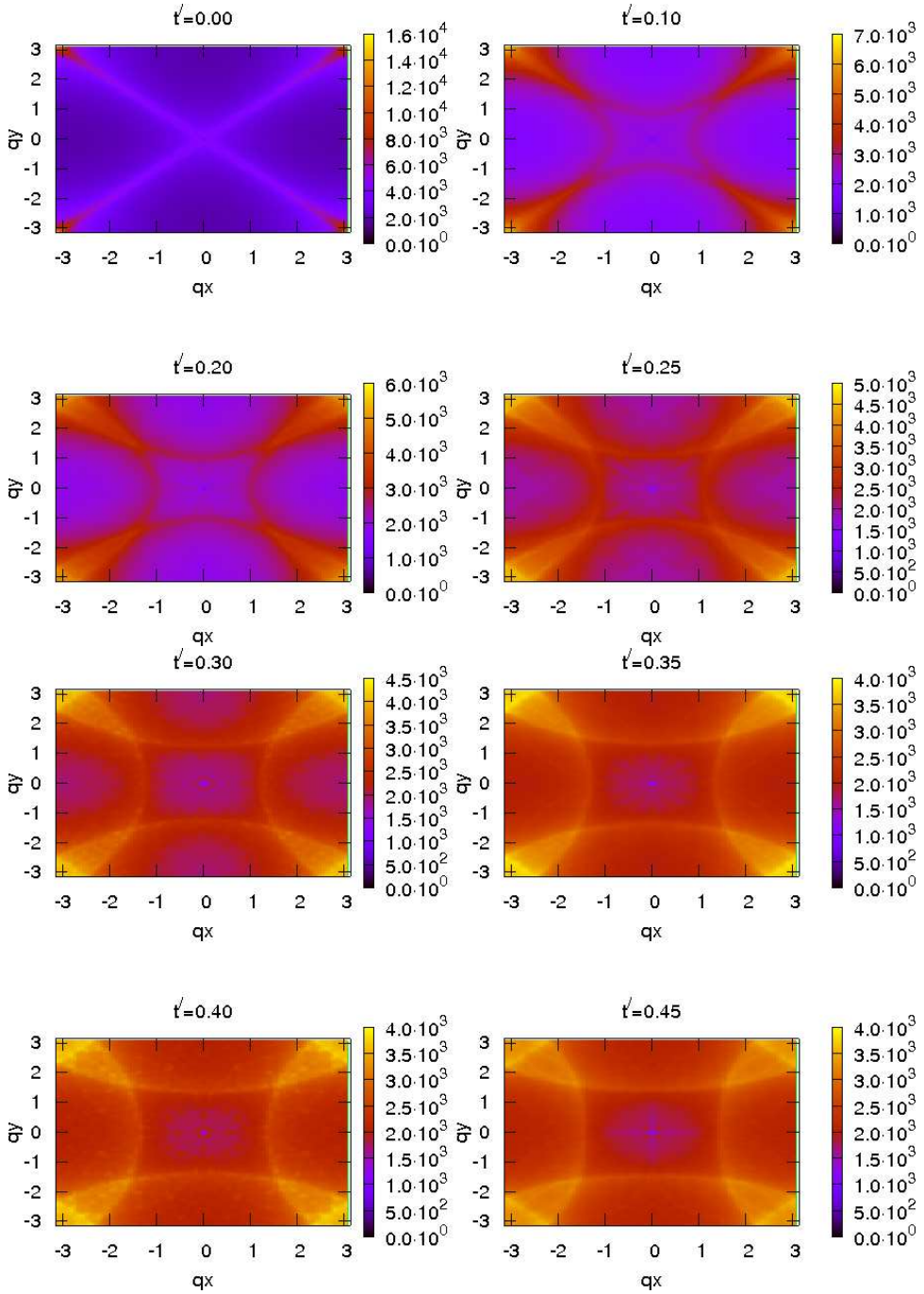

Figure 5.17: $Re\ \epsilon(\vec{q}, \omega \to 0)$ for $0 \leq t' \leq 0.45$. The divergence at the nesting vector $\vec{q} = (\pm\pi/a, \pm\pi/a)$ can clearly be seen for all t'. As the Fermi surface changes its shape in the dispersion and perfect nesting is destroyed, the divergence rapidly decreases and begins to level off at $t' \sim 0.25$, indicating that the vHs becomes dominant.

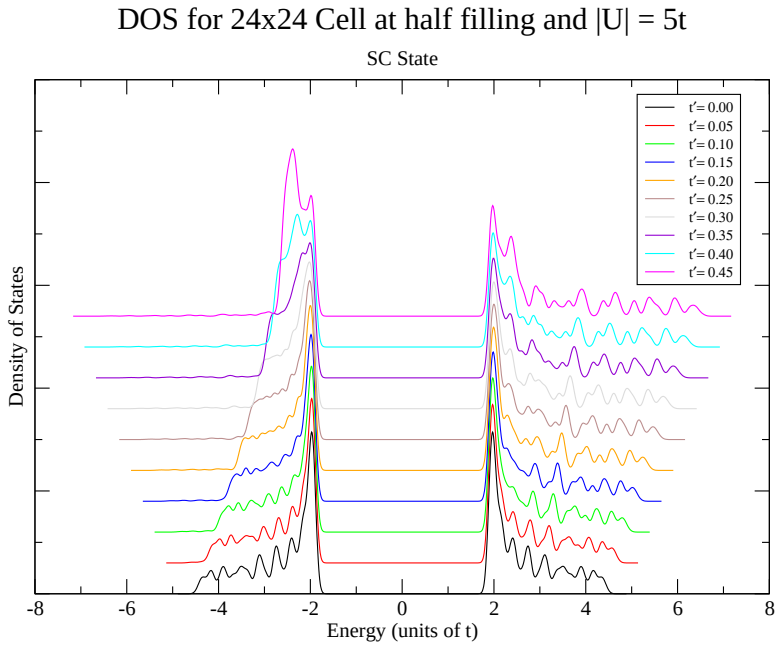

Figure 5.18: Density of States for various values of t'. The results are shifted vertically for clarity. These results were obtained using a 24x24 cell at half filling using an onsite coupling parameter of $|U| = 5t$ in the superconducting state.

values of t' for $|U| = 5t$. The SC DOS (ignoring the "artificial" states) somewhat reflects the change of the Fermi surface; however, the gap size is independent of t'. It is important to keep in mind that the electron density is uniform for the SC state and as a result the LDOS is identical at every site in the lattice. In this case the site-averaged density of states and the local DOS are identical. Figure 5.18 shows another feature that is distinct from the CDW state: the DOS at the van Hove singularity is quite featureless. This is because for the superconducting state the energy gap in the DOS is a result of the anomalous coupling between particle and hole states (i.e., the off diagonal component $\hat{\Delta}$ in the Hamiltonian), and represents the energy required to break a Cooper pair and create particle-hole excitations. The apparent abscence of any feature at the vHs can be explained by the effect of the BCS gap on the density of states. According to the BCS theory and Equation (2.10), the quasiparticle excitation energy in the SC state has the form

$$E_k = \sqrt{\epsilon_k^2 + \Delta^2}\ . \tag{5.15}$$

where ϵ_k is the single particle kinetic energy and $\Delta_k \equiv \Delta$. Since there is a one-to-one correspondence between single-particle states in the normal and SC states one finds that the density of states in the superconducting state is given by [43]

$$\begin{aligned} N_S(E_k)dE &= N_N(\epsilon_k)d\epsilon \\ \frac{N_S(E_k)}{N(0)} &= \frac{d\epsilon_k}{dE} \end{aligned}$$

where we have approximated the density of states in the normal state around the chemical potential to be approximately constant $N_N(\epsilon) \approx N(0)$. Evaluating (5.15) gives the density of states in the superconducting state as

$$\frac{N_S(E_k)}{N(0)} = \begin{cases} \frac{E_k}{\sqrt{E_k^2 - \Delta^2}} & E_k > \Delta\ , \\ 0 & E_k < \Delta\ . \end{cases} \tag{5.16}$$

This means that a singularity in the density of states develops at $E_k = \pm\Delta$ generating the familiar coherence peaks around the chemical potential. Excitations in the superconducting state occur close to the chemical potential, and therefore the singularity at the saddle points (which is below the Fermi level) is relatively unaffected. This implies that contrary to the CDW state, which is strongly dependent on t', the superconducting state is quite robust against changes of the Fermi surface. For intermediate to strong electron-phonon coupling, the SC state is barely affected by the next-nearest neighbour hopping parameter t'.

As the results presented in Figure 5.16(b) show, the behaviour of the CDW and SC states are fundamentally different. The CDW state is very sensitive to changes in the Fermi surface, while the SC state is not. The difference between the two states stems from the difference between anomalous and diagonal coupling. In the superconducting state the particle and hole amplitudes are coupled via the order parameter, and near the Fermi surface an excitation is a complicated mixture of both. Thus in the superconducting state, the coherence peaks with the square-root behaviour in Equation (5.16) stay well-defined even for $t' > 0$. The CDW state on the other hand has particle and hole amplitudes decoupled and the excitations are independent of each other, meaning that Fermi surface changes can have a significant

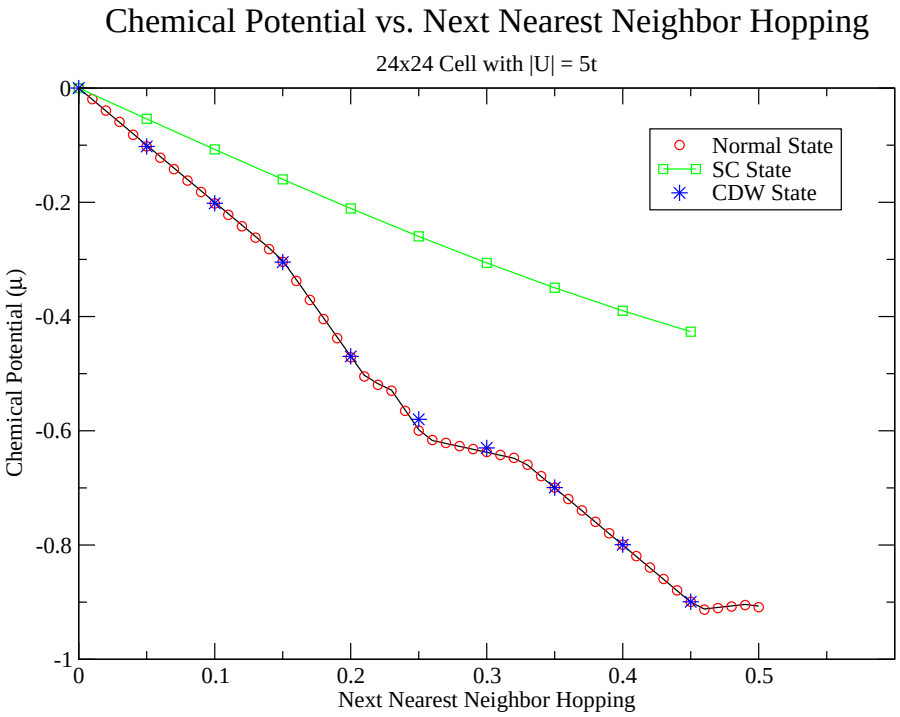

Figure 5.19: Chemical potential for $0 \leq t' \leq 0.5$ for $|U| = 5t$ on a 24x24 lattice. Results are shown for the normal, superconducting, and CDW states. One can see that the chemical potential as a function of t' behaves identically for the CDW and normal states; however, there is a very different behaviour in the SC state. This is a result of the anomalous coupling between particle and hole amplitudes in the SC state.

impact. This can be seen in the chemical potential, which is a representation of the energy required to change the particle number of the system by one. Figure 5.19 shows the chemical potential for the normal, CDW, and superconducting states as a function of t'. The chemical potential is identical for both the CDW and normal states. It is, however, much lower in the SC state. What this indicates is that it is relatively easy to add or remove particles in the SC state as compared to the CDW or normal states. The mixing between particles and holes in the SC state via the anomalous coupling is what makes it the SC state so robust to Fermi surface changes.

What we have identified so far is that as the next-nearest neighbour hopping is enhanced, the Fermi surface begins to change shape. As this happens the perfect nesting at $t' = 0$ is destroyed and contributions to the CDW from the vHs begins to become more dominant. Both the energy gap and transition temperature are reduced, indicating that the stability of the CDW state is suppressed as nesting is reduced. Conversely, for intermediate to strong

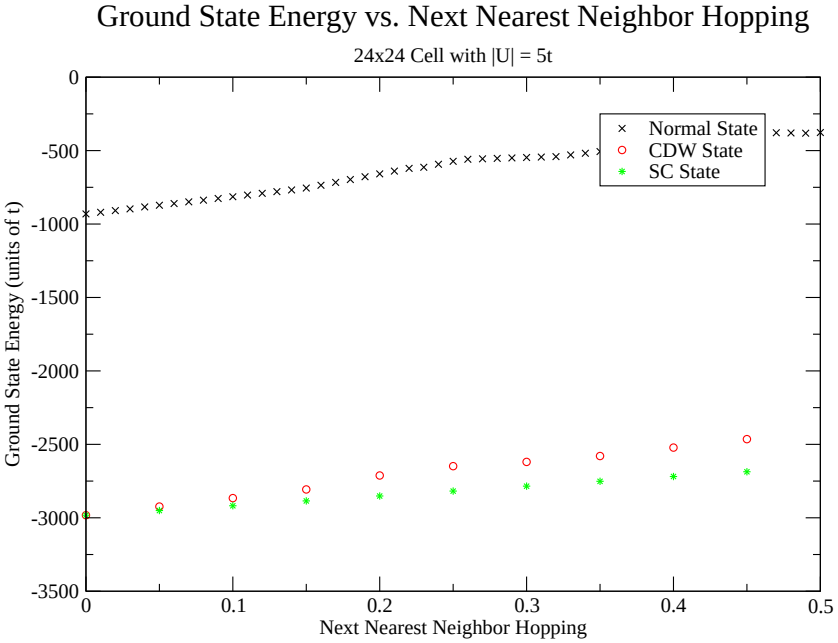

Figure 5.20: Ground state energy for $0 \leq t' \leq 0.5$ for $|U| = 5t$ on a 24x24 lattice. Results are shown for the normal, superconducting, and CDW states. At $t' = 0$ the SC and CDW states have identical ground-state energy and is considerably lower than the normal-state energy. However for $t' \neq 0$ the energies split and the SC state always has the lowest energy. The behaviour of the normal and CDW states energy curves is a result of the dependence of the chemical potential on t'.

coupling strengths the superconducting state is hardly affected by t', and as shown in Figure 5.16(b), it is quite robust against Fermi surface changes. In Section 5.1.3 it has been shown that for $t' = 0$ the SC and CDW states are degenerate and can coexist. For $t' \neq 0$, however, we have not found such a mixed state solution, as the solution always converges to a uniform SC state. In order to understand the relationship between the CDW and SC states, the ground-state energy has been computed as a function of t' and is shown in Figure 5.20 for the SC, CDW, and normal states. At $t' = 0$ the CDW and SC states are degenerate; however this degeneracy is removed as soon as t' becomes nonzero. The SC state always has lower energy than the CDW state. This observation explains why we have not been able to find mixed-state solutions, as the BdG equations tend to converge to the state with the lowest energy.

The condensation energy of the SC and CDW states, which is the ground-state energy

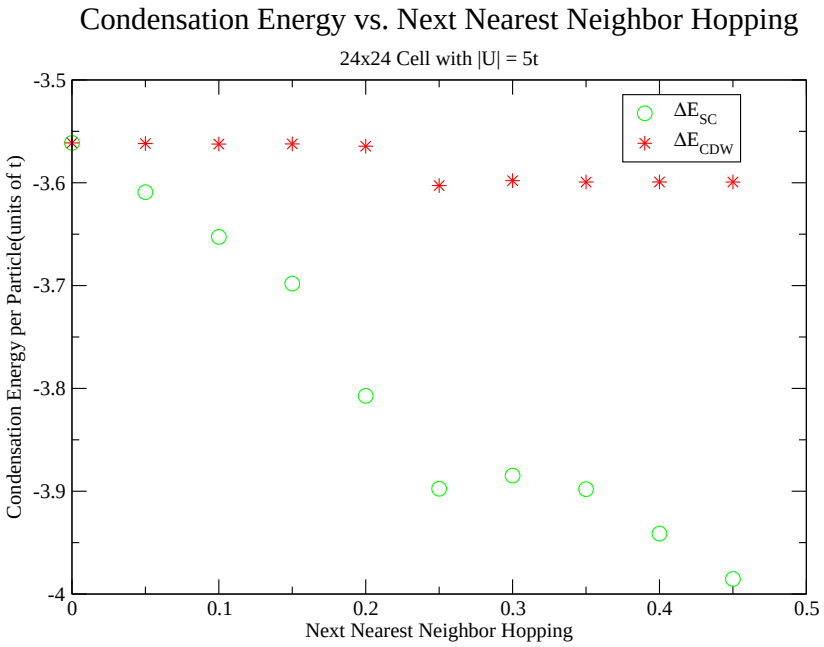

Figure 5.21: Condensation energy per particle for SC and CDW states. The condensation energy is the difference in energy between the SC/CDW and normal states. The larger condensation energy for the SC state indicates that it is the most stable configuration. The increase in the CDW condensation energy near $t' = 0.25$ may indicate that a vHs driven CDW is more stable than due to nesting.

per particle measured with respect to the normal state (i.e., kinetic energy), can also provide crucial information regarding the nature and stability of these two states. The condensation energy per particle is shown in Figure 5.21 for both the CDW and SC states as as function of t'. This energy is a representation of the energy saved by forming the CDW or SC states. Since the SC condensation energy is always greater than the CDW energy, this result verifies the interpretation of Figure 5.20 that the SC state is always preferred for $t' \neq 0$. Interestingly, the SC condensation energy strongly depends on t', while the CDW energy does not. At first sight, this appears to be contradictory to the fact that Δ and T_c are independent of t'. This t' dependence of the SC condensation energy, however, can be explained by inspecting the density of states in Figure 5.3. As the vHs moves toward negative energy, the hole-excitation states in the vicinity of the gap edge are drastically reduced. This change is reflected in the condensation energy; the SC state becoming more stable as t' increases. Additionally, the dip shape in both SC and CDW condensation energy around $t' = 0.25$ is a result of the different behaviour of the chemical potential in the SC and normal states. For the CDW state the

condensation energy is a reflection of the energy needed to destroy the regular/periodic density modulations in the sample. Once the CDW has formed, this energy is fixed and does not depend on t'. Intriguingly, Figure 5.21 also indicates a small increase of the CDW condensation energy for $t' \gtrsim 0.25$. Given that we have identified the vHs as the source of the CDW instability in this regime, this may indicate that a vHs-driven CDW is more stable than that due to nesting.

The results presented in this chapter provide an interesting insight into the interplay of charge density modulations and superconductivity. We have seen that when there is perfect nesting of the Fermi surface ($t' = 0$), the CDW can coexist with superconductivity. When perfect nesting is destroyed ($t' \neq 0$), diminishing T_c and gap size indicate that the CDW state is suppressed. In addition, pseudogap behaviour, enhancement of the density of states at the vHs, divergence of the dielectric response, and a slope change in $2\Delta/T_c$ all indicate a transition from nesting to a vHs mechanism for the CDW instability in our model. Ground-state energy calculations show that once perfect nesting is removed and the saddle-point mechanism has a more dominant role, the CDW and SC states can no longer coexist. In this case the SC ground-state is always preferred.

Chapter 6

Conclusion

Recent studies of the transition metal dichalcogenide 2H-$NbSe_2$ have led to extensive debate in the scientific community regarding the mechanism for the CDW instability in this material [24, 25]. Additionally, the precise nature of the relationship between charge density modulations and superconductivity is not known. In this thesis the Bogoliubov-de Gennes (BdG) equations formulated on a tight-binding lattice have been used to study the interplay of charge density waves (CDW) and superconductivity (SC). As the BdG equations have high numerical demand, software which utilizes parallel algorithms have been developed to solve these equations directly and numerically. Calculations were performed on a large-scale Beowulf-class PC cluster at the University of Saskatchewan.

In this thesis, we have first studied the effects of open boundaries and a single impurity in nanoscale superconductors. The presence of a surface or an impurity tends to cause charge density modulations and inhomogeneous superconductivity. Is has been found that in our tight-binding system at half filling, s-wave superconductivity is quite robust against the existence of surfaces: the ground state is three-fold degenerate with a pure CDW (no SC) state, a pure SC (no CDW) state, and a state in which CDW and SC coexist. In contrast, d-wave superconductivity is surface-sensitive and suppressed along the surface boundaries. We have then examined the influence of a single attractive impurity deposited at the centre of a nanoscale superconductor. It has been demonstrated that a *weakly* attractive impurity potential can lead to significant suppression of the superconducting order parameter, more so than a strong impurity. Perhaps the most fascinating result has come from the study of various d-wave coupling strengths in the presence of a weak impurity. We have found that in a nanoscale d-wave superconductor with strong electron-phonon coupling, the scattering by a *weakly* attractive impurity can indeed kill superconductivity in the bulk of the sample,

leaving "surface superconductivity" only.

Calculations for periodic systems also show that CDW can coexist with s-wave superconductivity. Since this system is pure in the sense that there are no boundaries or impurities, the density modulations must be a result of an electronic instability of the normal state. To identify the mechanism of the instability, the single-particle Hamiltonian was modified to include the hopping integral between next-nearest neighbour sites (t'), which changes the shape of the Fermi surface. It was demonstrated that the CDW state is strongly dependent on t' and that the transition temperature T_{CDW} is suppressed as the Fermi surface changes its shape. By studying the dielectric response, the density of states, and the ratio $2\Delta/T_c$, it has been found that for $t' < 0.25$ the CDW instability is mostly a result of the conventional Fermi surface nesting, while for $t' > 0.25$ it is dominated by the van-Hove singularity mechanism of Rice and Scott [1].

In contrast to the CDW state, we have found that the superconducting state with uniform density distribution does *not* depend on t'. The difference between the CDW and homogeneous SC states in this regard stems from the anomalous, or off-diagonal, coupling between particle and hole components of a quasiparticle in the SC state. As the particle and hole amplitudes are coupled by the order parameter, superconductivity is quite robust against changes of the Fermi surface.

To study the coexistence of CDW and SC, the ground-state energy as a function of t' was calculated for both the CDW and SC states. It was found that except for $t' = 0$, superconductivity is always the preferred ground state. Since $t' = 0$ is the only point where there is perfect nesting of the Fermi surface, these results indicate that within our model, when the CDW instability is a result of the vHs scenario, SC and CDW can no longer coexist. The authors of [25] have concluded from their ARPES measurements that the CDW in 2H-$NbSe_2$ is a result of nesting. It must be kept in mind, however, that the nesting points in momentum space found in [25] are far from the conditions required for perfect nesting. The dispersion along k_z [32] means that the contribution to the divergence of the dielectric response can be rather weak, if any. Combined with the fact that resistivity measurements favour the vHs scenario, it is possible that the CDW instability in 2H-$NbSe_2$ is a result of combined contributions from both the saddle-point and nesting mechanisms.

The results presented in this thesis show that within our model, a vHs-driven CDW cannot coexist with SC. It is important, however, to consider the scope to which our results may apply. Our model calculations are relevant only for one-band, isotropic, s-wave superconductivity. It is a well-established fact, however, that 2H-$NbSe_2$ is a *multiple-band* superconductor [48, 49]. Moreover, one may have to take into consideration anisotropic effects due to the shape of the Fermi surfaces and possibly momentum (FS sheet)-dependent electron-phonon coupling. Therefore, in order to properly understand the experimental data on 2H-$NbSe_2$, the BdG equations must be extended to account for multiple bands and possibly anisotropic effects.

The interplay between CDW and SC is one of the most challenging problems facing researchers in condensed matter physics today. It has long been the consensus that charge density waves should compete with superconductivity. The results presented in this thesis, however, have illustrated that this is not *always* the case and CDW and SC can in fact coexist. Whether CDW enhances or competes with SC is still an open question. It is hoped that the results presented in this thesis provide motivation for further research.

References

[1] T. M. Rice and G. K. Scott. New mechanism for a charge-density-wave instability. *Phys. Rev. Lett.*, 35(2):120–123, Jul 1975.

[2] H. Kamerlingh Onnes. *Comm. Leiden*, 1911.

[3] T. Shachtman. *Absolute Zero and the Conquest of Cold*. Mariner Books, 2000.

[4] C.W. Chu, L. Gao, F. Chen, Z.J. Huang, R.L. Meng, and Y.Y. Xue. Superconductivity above 150 K in $HgBa_2Ca_2Cu_3O_{8+\delta}$ at high pressures. *Nature*, 365:323–325, September 1993.

[5] J. G. Bednorz and K. A. Müller. Possible high-T_c superconductivity in the Ba-La-Cu-O system. *Zeitschrift für Physik B Condensed Matter*, 64:189–193, 1986. 10.1007/BF01303701.

[6] R.G. Parr W. Kohn, A.D. Becke. Density functional theory of electronic structure. *J. Phys. Chem*, 100(31):12974–12980, August 1996.

[7] W. Kohn and L. J. Sham. Self-consistent equations including exchange and correlation effects. *Phys. Rev.*, 140(4A):A1133–A1138, Nov 1965.

[8] A. M. Gabovich, A. I. Voitenko, T. Ekino, Mai Suan Li, H. Szymczak, and M. Pekala. Competition of superconductivity and charge density waves in cuprates: Recent evidence and interpretation. *Advances in Condensed Matter Physics*, 2010, Sept 2009.

[9] A. M. Gabovich, A. I. Voitenko, and M. Ausloos. Charge- and spin-density waves in existing superconductors: competition between cooper pairing and peierls or excitonic instabilities. *Physics Reports*, 367(6):583 – 709, 2002.

[10] T. Valla, A. V. Fedorov, P. D. Johnson, P-A. Glans, C. McGuinness, K. E. Smith, E. Y. Andrei, and H. Berger. Quasiparticle Spectra, Charge-Density Waves, Superconductivity, and Electron-Phonon Coupling in $2H - NbSe_2$. *Phys. Rev. Lett.*, 92(8):086401, Feb 2004.

[11] S. V. Borisenko, A. A. Kordyuk, A. N. Yaresko, V. B. Zabolotnyy, D. S. Inosov, R. Schuster, B. Büchner, R. Weber, R. Follath, L. Patthey, and H. Berger. Pseudogap and charge density waves in two dimensions. *Phys. Rev. Lett.*, 100(19):196402, May 2008.

[12] C. Kallin M. R. Norman, D. Pines. The pseudogap: friend or foe of high Tc? *Advances in Physics*, 54:715–733, 2005.

[13] A Yazdani. Visualizing pair formation on the atomic scale and the search for the mechanism of superconductivity in high-tc cuprates. *Journal of Physics: Condensed Matter*, 21(16):164214, 2009.

[14] R L Withers and J A Wilson. An examination of the formation and characteristics of charge-density waves in inorganic materials with special reference to the two- and one-dimensional transition-metal chalcogenides. *Journal of Physics C: Solid State Physics*, 19(25):4809, 1986.

[15] R.V. Coleman, B. Giambattista, P.K. Hansma, A. Johnson, W.W. McNairy, and C.G. Slough. Scanning tunnelling microscopy of charge-density waves in transition metal chalcogenides. *Advances in Physics*, 37(6):559, 1988.

[16] H. Mutka. Superconductivity in irradiated charge-density-wave compounds $2H-NbSe_2$, $2H-TaS_2$, and $2H-TaSe_2$. *Phys. Rev. B*, 28(5):2855–2858, Sep 1983.

[17] J.A. Wilson, F.J. Di Salvo, and S. Mahajan. Charge-density waves and superlattices in the metallic layered transition metal dichalcogenides. *Advances in Physics*, 50(8 SPEC.):1171 – 1248, 2001. Charge-density waves;.

[18] Rudolph Peierls. *Quantum Theory of Solids*. Clarendon Press, Oxford, 1955.

[19] Rudolph Peierls. *More Surprises in Theoretical Physics*. Princeton University Press, 1991.

[20] G. Grüner. The dynamics of charge-density waves. *Rev. Mod. Phys.*, 60(4):1129–1181, Oct 1988.

[21] J. A. Wilson, F. J. Di Salvo, and S. Mahajan. Charge-density waves in metallic, layered, transition-metal dichalcogenides. *Phys. Rev. Lett.*, 32(16):882–885, Apr 1974.

[22] R. S. Markiewicz. A survey of the van hove scenario for high-tc superconductivity with special emphasis on pseudogaps and striped phases. *Journal of Physics and Chemistry of Solids*, 58(8):1179 – 1310, 1997.

[23] D. E. Moncton, J. D. Axe, and F. J. DiSalvo. Neutron scattering study of the charge-density wave transitions in $2H-TaSe_2$ and $2H-NbSe_2$. *Phys. Rev. B*, 16(2):801–819, Jul 1977.

[24] T. Kiss, T. Yokoya, A. Chainani, S. Shin, T. Hanaguri, M. Nohara, and H. Takagi. Charge-order-maximized momentum-dependent superconductivity. *Nature Physics*, 3:720–725, October 2007.

[25] S. V. Borisenko, A. A. Kordyuk, V. B. Zabolotnyy, D. S. Inosov, D. Evtushinsky, B. Büchner, A. N. Yaresko, A. Varykhalov, R. Follath, W. Eberhardt, L. Patthey, and H. Berger. Two Energy Gaps and Fermi-Surface "Arcs" in $NbSe2$. *Phys. Rev. Lett.*, 102(16):166402, Apr 2009.

[26] L. F. Mattheiss. Band structures of transition-metal-dichalcogenide layer compounds. *Phys. Rev. B*, 8(8):3719–3740, Oct 1973.

[27] R Corcoran, P Meeson, Y Onuki, P A Probst, M Springford, K Takita, H Harima, G Y Guo, and B L Gyorffy. Quantum oscillations in the mixed state of the type II superconductor 2H-$NbSe_2$. *Journal of Physics: Condensed Matter*, 6(24):4479, 1994.

[28] M. D. Johannes, I. I. Mazin, and C. A. Howells. Fermi-surface nesting and the origin of the charge-density wave in $NbSe_2$. *Phys. Rev. B*, 73(20):205102, May 2006.

[29] Th. Straub, Th. Finteis, R. Claessen, P. Steiner, S. Hüfner, P. Blaha, C. S. Oglesby, and E. Bucher. Charge-Density-Wave Mechanism in $2H - NbSe_2$: Photoemission Results. *Phys. Rev. Lett.*, 82(22):4504–4507, May 1999.

[30] W. C. Tonjes, V. A. Greanya, Rong Liu, C. G. Olson, and P. Molinié. Charge-density-wave mechanism in the $2H-NbSe_2$ family: Angle-resolved photoemission studies. *Phys. Rev. B*, 63(23):235101, May 2001.

[31] T. Yokoya, T. Kiss, A. Chainani, S. Shin, M. Nohara, and H. Takagi. Fermi Surface Sheet-Dependent Superconductivity in 2H-$NbSe_2$. *Science*, 294(5551):2518–2520, 2001.

[32] K. Rossnagel, O. Seifarth, L. Kipp, M. Skibowski, D. Voß, P. Krüger, A. Mazur, and J. Pollmann. Fermi surface of $2H - NbSe_2$ and its implications on the charge-density-wave mechanism. *Phys. Rev. B*, 64(23):235119, Nov 2001.

[33] Takayuki Kiss, Takayoshi Yokoya, Ashish Chainani, Shik Shin, Minoru Nohara, and Hidenori Takagi. Fermi surface and superconducting gap of 2H-$NbSe_2$ using low-temperature ultrahigh-resolution angle-resolved photoemission spectroscopy. *Physica B: Condensed Matter*, 312-313:666 – 667, 2002.

[34] Ryan L. Barnett, Anatoli Polkovnikov, Eugene Demler, Wei-Guo Yin, and Wei Ku. Coexistence of Gapless Excitations and Commensurate Charge-Density Wave in the $2H$ Transition Metal Dichalcogenides. *Phys. Rev. Lett.*, 96(2):026406, Jan 2006.

[35] J. Bardeen, L. N. Cooper, and J. R. Schrieffer. Theory of superconductivity. *Phys. Rev.*, 108(5):1175–1204, Dec 1957.

[36] John Bardeen and David Pines. Electron-phonon interaction in metals. *Phys. Rev.*, 99(4):1140–1150, Aug 1955.

[37] Leon N. Cooper. Bound electron pairs in a degenerate fermi gas. *Phys. Rev.*, 104(4):1189–1190, Nov 1956.

[38] J. R. Schrieffer. *Theory of Superconductivity*, pages 47–48. W.A. Benjamin, Inc., Publishers, 1964.

[39] Otfried Madelung. *Introduction to Solid-State Theory*. Springer, 1978.

[40] M. D. Johannes and I. I. Mazin. Fermi surface nesting and the origin of charge density waves in metals. *Phys. Rev. B*, 77(16):165135, Apr 2008.

[41] W. Kohn. Image of the fermi surface in the vibration spectrum of a metal. *Phys. Rev. Lett.*, 2(9):393–394, May 1959.

[42] M. Dressel. Peierls instability and charge density waves. `http://www.pi1.uni-stuttgart.de/glossar/Peierls_e.php`, 2008.

[43] M. Tinkham. *Introduction to Superconductivity*. Dover Publication, Inc., Second Editions, 1995.

[44] L.P. Gor'kov. On the energy spectrum of superconductors. *Sov. Phys. JETP*, 7:505–508, 1958.

[45] P. de Gennes. *Superconductivity of Metals and Alloys*. Boulder, CO: Westview Press, 1999.

[46] S. Hufner. *Photoelectron Spectroscopy*. Springer-Verlag, 1995.

[47] Øystein Fischer, Martin Kugler, Ivan Maggio-Aprile, Christophe Berthod, and Christoph Renner. Scanning tunneling spectroscopy of high-temperature superconductors. *Rev. Mod. Phys.*, 79(1):353–419, Mar 2007.

[48] C. L. Huang, J.-Y. Lin, Y. T. Chang, C. P. Sun, H. Y. Shen, C. C. Chou, H. Berger, T. K. Lee, and H. D. Yang. Experimental evidence for a two-gap structure of superconducting $NbSe_2$: A specific-heat study in external magnetic fields. *Phys. Rev. B*, 76(21):212504, Dec 2007.

[49] M. Zehetmayer and H. W. Weber. Experimental evidence for a two-band superconducting state of $NbSe_2$ single crystals. *Phys. Rev. B*, 82(1):014524, Jul 2010.

Appendix A

BdG Equations in the Tight-Binding Model

A.1 Derivation of the BdG Equations

The mean field Hamiltonian in our model is

$$\begin{aligned} H_{eff} &= H_0 + \sum_{i\sigma} V_{ii}^{(H)} \hat{n}_{i\sigma} + \frac{1}{2} \sum_{\langle ij \rangle \sigma} V_{ij}^{(H)} \hat{n}_{i\sigma} - \frac{1}{2} \sum_{\langle ij \rangle \sigma} V_{ij}^{(F)} c_{i\sigma}^{\dagger} c_{j\sigma} \\ &\quad + \sum_{i} \Delta_{ii} c_{i\uparrow}^{\dagger} c_{i\downarrow}^{\dagger} + \frac{1}{2} \sum_{\langle ij \rangle} \Delta_{ij} c_{i\uparrow}^{\dagger} c_{j\downarrow}^{\dagger} + H.c. \end{aligned} \tag{A.1}$$

We wish to make a transformation to a basis such that the Hamiltonian is diagonal, i.e.,

$$H_{eff} = E_0 + \sum_{n\sigma} \epsilon_n \gamma_{n\sigma}^{\dagger} \gamma_{n\sigma} \ , \tag{A.2}$$

where E_0 is the ground-state energy, and ϵ_n is the energy of a quasiparticle excitation in state n. In this representation the new operators $\gamma_{n\sigma}$ and $\gamma_{n\sigma}^{\dagger}$ create and destroy excitations with respect to the ground state. Since the form of the quasiparticle operators must be invariant under a canonical transformation, the quasiparticle operators must also obey the fermion anti-commutation relations,

$$\left\{ \gamma_{m\sigma} \gamma_{n\sigma'}^{\dagger} \right\} = \delta_{mn} \delta_{\sigma\sigma'} \, , \tag{A.3}$$

$$\left\{ \gamma_{m\sigma} \gamma_{n\sigma'} \right\} = 0 \, , \tag{A.4}$$

$$\left\{ \gamma_{m\sigma}^{\dagger} \gamma_{n\sigma'}^{\dagger} \right\} = 0 \, . \tag{A.5}$$

Therefore in the basis in which H_{eff} is diagonal we have

$$\left[H_{eff}, \gamma_{n\sigma}^{\dagger} \right] = \sum_{n'\sigma'} \epsilon_{n'} \left[\gamma_{n'\sigma'}^{\dagger} \gamma_{n'\sigma'}, \gamma_{n\sigma}^{\dagger} \right] \ .$$

Using the identity

$$[AB, C] = A \{B, C\} - \{A, C\} B \ , \tag{A.6}$$

one has,

$$\begin{aligned} \left[H_{eff}, \gamma_{n\sigma}^{\dagger} \right] &= \sum_{n'\sigma'} \epsilon_{n'} \left(\gamma_{n'\sigma'}^{\dagger} \left\{ \gamma_{n'\sigma'}, \gamma_{n\sigma}^{\dagger} \right\} - \left\{ \gamma_{n'\sigma'}^{\dagger}, \gamma_{n\sigma}^{\dagger} \right\} \gamma_{n'\sigma'} \right) \\ &= \sum_{n'\sigma'} \epsilon_{n'} \gamma_{n'\sigma'}^{\dagger} \delta_{nn'} \delta_{\sigma\sigma'} \\ &= \epsilon_n \gamma_{n\sigma}^{\dagger} \ . \end{aligned}$$

Similarly,

$$\begin{aligned}\left[H_{eff},\gamma_{n\sigma}\right] &= \sum_{n'\sigma'}\epsilon_{n'}\left[\gamma^{\dagger}_{n'\sigma'}\gamma_{n'\sigma'},\gamma_{n\sigma}\right]\\ &= \sum_{n'\sigma'}\epsilon_{n'}\left(\gamma^{\dagger}_{n'\sigma'}\Big\{\gamma_{n'\sigma'},\gamma_{n\sigma}\Big\}-\Big\{\gamma^{\dagger}_{n'\sigma'},\gamma_{n\sigma}\Big\}\gamma_{n'\sigma'}\right)\\ &= -\sum_{n'\sigma'}\epsilon_{n'}\gamma_{n'\sigma'}\delta_{nn'}\delta_{\sigma\sigma'}\\ &= -\epsilon_n\gamma_{n\sigma}\ .\end{aligned}$$

The transformation which diagonalizes the mean-field Hamiltonian is the Bogoliubov-Valatin transformation, and gives the electron annihilation operators in terms of the quasiparticle operators:

$$c_{i\uparrow} = \sum_n\left(\gamma_{n\uparrow}u_n(i)-\gamma^{\dagger}_{n\downarrow}v^{\star}_n(i)\right) \tag{A.7}$$

$$c_{i\downarrow} = \sum_n\left(\gamma_{n\downarrow}u_n(i)+\gamma^{\dagger}_{n\uparrow}v^{\star}_n(i)\right) \tag{A.8}$$

Thus by computing the commutators $[H_{eff},c_{i\uparrow}]$ and $[H_{eff},c_{i\downarrow}]$ explicitly and comparing coefficients we arrive at the BdG equations.

We begin by calculating the commutators term by term. To keep the calculation manageable, I break up the Hamiltonian into the single-particle, $s-$ and $d-$wave components, where

$$\begin{aligned}H_0 &= \sum_{\langle ij\rangle\sigma}\tilde{t}_{ij}c^{\dagger}_{i\sigma}c_{j\sigma}+\sum_{i\sigma}\left(\epsilon_i-\tilde{\mu}\right)\hat{n}_{i\sigma}\ ,\\ H_s &= \sum_i\left(\Delta_{ii}c^{\dagger}_{i\uparrow}c^{\dagger}_{i\downarrow}+\Delta^{\star}c_{i\downarrow}c_{i\uparrow}\right)\ ,\\ H_d &= \frac{1}{2}\sum_{<i,j>\sigma}V^{(H)}_{ij}n_{i\sigma}+\frac{1}{2}\sum_{<i,j>}\left(\Delta_{ij}c^{\dagger}_{i\uparrow}c^{\dagger}_{j\downarrow}+\Delta^{\star}_{ij}c_{j\downarrow}c_{i\uparrow}\right)\ .\end{aligned}$$

For simplicity I have defined

$$\begin{aligned}\tilde{t}_{ij} &= t_{ij}-\frac{1}{2}V^{(F)}_{ij}\ ,\\ \tilde{\mu} &= \mu-V^{(H)}_{ii}\ .\end{aligned}$$

The quantity of interest is then,

$$\left[H_{eff},c_{k\uparrow}\right]=\left[H_0,c_{k\uparrow}\right]+\left[H_s,c_{k\uparrow}\right]+\left[H_d,c_{k\uparrow}\right]\ . \tag{A.9}$$

The first term is,

$$\left[H_0,c_{k\uparrow}\right] = \sum_{\langle ij\rangle\sigma}\tilde{t}_{ij}\left[c^{\dagger}_{i\sigma}c_{j\sigma},c_{k\uparrow}\right]+\sum_{i\sigma}\left(\epsilon_i-\tilde{\mu}\right)\left[\hat{n}_{i\sigma},c_{k\uparrow}\right]\ .$$

Evaluating the commutators,

$$\begin{aligned}\left[c^\dagger_{i\sigma}c_{j\sigma},c_{k\uparrow}\right] &= c^\dagger_{i\sigma}\left\{c_{j\sigma},c_{k\uparrow}\right\}-\left\{c^\dagger_{i\sigma},c_{k\uparrow}\right\}c_{j\sigma}\\ &= -c_{j\sigma}\delta_{ik}\delta_{\sigma\uparrow}\ ,\end{aligned}$$

$$\begin{aligned}\left[c^\dagger_{i\sigma}c_{i\sigma},c_{k\uparrow}\right] &= c^\dagger_{i\sigma}\left\{c_{i\sigma},c_{k\uparrow}\right\}-\left\{c^\dagger_{i\sigma},c_{k\uparrow}\right\}c_{i\sigma}\\ &= -c_{i\sigma}\delta_{ik}\delta_{\sigma\uparrow}\ ,\end{aligned}$$

yields,

$$\left[H_0,c_{k\uparrow}\right]=-\sum_{\langle j\rangle}\tilde{t}_{kj}c_{j\uparrow}-\left(\epsilon_k-\tilde{\mu}\right)c_{k\uparrow}\ . \tag{A.10}$$

For the s-wave term we have,

$$\left[H_s,c_{k\uparrow}\right]=\sum_i\left(\Delta_{ii}\left[c^\dagger_{i\uparrow}c^\dagger_{i\downarrow},c_{k\uparrow}\right]+\Delta^\star\left[c_{i\downarrow}c_{i\uparrow},c_{k\uparrow}\right]\right)\ .$$

Evaluating the commutators,

$$\begin{aligned}\left[c^\dagger_{i\uparrow}c^\dagger_{i\downarrow},c_{k\uparrow}\right] &= c^\dagger_{i\uparrow}\left\{c^\dagger_{i\downarrow},c_{k\uparrow}\right\}-\left\{c^\dagger_{i\uparrow},c_{k\uparrow}\right\}c^\dagger_{i\downarrow}\\ &= -c^\dagger_{i\downarrow}\delta_{ik}\ ,\end{aligned}$$

$$\left[c_{i\downarrow}c_{i\uparrow},c_{k\uparrow}\right] = 0\ ,$$

yields,

$$\left[H_s,c_{k\uparrow}\right]=-\Delta_{kk}c^\dagger_{k\downarrow}\ . \tag{A.11}$$

The d-wave term is,

$$\left[H_d,c_{k\uparrow}\right]=\frac{1}{2}\sum_{<i,j>\sigma}V^{(H)}_{ij}\left[n_{i\sigma},c_{k\uparrow}\right]+\frac{1}{2}\sum_{<i,j>}\left(\Delta_{ij}\left[c^\dagger_{i\uparrow}c^\dagger_{j\downarrow},c_{k\uparrow}\right]+\Delta^\star_{ij}\left[c_{j\downarrow}c_{i\uparrow},c_{k\uparrow}\right]\right)\ .$$

After evaluating the commutators

$$\begin{aligned}\left[c^\dagger_{i\uparrow}c^\dagger_{j\downarrow},c_{k\uparrow}\right] &= c^\dagger_{i\uparrow}\left\{c^\dagger_{j\downarrow},c_{k\uparrow}\right\}-\left\{c^\dagger_{i\uparrow},c_{k\uparrow}\right\}c^\dagger_{j\downarrow}\ ,\\ &= -c^\dagger_{j\downarrow}\delta_{ik}\end{aligned}$$

$$\left[c_{j\downarrow}c_{i\uparrow},c_{k\uparrow}\right] = 0\ ,$$

we find

$$\left[H_d,c_{k\uparrow}\right]=-\frac{1}{2}\sum_{<j>}V^{(H)}_{kj}c_{k\uparrow}-\frac{1}{2}\sum_{<j>}\Delta_{kj}c^\dagger_{j\downarrow}\ . \tag{A.12}$$

Upon substituting (A.10), (A.11), (A.12) into (A.9) we find

$$\Big[H_{eff}, c_{k\uparrow}\Big] = -\sum_{\langle j\rangle} \tilde{t}_{kj} c_{j\uparrow} - (\epsilon_k - \tilde{\mu})\, c_{k\uparrow} - \Delta_{kk} c^{\dagger}_{k\downarrow} - \frac{1}{2}\sum_{<j>} V^{(H)}_{kj} c_{k\uparrow} - \frac{1}{2}\sum_{<j>} \Delta_{kj} c^{\dagger}_{j\downarrow}\ . \quad \text{(A.13)}$$

Repeating the same procedure for $[H_{eff}, c_{k\downarrow}]$ results in

$$\Big[H_{eff}, c_{k\downarrow}\Big] = -\sum_{\langle j\rangle} \tilde{t}_{kj} c_{j\downarrow} - (\epsilon_k - \tilde{\mu})\, c_{k\uparrow} + \Delta_{kk} c^{\dagger}_{k\uparrow} - \frac{1}{2}\sum_{<j>} V^{(H)}_{kj} c_{k\downarrow} + \frac{1}{2}\sum_{<j>} \Delta_{kj} c^{\dagger}_{j\uparrow}\ . \quad \text{(A.14)}$$

By substituting the relations (A.7) and (A.8) into (A.13) and (A.14), the commutators can be expressed in terms of the quasiparticle creation and annihilation operators as

$$\begin{aligned}
\Big[H_{eff}, c_{k\uparrow}\Big] = & -\sum_{\langle j\rangle n} \tilde{t}_{kj} \Big(\gamma_{n\uparrow} u_n(j) - \gamma^{\dagger}_{n\downarrow} v^{\star}_n(j)\Big) \quad + \\
& - \quad \sum_n \left(\epsilon_k - \tilde{\mu} + \frac{1}{2}\sum_{<j>} V^{(H)}_{kj}\right) \Big(\gamma_{n\uparrow} u_n(k) - \gamma^{\dagger}_{n\downarrow} v^{\star}_n(k)\Big) \\
& - \quad \sum_n \Delta_{kk} \Big(\gamma^{\dagger}_{n\downarrow} u^{\star}_n(k) + \gamma_{n\uparrow} v_n(k)\Big) \\
& - \quad \frac{1}{2}\sum_{<j>\ n} \Delta_{kj} \Big(\gamma^{\dagger}_{n\downarrow} u^{\star}_n(j) + \gamma_{n\uparrow} v_n(j)\Big)\ .
\end{aligned} \quad \text{(A.15)}$$

Using the Bogoliubov-Valatin transformation for the electron annihilation operator in (A.7),

$$\begin{aligned}
\Big[H_{eff}, c_{k\uparrow}\Big] &= \sum_n u_n(k)\Big[H_{eff}, \gamma_{n\uparrow}\Big] - v^{\star}_n(k)\Big[H_{eff}, \gamma^{\dagger}_{n\downarrow}\Big] \\
&= -\sum_n \Big(\epsilon_n u_n(k)\gamma_{n\uparrow} + \epsilon_n v^{\star}_n(k)\gamma^{\dagger}_{n\downarrow}\Big)\ .
\end{aligned} \quad \text{(A.16)}$$

Comparison of the coefficients of $\gamma_{n\uparrow}$ and $\gamma^{\dagger}_{n\downarrow}$ in (A.15) and (A.16) leads to

$$\sum_{\langle j\rangle} \tilde{t}_{kj} u_n(j) + \left(\epsilon_k - \tilde{\mu} + \frac{1}{2}\sum_{<j>} V^{(H)}_{kj}\right) u_n(k) + \Delta_{kk} v_n(k) + \frac{1}{2}\sum_{<j>} \Delta_{kj} v_n(j) = \epsilon_n u_n(k)\ , \quad \text{(A.17)}$$

$$-\sum_{\langle j\rangle} \tilde{t}_{kj} v_n(j) + \left(\epsilon_k - \tilde{\mu} + \frac{1}{2}\sum_{<j>} V^{(H)}_{kj}\right) v_n(k) + \Delta^{\star}_{kk} u_n(k) + \frac{1}{2}\sum_{<j>} \Delta^{\star}_{kj} u_n(j) = \epsilon_n v_n(k)\ , \quad \text{(A.18)}$$

which are known as the BdG equations. It can be written in matrix form as

$$\begin{pmatrix} \hat{T} + \hat{V}^{(H)} + \hat{V}^{(F)} & \hat{\Delta} \\ \hat{\Delta}^{*} & -\Big(\hat{T}^{*} + \hat{V}^{(H)} + \hat{V}^{(F)}\Big) \end{pmatrix} \begin{pmatrix} u_n \\ v_n \end{pmatrix} = \epsilon_n \begin{pmatrix} u_n \\ v_n \end{pmatrix}. \quad \text{(A.19)}$$

A.2 Derivation for the Ground-State Energy

The ground-state energy is given by

$$\left\langle H_{eff} \right\rangle = \left\langle H_0 \right\rangle + \left\langle H_s \right\rangle + \left\langle H_d \right\rangle \tag{A.20}$$

and we will calculate the expectation values term by term. The expectation value for the single-particle term is

$$\left\langle H_0 \right\rangle = \sum_{\langle ij \rangle \sigma} \tilde{t}_{ij} \left\langle c^\dagger_{i\sigma} c_{j\sigma} \right\rangle + \sum_{i\sigma} \left(\epsilon_i - \tilde{\mu} \right) \left\langle \hat{n}_{i\sigma} \right\rangle .$$

For our calculation u_n and v_n can be assumed to real without loss of generality. One can then show that

$$\left\langle c^\dagger_{i\sigma} c_{j\sigma} \right\rangle = \left\langle c^\dagger_{j\sigma} c_{i\sigma} \right\rangle .$$

Using the definition of the mean fields in (3.6) to (3.10) we find

$$\left\langle H_0 \right\rangle = 2 \sum_{\langle ij \rangle} \tilde{t}_{ij} \frac{V^{(F)}_{ij}}{U_{ij}} + \sum_i \left(\epsilon_i - \tilde{\mu} \right) \left\langle \hat{n}_i \right\rangle . \tag{A.21}$$

For the s and d-wave components we find

$$\begin{aligned} \left\langle H_s \right\rangle &= \sum_i \left(\Delta_{ii} \left\langle c^\dagger_{i\uparrow} c^\dagger_{i\downarrow} \right\rangle + \Delta^\star \langle c_{i\downarrow} c_{i\uparrow} \rangle \right) \\ &= 2 \sum_i \frac{|\Delta^2_{ii}|}{U_{ii}} , \end{aligned} \tag{A.22}$$

$$\begin{aligned} \left\langle H_d \right\rangle &= \frac{1}{2} \sum_{<ij>\sigma} V^{(H)}_{ij} \left\langle \hat{n}_{i\sigma} \right\rangle + \frac{1}{2} \sum_{<i,j>} \left(\Delta_{ij} \left\langle c^\dagger_{i\uparrow} c^\dagger_{j\downarrow} \right\rangle + \Delta^\star_{ij} \left\langle c_{j\downarrow} c_{i\uparrow} \right\rangle \right) \\ &= \frac{1}{2} \sum_{<ij>} V^{(H)}_{ij} \left\langle \hat{n}_i \right\rangle + \sum_{<ij>} \frac{|\Delta_{ij}|^2}{U_{ij}} , \end{aligned} \tag{A.23}$$

where we have again taken advantage of u_n and v_n being real. The expressions (A.21), (A.22), and (A.23) along with the definitions for $\tilde{t_{ij}}$ and $\tilde{\mu}$ yield the total ground-state energy as

$$\begin{aligned} \left\langle H_{eff} \right\rangle =& 2 \sum_{\langle ij \rangle} \left(t_{ij} - \frac{1}{2} V^{(F)}_{ij} \right) \frac{V^{(F)}_{ij}}{U_{ij}} + \sum_i \left(\epsilon_i - \mu + V^{(H)}_{ii} \right) \left\langle \hat{n}_i \right\rangle \\ &+ 2 \sum_i \frac{|\Delta^2_{ii}|}{U_{ii}} + \frac{1}{2} \sum_{<ij>} V^{(H)}_{ij} \left\langle \hat{n}_i \right\rangle + \sum_{<ij>} \frac{|\Delta_{ij}|^2}{U_{ij}} . \end{aligned} \tag{A.24}$$

Appendix B

Numerical Methods

B.1 Introduction to ScaLAPACK

ScaLAPACK, which stands for Scalable Linear Algebra Package, is an extension of the LAPACK library for performance on distributed-memory message passing computers which support PVM and/or MPI. Similarly to LAPACK, ScaLAPACK contains routines for solving linear equations, least squares, and eigenvalue problems. LAPACK however is written as a single thread of execution and does not provide routines for parallel execution. ScaLAPACK is designed for efficiency and scalability as the problem size and number of processors increases.

ScaLAPACK is dependent on a few libraries for implementation. These libraries include the BLAS (Basic Linear Algebra Package) used for performing common linear algebra computations, PBLAS which is a parallel set of the BLAS routines, and BLACS (Basic Linear Algebra Communication Subprograms) which is used for communication of data between process nodes. BLACS and the process grid model will be discussed in the following section. The basic components of ScaLAPACK are shown in Figure B.1. Elements below the dashed line labelled *Local* are called by a single processor, while elements labeled *Global* are parallel routines.

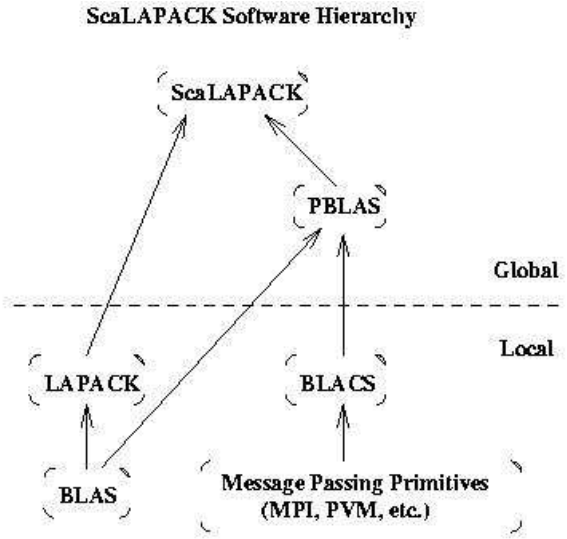

Figure B.1: ScaLAPACK software hierarchy

B.2 BLACS Process Grid

BLACS is a message passing library designed for implementing linear algebra. The processes of a distributed memory machine are organized into a two-dimensional process grid. Each process on the grid stores a piece of the overall matrix. If a calculation is executed with P processes labelled $0, 1, \ldots, P-1$, then the BLACS arranges these processes into a grid with P_r rows and P_c columns where $P_r \times P_c = P$. This ordering also allows for certain forms of scoped operations. For example, we can issue commands that only allow a specific process row or column to participate. This mapping is done so that matrix elements can be efficiently distributed across different process nodes. An example of eight processes mapped onto a 2×4 process grid is shown in Figure B.2

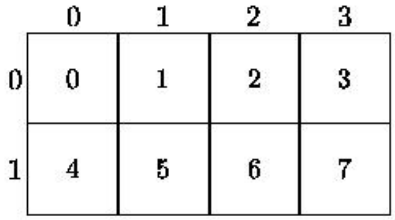

Figure B.2: Example of a $P_r = 2$, $P_c = 4$ process grid

B.3 Distributed Memory Storage Scheme

Once the process grid had been initialized by the BLACS the matrix elements must be distributed out to the processes in the grid. For the execution of a parallel program to be efficient, the distribution of matrix elements should be well balanced amongst the processes on the grid. Load balancing and communication characteristics largely influence the performance of the computation and must be considered during the design of high performance algorithms. For dense matrices ScaLAPACK distributes the memory according to the *two-dimensional block-cyclic* data scheme. This distribution scheme provides a simple way to partition a matrix and distribute the elements across a process grid.

In a two-dimensional block cyclic data distribution the first task is to divide the matrix into blocks of size $M_B \times N_B$. If the block size does not divide the matrix evenly, then the last block in each row/column will contain the remaining elements. These blocks are then cyclically dealt out to each process in the grid like a deck of cards. As an example, we will distribute the following 9×9 matrix across a 2×2 process grid using a block size of $M_B = N_B = 2$ as shown in Figure B.3.

Process Column

Process Row

	0		1		0		1		0
0	a_{11}	a_{12}	a_{13}	a_{14}	a_{15}	a_{16}	a_{17}	a_{18}	a_{19}
	a_{21}	a_{22}	a_{23}	a_{24}	a_{25}	a_{26}	a_{27}	a_{28}	a_{29}
1	a_{31}	a_{32}	a_{33}	a_{34}	a_{35}	a_{36}	a_{37}	a_{38}	a_{39}
	a_{41}	a_{42}	a_{43}	a_{44}	a_{45}	a_{46}	a_{47}	a_{48}	a_{49}
0	a_{51}	a_{52}	a_{53}	a_{54}	a_{55}	a_{56}	a_{57}	a_{58}	a_{59}
	a_{61}	a_{62}	a_{63}	a_{64}	a_{65}	a_{66}	a_{67}	a_{68}	a_{69}
1	a_{71}	a_{72}	a_{73}	a_{74}	a_{75}	a_{76}	a_{77}	a_{78}	a_{79}
	a_{81}	a_{82}	a_{83}	a_{84}	a_{85}	a_{86}	a_{87}	a_{88}	a_{89}
0	a_{91}	a_{92}	a_{93}	a_{94}	a_{95}	a_{96}	a_{97}	a_{98}	a_{99}

Figure B.3: A 9X9 matrix distributed across 4 processors

The important thing to remember in this style of data distribution is that every process in the grid owns a collection of these blocks, which are then stored locally in a two-dimensional column major array. For example the local matrix stored by process $(0, 0)$ is a 5×5 array with elements:

$$A_{0,0} = \begin{pmatrix} a_{11} & a_{12} & a_{15} & a_{16} & a_{19} \\ a_{21} & a_{22} & a_{25} & a_{26} & a_{29} \\ a_{51} & a_{52} & a_{55} & a_{56} & a_{59} \\ a_{61} & a_{62} & a_{65} & a_{66} & a_{69} \\ a_{91} & a_{92} & a_{95} & a_{96} & a_{99} \end{pmatrix}$$

Similarly process $(0, 1)$ owns a 5×4 array, $(1, 0)$ owns a 4×5 array, and $(1, 1)$ owns a

4×4 array. In this case the load is not shared evenly by the processors; however, it is the most balanced distribution given this particular matrix size. If we had chosen a block size of $M_B = N_B = 3$ we would have an even division of the global matrix. However process $(0,0)$ and $(1,0)$ would take on approximately twice as many matrix elements as the remaining nodes.

From this example we can see that the size of the matrix we are solving is only limited by the number of processors available. This is the advantage of the distributed memory scheme, as it allows one to solve problems that are much larger than any one processor is capable of performing alone.

B.4 Diagonalization of BdG Matrix Elements

The BdG Equations are given by:

$$\sum_{i'} \left(\hat{T}_{ii'} + \hat{V}^{(F)}_{ii'} \right) u_n(i') + \hat{V}^{(H)}_{ii} u_n(i) + \hat{\Delta}_{ii} v_n(i) + \sum_{i'} \hat{\Delta}_{ii'} v_n(i') = \epsilon_n u_n(i) \ , \tag{B.1}$$

$$-\sum_{i'} \left(\hat{T}_{ii'} + \hat{V}^{(F)}_{ii'} \right) v_n(i') + \hat{V}^{(H)}_{ii} v_n(i) + \hat{\Delta}^{\star}_{ii} u_n(i) + \sum_{i'} \hat{\Delta}^{\star}_{ii'} u_n(i') = \epsilon_n v_n(i) \ , \tag{B.2}$$

where

$$\hat{T}_{ii'} = \sum_{<j>} t_{ij} \delta_{i'j} - (\mu - \epsilon_i)\, \delta_{ii'} \ , \tag{B.3}$$

$$\hat{V}^{(H)}_{ii} = V^{(H)}_{ii} + \frac{1}{2} \sum_{<j>} V^{(H)}_{ij} \ , \tag{B.4}$$

$$\hat{V}^{(F)}_{ii'} = -\frac{1}{2} \sum_{<j>} V^{(F)}_{ij} \delta_{i'j} \ , \tag{B.5}$$

$$\tag{B.6}$$

and

$$t_{ij} = \begin{cases} -t & \text{if } i \text{ and } j \text{ are nearest neighbours,} \\ t' & \text{if } i \text{ and } j \text{ are next nearest neighbours,} \\ 0 & \text{otherwise.} \end{cases} \tag{B.7}$$

The $< j >$ indicates a sum over sites j which are neighbours to site i. The selfconsistent mean fields $V^{(H)}_{ij}$, $V^{(F)}_{ij}$, and Δ_{ij} are given by

$$V^{(H)}_{ij} = U_{ij} \sum_n \left[\, |u_n(j)|^2 f_n + |v_n(j)|^2 (1 - f_n) \, \right] , \tag{B.8}$$

$$\Delta_{ij} = -\frac{1}{2} U_{ij} \sum_n \left[\, u_n(i) v^*_n(j) + u_n(j) v^*_n(i) \, \right] (1 - 2 f_n) \, , \tag{B.9}$$

$$\begin{aligned} V^{(F)}_{ij} = \frac{1}{2} U_{ij} \sum_n \big[& \left(u^*_n(i) u_n(j) + u_n(i) u^*_n(j) \right) f_n \\ & + \left(v_n(i) v^*_n(j) + v^*_n(i) v_n(j) \right) (1 - f_n) \, \big] \end{aligned} \tag{B.10}$$

which are valid for either $j = i$ or $j \neq i$. The sums in Equations (B.8) to (B.10) are over positive eigenvalues only. We use n to label the eigenvalues and i to label the sites. If the system contains N sites then i ranges from $1 \leq i \leq N$. The f_n is the Fermi-Dirac distribution function with argument $\beta\epsilon_n$, where $\beta = 1/k_B T$, with T the temperature.. This gives us two coupled equations which are to be solved simultaneously. The presence of the mean fields (B.8) to (B.10) indicate that they must also be solved selfconsistently.

These equations can be written in the more compact form

$$\begin{pmatrix} \hat{T} + \hat{V}^{(H)} + \hat{V}^{(F)} & \hat{\Delta} \\ \hat{\Delta}^* & -\left(\hat{T}^* + \hat{V}^{(H)} + \hat{V}^{(F)}\right) \end{pmatrix} \begin{pmatrix} u_n \\ v_n \end{pmatrix} = \epsilon_n \begin{pmatrix} u_n \\ v_n \end{pmatrix} . \tag{B.11}$$

By introducing the composite eigenvector

$$\begin{pmatrix} u_n \\ v_n \end{pmatrix} = \begin{pmatrix} u_n^1 \\ u_n^2 \\ \vdots \\ u_n^N \\ v_n^1 \\ v_n^2 \\ \vdots \\ v_n^N \end{pmatrix} \tag{B.12}$$

we can rewrite Equation (B.11) in terms of only one matrix Λ given by:

$$\Lambda_{jj'} = \begin{cases} \hat{T}_{jj'} + \hat{V}_{jj}^{(H)} + \hat{V}_{jj'}^{(F)} + \delta_{j+N,j'}\hat{\Delta}_{jj'} & j \leq N \\ -\hat{T}_{j-M,j'-M} - \hat{V}_{j-M,j-M}^{(H)} - \hat{V}_{j-M,j'}^{(F)} + \delta_{j-M,j'}\hat{\Delta}_{j-M,j'}^{\star} & j > N \, . \end{cases} \tag{B.13}$$

The column index j' of the matrices $\hat{T}$, $\hat{V}^{(H)}$, and $\hat{V}^{(F)}$ on the first (second) line is also restricted to $j' \leq N$ ($j' > N$). The matrices are $N \times N$ while the overall matrix Λ is $2N \times 2N$. The indices j and j' therefore run from 1 to $2N$. In terms of the site label i we have

$$i = \begin{cases} j & j \leq N \\ j - N & j > N \end{cases}$$

This will give the matrix components of Λ as

$$\hat{\Lambda} = \begin{pmatrix}
-\tilde{\mu} & \tilde{t} & 0 & \cdots & 0 & \tilde{t} & \Delta_1 & \Delta_{12} & 0 & \cdots & 0 & 0 \\
\tilde{t} & -\tilde{\mu} & \tilde{t} & 0 & \cdots & 0 & \Delta_{21} & \ddots & 0 & \cdots & 0 & 0 \\
0 & \tilde{t} & \ddots & \ddots & 0 & \cdots & 0 & \ddots & \ddots & \ddots & \vdots & \vdots \\
\vdots & 0 & \ddots & \ddots & \ddots & 0 & \cdots & 0 & \ddots & \ddots & 0 & 0 \\
0 & 0 & 0 & \tilde{t} & -\tilde{\mu} & \tilde{t} & 0 & 0 & \cdots & \Delta_{N-1,N-2} & \Delta_{N-1} & \Delta_{N-1,N} \\
\tilde{t} & 0 & 0 & 0 & \tilde{t} & -\tilde{\mu} & 0 & \cdots & 0 & 0 & \Delta_{N,N-1} & \Delta_N \\
\Delta_1^\star & \Delta_{12}^\star & 0 & \cdots & 0 & 0 & \tilde{\mu} & -\tilde{t} & 0 & \cdots & 0 & -\tilde{t} \\
\Delta_{21}^\star & \ddots & 0 & \cdots & 0 & 0 & -\tilde{t} & \tilde{\mu} & -\tilde{t} & 0 & \cdots & 0 \\
\vdots & \ddots & \ddots & \ddots & \cdots & 0 & 0 & \ddots & \ddots & \ddots & 0 & \vdots \\
0 & 0 & 0 & \ddots & \Delta_{N-1}^\star & \Delta_{N-1,N}^\star & 0 & \cdots & 0 & -\tilde{t} & \tilde{\mu} & -\tilde{t} \\
0 & 0 & 0 & \cdots & \Delta_{N,N-1}^\star & \Delta_N^\star & -\tilde{t} & 0 & \cdots & 0 & -\tilde{t} & \tilde{\mu}
\end{pmatrix} \tag{B.14}$$

Together with the composite eigenvector the BdG equations can be written as an eigenvalue equation,

$$\hat{\Lambda}\mathbf{x} = \lambda\mathbf{x} \; . \tag{B.15}$$

There are $2N$ eigenvalues λ and eigenvectors which correspond to the particle ($n \leq N$) and hole ($n > N$) energies and wavefunctions, respectively. The matrix $\hat{\Lambda}$ is distributed across the process nodes according to the storage scheme discussed in the previous section. The diagonalization is done using the ScaLAPACK routine PDSYEVD. This routine solves the eigenvalues and eigenvectors for a given symmetric distributed matrix using a divide and conquer algorithm. The eigenvectors are stored in an $2N \times 2N$ distributed matrix $\hat{Z}$ with the eigenvectors as columns.

$$\hat{Z} = \begin{pmatrix} \mathbf{x_1} & \mathbf{x_2} & \cdots & \mathbf{x_{N-1}} & \mathbf{x_N} \end{pmatrix} \tag{B.16}$$

B.5 Calculations with Distributed Matrices

Once the matrix $\hat{\Lambda}$ has been diagonalized we can compute the quantities given in Equations (B.8) to (B.10). This process is not quite straightforward since the elements of the eigenvectors are distributed across each processor. We need to construct a mechanism for computing these quantities which minimizes the number of communication broadcasts. The trick is defining a one dimensional array that will store the *local* eigenvector components for a given column of the matrix Z. For example, suppose we have only $N = 6$ sites. This gives the dimensions of $\hat{\Lambda}$ and x as 12×12 and 12×1, respectively. To solve this with ScaLAPACK we can use a 2×2 process grid using $M_B = N_B = 3$. The local components for the n-th column of $\hat{Z}$ for each process will be

$$\begin{pmatrix} u_1^n \\ u_2^n \\ u_3^n \\ 0 \\ 0 \\ 0 \\ v_1^n \\ v_2^n \\ v_3^n \\ 0 \\ 0 \\ 0 \end{pmatrix} \quad \begin{pmatrix} 0 \\ 0 \\ 0 \\ 0 \\ 0 \\ 0 \\ 0 \\ 0 \\ 0 \\ 0 \\ 0 \\ 0 \end{pmatrix} \quad \begin{pmatrix} 0 \\ 0 \\ 0 \\ u_4^n \\ u_5^n \\ u_6^n \\ 0 \\ 0 \\ 0 \\ v_4^n \\ v_5^n \\ v_6^n \end{pmatrix} \quad \begin{pmatrix} 0 \\ 0 \\ 0 \\ 0 \\ 0 \\ 0 \\ 0 \\ 0 \\ 0 \\ 0 \\ 0 \\ 0 \end{pmatrix}$$

$$Node: \qquad (0,0) \qquad (0,1) \qquad (1,0) \qquad (1,1)$$

At this point it is possible to call the BLACS routine DGSUM2D which performs an element-wise summation of an array or a matrix. The result(which will be the desired column of the matrix $\hat{Z}$) is placed on all nodes after completion of the summation. If we were to perform a gathering operation for each element of $\hat{Z}$, we would require $N^2/2$ broadcasts (since we only need to perform summations for positive eigenvalues). Using this method of summing local process columns, we only need to perform $N/2$ broadcast calls, considerably increasing the performance of the routine.

Once Δ_{ij}, $V_{ij}^{(H)}$, and $V_{ij}^{(F)}$ have been computed we can substitute them into (B.11) and perform the routine again for the new matrix elements. This process must be performed until all mean fields are selfconsistent to within a desired convergence criterion. For example we would iterate the BdG equations until the order parameter satisfies

$$\left| \frac{\Delta_i^{\text{New}} - \Delta_i^{\text{Old}}}{\Delta_i^{\text{New}}} \right| < \epsilon \tag{B.17}$$

where ϵ is the desired tolerance for Δ.

Appendix C

Derivation of the Dispersion Relations

In the normal state the tight-binding Hamiltonian including next-nearest neighbour hopping is given by

$$H_0 = \sum_{\langle ij\rangle\sigma} t_{ij} c^{\dagger}_{i\sigma} c_{j\sigma} - \sum_{i\sigma} \mu\, \hat{n}_{i\sigma}\,, \tag{C.1}$$

where

$$t_{ij} = \begin{cases} -t; & \text{if } i \text{ and } j \text{ are nearest neighbours.} \\ t'; & \text{if } i \text{ and } j \text{ are next nearest neighbours.} \\ 0; & \text{otherwise.} \end{cases} \tag{C.2}$$

Wwe introduce the Fourier transform of the creation and annihilation operators as

$$c_{i\sigma} = \frac{1}{\sqrt{N}} \sum_{\vec{k}} c_{k\sigma} e^{i\vec{k}\cdot\vec{R}_i}\,, \tag{C.3}$$

$$c_{k\sigma} = \frac{1}{\sqrt{N}} \sum_{\vec{R}_i} c_{i\sigma} e^{-i\vec{k}\cdot\vec{R}_i}\,, \tag{C.4}$$

where N is the total number of sites on the lattice. For simplicity hereafter we will suppress the spin index. Denoting the lattice spacing as a and by using periodic boundary conditions on the lattice the Bloch condition for the wavefunctions $\psi(x)$ in one dimension gives:

$$\begin{aligned} \psi(x + N_x a) &= \psi(x); \\ \psi_{k_x}(x + N_x a) &= e^{ik_x N_x a} \psi_{k_x}(x)\,, \end{aligned}$$

so that we must have

$$e^{ik_x N_x a} = 1\,, \tag{C.5}$$

i.e.,

$$k_x = \frac{2\pi n_x}{N_x a} \tag{C.6}$$

where $-\frac{N_x}{2} \leq n_x \leq \frac{N_x}{2}$. Similar results hold for both y and z directions. We can break up the Hamiltonian into two separate sums and calculate the contributions from nearest neighbours and next-nearest neighbours separately. That is to say that we replace the sum over $\langle ij\rangle$ with

$$\sum_{\langle ij\rangle} = \sum_{\langle ij\rangle}^{\text{N.N}} + \sum_{\langle i\ell\rangle}^{\text{Next N.N}}\,, \tag{C.7}$$

where j are the nearest neighbours (N.N) and ℓ are the next-nearest neighbours (Next N.N) to site i. Calculating the first term in the Hamiltonian explicitly gives

$$-t\sum_{\langle ij\rangle} c_i^\dagger c_j = \frac{-t}{N}\sum_{\langle ij\rangle\sigma}\sum_{kk'} c_k^\dagger c_{k'} e^{i\left(\vec{k}\cdot\vec{R}_i - \vec{k'}\cdot\vec{R}_j\right)} \ . \tag{C.8}$$

In two dimensions ($N = N_x N_y$) the nearest neighbour sites are

$$\vec{R}_j = \{(x_i \pm a, y_i), (x_i, y_i \pm a)\} \ . \tag{C.9}$$

Then writing out the sum over nearest neighbours we have

$$\begin{aligned}
-t\sum_{\langle ij\rangle} c_i^\dagger c_j &= \frac{-t}{N}\sum_{\vec{R}_i}\sum_{kk'} c_k^\dagger c_{k'}\left(e^{i\left(\vec{k}\cdot\vec{R}_i - \vec{k'}\cdot\left(\vec{R}_i \pm a\hat{x}\right)\right)} + e^{i\left(\vec{k}\cdot\vec{R}_i - \vec{k'}\cdot\left(\vec{R}_i \pm a\hat{y}\right)\right)}\right) \\
&= \frac{-t}{N}\sum_{\vec{R}_i}\sum_{kk'} c_k^\dagger c_{k'} e^{i\left(\vec{k}-\vec{k'}\right)\cdot\vec{R}_i}\left(e^{\mp\vec{k'}\cdot a\hat{x}} + e^{\mp\vec{k'}\cdot a\hat{y}}\right) \\
&= \frac{-2t}{N}\sum_{\vec{R}_i}\sum_{kk'}\left(\cos(k'_x a) + \cos(k'_y a)\right) c_k^\dagger c_{k'} e^{i\left(\vec{k}-\vec{k'}\right)\cdot\vec{R}_i}
\end{aligned}$$

We can write $\vec{R}_i = a(i_x, i_y)$, where i_x and i_y are the site numbers, and the summation over the coordinates as

$$\sum_{\vec{R}_i} = \sum_{i_x, i_y} \ , \tag{C.10}$$

where $i_x = 1, 2, \cdots, N_x$ and $i_y = 1, 2, \cdots, N_y$. If we let $\vec{q} = \vec{k} - \vec{k'}$ where

$$\vec{q}_x = \frac{2\pi m_x}{N_x a} \qquad \vec{q}_y = \frac{2\pi m_y}{N_y a}$$

and $m_x = n_x - n'_x$, $m_y = n_y - n'_y$ are also integers then we can evaluate the sum over coordinates as

$$\begin{aligned}
\sum_{i_x=1}^{N_x}\sum_{i_y=1}^{N_y} e^{i\left(\vec{k}-\vec{k'}\right)\cdot\vec{R}_i} &= \left(\sum_{i_x=1}^{N_x} e^{iq_x i_x a}\right)\left(\sum_{i_y=1}^{N_y} e^{iq_y i_y a}\right) \\
&= \left(\frac{1 - e^{i2\pi m_x}}{e^{-i2\pi m_x/N_x} - 1}\right)\left(\frac{1 - e^{i2\pi m_y}}{e^{-i2\pi m_y/N_y} - 1}\right) \\
&= 0 \ .
\end{aligned}$$

However, if $\vec{k} = \vec{k'}$ then

$$\sum_{i_x=1}^{N_x}\sum_{i_y=1}^{N_y} e^{i\left(\vec{k}-\vec{k'}\right)\cdot\vec{R}_i} = N_x N_y = N \ ,$$

therefore

$$\sum_{\vec{x_i}} e^{i\left(\vec{k}-\vec{k'}\right)\cdot\vec{R}_i} = \delta_{kk'} N \ . \tag{C.11}$$

Then

$$\begin{aligned} -t\sum_{\langle ij\rangle} c_i^\dagger c_j &= \frac{-2t}{N}\sum_{kk'}\left(\cos(k'_x a)+\cos(k'_y a)\right) c_k^\dagger c_{k'}\delta_{kk'}N \\ &= -2t\sum_k \left(\cos(k_x a)+\cos(k_y a)\right) c_k^\dagger c_k \ . \end{aligned} \tag{C.12}$$

Now calculating the contribution from the next-nearest neighbours yields

$$t'\sum_{\langle i\ell\rangle} c_i^\dagger c_k = \frac{t'}{N}\sum_{\langle i\ell\rangle}\sum_{kk'} c_k^\dagger c_{k'} e^{i\left(\vec{k}\cdot\vec{R}_i-\vec{k'}\cdot\vec{R}_\ell\right)} \ . \tag{C.13}$$

The next-nearest neighbours are given by the coordinates

$$\vec{R}_\ell = \vec{R}_i \pm a(\hat{x}\pm\hat{y}) \ . \tag{C.14}$$

Writing out the sum over next-nearest neighbours gives:

$$\begin{aligned} t'\sum_{\langle i\ell\rangle} c_i^\dagger c_k &= \frac{t'}{N}\sum_{\vec{R}_i}\sum_{kk'} c_k^\dagger c_{k'} e^{i\left(\vec{k}\cdot\vec{R}_i-\vec{k'}\cdot\vec{R}_i\pm a(\hat{x}\pm\hat{y})\right)} \\ &= t'\sum_{kk'} c_k^\dagger c_{k'}\delta_{kk'} e^{\mp ia(k'_x\pm k'_y)} \end{aligned}$$

where

$$\begin{aligned} e^{\mp ia(k'_x\mp k'_y)} &= e^{-ak'_x}e^{-ak'_y}+e^{-ak'_x}e^{ak'_y}+e^{ak'_x}e^{-ak'_y}+e^{ak'_x}e^{ak'_y} \\ &= 2e^{k'_x a}\cos(k'_y a)+2e^{-k'_x a}\cos(k'_y a) \\ &= 4\cos(k'_x a)\cos(k'_y a) \ . \end{aligned}$$

Therefore the sum over next-nearest neighbours becomes

$$t'\sum_{\langle i\ell\rangle} c_i^\dagger c_k = 4t'\sum_k \cos(k_x a)\cos(k_y a) c_k^\dagger c_k \ . \tag{C.15}$$

Substituting Eqs (C.15) and (C.12) into the Hamiltonian yields

$$H_0 = \sum_k E(\vec{k}) c_k^\dagger c_k \ , \tag{C.16}$$

where

$$E(\vec{k}) = -2t\left(\cos(k_a a)+\cos(k_y a)\right)+4t'\cos(k_x a)\cos(k_y a)-\mu \ . \tag{C.17}$$

Appendix D

Chemical Potential and DOS for Negative t'

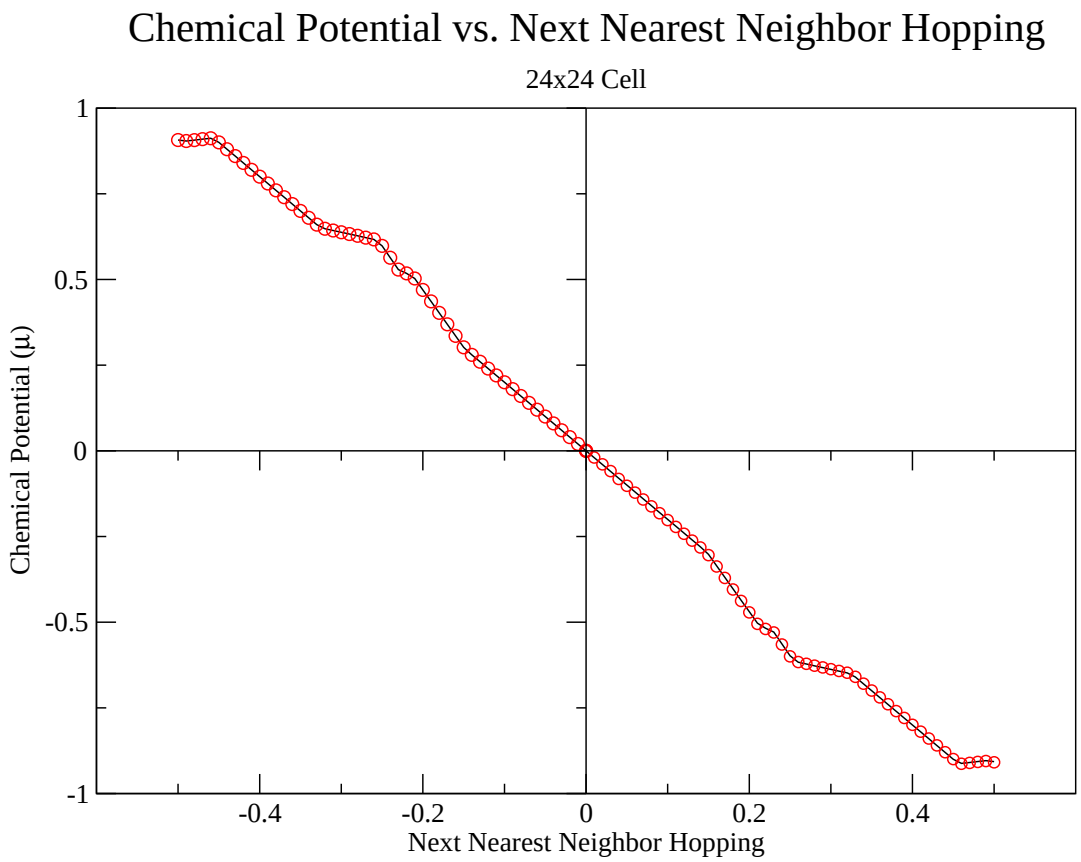

Figure D.1: Chemical potential for $-0.5 \leq t' \leq 0.5$ on a 24x24 lattice. The chemical potential increases for negative t' such that μ for positive and that for negative t' are mirror images of each other.

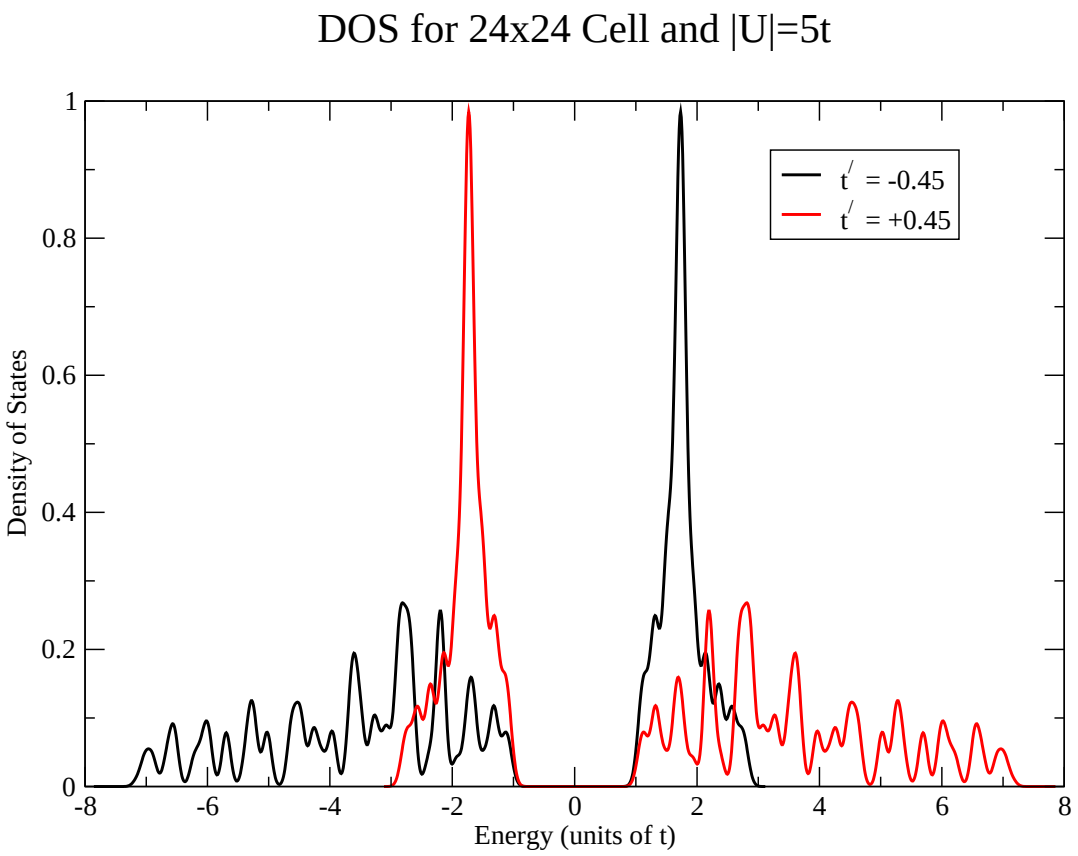

Figure D.2: Density of states for positive and negative t' on a 24x24 cell with $|U| = 5t$. Clearly, the density of states for positive and negative t' are identical with $E(k) \rightarrow -E(k)$.